Universitat Autònoma de Barcelona

Magnetic Metal-Organic / Topological Insulator Heterostructures

Marc González Cuxart

Universitat Autònoma de Barcelona
Institut Català de Nanociència i Nanotecnologia

Ph.D. Thesis in Physics

Magnetic Metal-Organic / Topological Insulator Heterostructures

Marc González Cuxart

Directors:
Prof. Aitor Mugarza
Prof. Sergio O. Valenzuela
Dr. César Moreno

Tutor:
Prof. Jordi Sort

March 2019

Abstract

Topological Insulators (TIs) have become one of the wonder materials of condensed matter physics over the last decade due to their novel properties, possessing an insulating bulk in coexistence with metallic boundaries. They present an inverted band gap consequence of strong spin orbit coupling, which gives rise to the conductive boundary states with linear dispersion, characteristic of Dirac fermions, and helical spin polarization. Numerous materials have been predicted and observed to have TI signatures, holding great perspective for the realization of novel applications in spintronics, quantum computing and metrology.

The experimental realization of three-dimensional TIs with the the Fermi Level located well in the bulk band gap is a challenging task because of their relatively small gap of hundreds of meV, and their high sensibility to crystal defects and impurities. These can induce electron doping that activates bulk conduction channels, thus burying the contribution of the surface states to the transport. Molecular Beam Epitaxy (MBE) has been reported to be the most suitable growth method to overcome this hindrance, due to its capability to grow single crystals with fine control over the crystal defects and impurity level. The first part of this thesis deals with the growth of high-quality TIs that maintain their pristine insulating bulk behaviour. By using MBE, we studied the impact of different substrates and growth parameters to the synthesis of Bismuth Telluride (Bi_2Te_3) thin films, and the growth of the ternary compound Bismuth-Antimony Telluride.

We were able to grow insulating Bi_2Te_3 thin films with complete suppression of the "twin" domains, mirror-symmetric domains that contribute to the self-doping of the crystal. By a combination of the initial interaction with the lattice-matched Barium Fluoride substrate and the high working temperatures, the growth of Bi_2Te_3 single-crystalline films is achieved already from the first layer. More importantly, the films present low-doping level with the the Fermi Level kept in the bulk band gap. The correlation between the lack of "twin" domains (measured by Reflection High-Energy Electron Diffraction, X-ray Diffraction and Atomic Force Microscopy) and the low-doping level measured by Angle-Resolved Photoemission Spectroscopy (ARPES), indicates the relation between the crystal quality and the capability to preserve the bulk insulating character. This result contrasts to other TIs grown on more conventional substrates, typically presenting large lattice misfits that lead to the formation of an initial polycrystalilne or amorphous seed layer. In parallel, we explored a complemen-

tary approach to the growth of insulating Bi_2Te_3, based on the addition of Sb at the expense of Te atoms. A sequence of Bismuth-Antimony Telluride films with different x content were measured by X-ray Photoemission Spectroscopy (XPS) and ARPES, showing that the the Fermi Level can be gradually brought to the bulk valence band. The realization of such TIs, with a controlled level of the the Fermi Level position is of special interest for counteracting the n-doping effects typically induced by the addition of magnetic materials.

The second and more extended part of this thesis is devoted to the study of interfaces formed by magnetic Metal-organic molecules deposited on the TI thin films. Interfacing TI surfaces with magnetic materials can give rise to novel magnetoelectronic phenomena, involving the manipulation of spin-torques (Inverse Edelstein Effect), or the realization of spin polarized edge states (Quantum Anomalous Hall Effect). The realization of such spin-related effects rely on the capability to control the interfacial magnetic and electronic interactions. The use of organic molecules to cage magnetic ions has been proved to be a versatile approach to engineer inter-ions and ions-surface interactions, due to the flexible design that molecules offer and to their ability to form structurally perfect self-assembled structures. Moreover, they can also act as building blocks for covalent or coordination structures via on-surface reactions.

As a first approach to tune the interfacial properties with Metal-organic molecules, we showed how the ligand chemistry allows a progressive control over the magnetic interactions between a hosted Co ion and a prototypical Au surface. The spin states and magnetic moments are comprehensively studied thanks to the complementary use of local spectroscopic Scanning Tunneling Spectroscopy and non-local magnetic sensitive X-ray Magnetic Circular Dichroism (XMCD) techniques, which are supported theoretically by Density Functional Theory (DFT). We were able to continuously cover the range of magnetic Co ion-substrate interactions, from a strong interacting scenario where the magnetic moment is quenched, to a gradual decrease of the interaction revealed by a lower Kondo screening of the spin. In addition, by changing the Au surface for a TI surface, the interfacial interactions reach the weakest limit in which the molecular magnetic structure is completely decoupled from the substrate electrons.

Thereafter, we explored the electronic and magnetic interactions between the Topological Surface State of the Bi_2Te_3 thin film and Co ions caged in two different planar molecules such as Cobalt - Tetrakis (4-Promophenyl) Porphyrin (CoTBrPP) and Cobalt - Phthalocyanine (CoPc). We found a Metal-organic / TI interface with unperturbed electronic and magnetic properties. This is assessed by a coverage dependent ARPES study in which the Topological Surface State persists upon the deposition of one (CoTBrPP or CoPc) molecular layer. On the other hand, XMCD and Scanning Tunneling Spectroscopy measurements reveal the preservation of the pristine CoTBrPP magnetic moment and electronic structure respectively. Furthermore, a comprehensive Scanning Tunneling Microscopy (STM) and DFT study of the CoTBrPP adsorption geometry describes weak molecule-surface interactions, and corroborates the electronic decoupling of the Metal-organic layer from the TI surface. In an analogue study with CoPc we find slightly stronger interactions yet within the non-perturbative regime, that

suggesting ligand chemistry can be used to tune magnetic interactions without affecting the overall properties of each component of the heterostructure.

Subsequently, the Br-functionalized CoTBrPP on Bi_2Te_3 system was used to induce on-surface synthesis of Metal-organic coordination networks on TI. These more entangled structures are of great interest as a framework in which magnetic ions could arrange in ordered and mechanically stable arrays. Two different coordination phases are selectively created after CoTBrPP dehalogenation upon thermal activation. We track the chemical reaction by XPS, and investigate the morphological and electronic properties of the final products by combining Scanning Tunneling Spectroscopy (STS) and DFT calculations. We conclude that the resulting structures consists of CoTPP coordinated with Te atoms incorporated from the substrate, and thanks to the supporting DFT calculations, we are able to explain the presence of linear chains and irregular coordinated networks. In parallel, the presence of unperturbed Topological Surface State upon the formation of the Metal-organic structures is confirmed by a coverage-dependent ARPES study.

Overall, the first part of the thesis constitutes an extensive study of MBE grown of Bi_2Te_3 thin films, in which different substrates and growth conditions are discussed. Furthermore, the results provide a route for the enhancement of the crystal quality of simple diatomic TIs, crucial for the preservation of their bulk insulating behaviour. The results presented in the second part conceive the capabilities of organic molecules to tune magnetic interactions between Co atoms and Bi_2Te_3 films, and pave the way for the on-TI surface synthesis of magnetic supramolecular structures.

Contents

List of abbreviations

E_F Fermi Level.

T_K Kondo Temperature.

ARPES Angle-Resolved Photoemission Spectroscopy.

Bi_2Te_3 Bismuth Telluride.

CoPc Cobalt - Phthalocyanine.

CoTBrPP Cobalt - Tetrakis (4-Promophenyl) Porphyrin.

DFT Density Functional Theory.

DOS Density of States.

MBE Molecular Beam Epitaxy.

MO Metal-Organic.

QL Quintuple-Layer.

STM Scanning Tunneling Microscopy.

STS Scanning Tunneling Spectroscopy.

TI Topological Insulator.

TSS Topological Surface State.

UHV Ultra High Vacuum.

vdW van der Waals.

XAS X-ray Absorption Spectroscopy.

XMCD X-ray Magnetic Circular Dichroism.

XPS X-ray Photoemission Spectroscopy.

A tota la meva família.

Chapter 1

Introduction

Interfaces in nature are n-dimensional boundary regions separating different immiscible phases of matter. They have long fascinated researchers because of their unique properties and functionalities differing from those of the bulk material on either side of the interface [1]. Human skin is an illustrative example, as it does not act as a simple anatomical barrier of our body, but it also functions as heat regulator, vitamin D synthesizer and sweat excretion system among others. Another common interface is that between a body of liquid water and air, which behaves somewhat similar to an elastic membrane due to an emerging physical property, the surface tension.

In solid-state systems, the dimensions of interfaces are typically limited to a few atoms or a few atomic layers, whose properties differ significantly from those of the bulk atoms that it separates [2]. Their study constitutes the field of surface or interface physics, a well-defined sub-discipline of general condensed-matter physics, with implications in numerous areas of application such as surface coatings, heterogeneous catalysis, or semiconductor technology and electronic devices. A paradigmatic example of a solid-state interface triggering novel properties is formed by lanthanum aluminate ($LaAlO_3$) and strontium titanate ($SrTiO_3$). Even though they are non-magnetic insulators, their interface can exhibit electrical conductivity, superconductivity, ferromagnetism, magnetoresistance or photoconductivity [3–7]. As a result, this interface has been envisaged to have potential for multiple applications such as field-effect and thermoelectric devices, sensors and photodetectors [8].

Interfaces have also a crucial role in the emergence of novel phenomena between different topological phases of matter. Topological matter refers to systems whose fundamental properties are described by a topological invariant, implying that some macroscopic measurable magnitudes do not change upon modifications within the same topological order. This class of matter includes materials with topological defects such as skyrmions [9], with symmetry-protected topological phases such as topological crystalline insulators [10] and Dirac/Weyl semimetals [11] or with topologically-protected boundary modes such as Topological Insulators (TIs). Indeed, "the discovery of topological transitions and topological

phases of matter" granted D. Thouless, D. Haldane and M. Kosterlitz the 2016 Nobel Prize in Physics [12].

In the case of TIs [13, 14], insulating bulk materials possessing metallic boundary states, the topology of the electronic structure is altered due to strong spin orbit coupling that inverts the conventional order of the conduction and valence band around the band gap. Conventional order refers to the appropriate order of atomic levels; whereas the energy of the p-levels lies below that of s-level in semiconductors (referred as trivial insulators from now on), in TIs, the s-orbital is pulled below the p-orbitals giving rise to an inverted gap, where the conduction and valence band are populated by p and s electrons respectively. This inverted bulk band structure harbours a non-trivial topological phase and, as a consequence, states continuously connecting the conduction and valence bands emerge at the interface between the non-trivial and a trivial insulator. The robustness of such states is granted as long as the transition between different topological phases is conserved, that is the Topological Surface State (TSS) is topologically protected.

TIs are one of the few examples of materials that were first predicted and later experimentally observed. In 2005, two groups introduced models for a two-dimensional TI [15, 16], adapting an earlier model based on an integer Quantum Hall Effect (QHE) [17], that is the quantized version of the Hall Effect (HE) occurring in a two-dimensional electron gas. They proposed a new type of insulator with a non-trivial order characterized by the so-called Quantum Spin Hall Effect (QSHE). The QSHE in a 2D TI can be understood as a time reversal invariant version of QHE, and it is well-described in terms of wave vector $\mathbf{k}$ by an effective Hamiltonian of the interaction between the conduction and valence bands [18]. For a Quantum Spin Hall insulator where conduction and valence bands are inverted, the eigenvalues lead to a pair of edge states of opposite $\mathbf{k}$ that carry opposite spins. These interfacial states present helical spin texture that preserves Time Reversal Symmetry (TRS), and whose carriers are subject to spin-momentum locking. Therefore, elastic transitions between $\mathbf{k} \rightarrow -\mathbf{k}$ are not allowed as they would simultaneously entail $\mathbf{s} \rightarrow -\mathbf{s}$ spin transitions, i.e. backscattering is forbidden.

One year after the theoretical prediction, M. König et al. [19] observed the occurrence of QSHE in quantum wells of mercury telluride (HgTe) sandwiched between cadmium telluride (CdTe). They measured a conductance of $\sim 2e^2/h$ in transport measurements, whereas a trivial insulator would show zero conductance. The list of 2D TI materials has been expanded [20] to structures not only formed by quantum-wells. In many of them, the topological interface is achieved between the non-trivial insulator and air or vacuum acting as a trivial insulator.

Considering the QSHE in three dimensions brought L. Fu et al. to predict the existence of three-dimensional TIs [11, 21], in which the topological transition is extended to a two-dimensional interface between the non-trivial and a trivial insulator. The one-dimensional helical edge state present in 2D TIs can be generalized to surface states in 3D TIs, consisting of massless Dirac fermion states dispersing linearly with $\mathbf{k}$, that is forming a Dirac cone. Analogously, spins of the TSS carriers are always aligned orthogonally to their momentum (i.e. subject

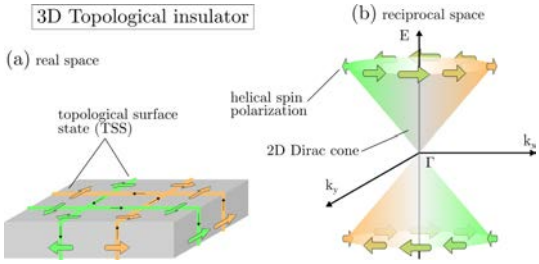

Figure 1.1: Schematic of (a) real space picture of a 3D TI showing the spin current flow at the TSS, and of (b) the energy dispersion of the TSS. It forms a single 2D Dirac cone with helical spin texture, which forbids backscattering involving k of opposite sign. Green and orange depict spin polarization along the k_x axis.

to spin-momentum locking), and mostly lying within the surface plane [22], as depicted schematically in Figure 1.1. The Quantum Spin Hall phase in a 3D material was identified in 2008 by D. Hsieh et al. [23] in the bulk alloy $Bi_{1-x}Sb_x$. Shortly after, a new generation of TIs with well-separated bulk and surface electronic structure, and with a relatively large bulk gap of ~ 0.3 eV, was proposed and experimentally confirmed in well-known thermoelectric materials, Sb_2Te_3, Bi_2Te_3 and Bi_2Se_3 [22, 24]. As of 2018, the list of TI materials has been expanded to alloys formed by not only chalcogen and pnictogen atoms, but also by other heavy elements with high spin orbit coupling such Pb, Sm, Sn, Y, Ir or Rh among others [13, 25–28].

Interfacing TIs with other kinds of trivial phases of matter can generate exotic electronic states and quasiparticles which are inaccessible in ordinary condensed-matter systems. Therefore, TIs become attractive for fundamental research in physics, and for future applications ranging from spintronic devices to quantum information processes, technologies that utilizes both the charge and spin degrees of freedom of electrons, to store, transmit and process information. Proximity-induced superconductivity in TIs is one of the phenomena that has attracted more attention during the last years, as it can lead to novel quantum phases such topological superconductivity or to unconventional Pearl vortices [29, 30] and Josephson effect [31, 32]. One particularly fascinating example is the emergence of Majorana fermions. These particles are their own antiparticle and were hypothesized by E. Majorana in 1937 [33, 34], in contrast to Standard Model fermions subject to the Fermi-Dirac statistics, possessing an associated antiparticle different from themselves. More than 70 years later, Majorana fermions were predicted to appear as quasiparticle excitations in a solid-state interface formed by a 3D TI and a conventional superconductor [35], and thereafter measured in different TI on s-wave superconductor systems [36].

Novel magnetoelectronic phenomena can also be induced when the helical spin-polarized surface states of a TI are in contact with magnetic materials. For instance the manipulation of electronic spins without the need of external magnetic fields, which is of particular interest in the field of spintronics, since the control of spin currents through charge currents and vice versa is essential for the realization of functional devices [37–39]. Edelstein effect [40] is one of those effects, consisting in a steady current J_x passing through a high spin orbit coupling material (like a TI) that creates a steady non-equilibrium spin polarization S^y. This polarization can be used to switch the magnetization of a ferromagnetic

overlayer [41, 42]. Conversely, in Inverse Edelstein Effect, a spin accumulation (induced by spin injection from a ferromagnet) in the interface with the TI generates a net charge current J_x [43]. More entangled magnetic interactions, such as ferromagnetic exchange, are expected to alter the bulk topology of a 2D TI, thus bringing it from a Quantum Spin Hall to a Quantum Anomalous Hall phase [44, 45]. The Quantum Anomalous Hall Effect (QAHE) can be viewed as the zero-magnetic-field version of QHE, in which the introduction of long-range ferromagnetic order to the system acts as an effective magnetic field and breaks TRS [46, 47]. In 2D TIs, a large enough ferromagnetic exchange splitting can bring one set of spin subbands to the topologically trivial phase [48], thus leaving only one single chiral edge state intact. That represents a one-dimensional channel where spin currents propagate in only one direction, which is of particular interest for applications in devices with reduced heat dissipation [49, 50], and in fault-tolerant quantum information processing [51]. In the 3D TI case, perpendicular ferromagnetic magnetization to the surface also breaks the TRS, being expected to open a gap at the Dirac point. If the strength of the induced magnetization is large enough, the bulk insulator evolves from a QSHE to a QAHE phase in which chiral states appear at the magnetic domain boundaries.

Prerequisites for the experimental realization of the mentioned spin-related effects are the null contribution of bulk channels to the transport and long-range magnetic order. Non-perturbative interactions between magnetic materials and TIs would ensure the stability of the respective TSS and magnetic properties, maintaining also the bulk insulating character. Nevertheless, fulfilling these requirements simultaneously has arisen to be a very challenging task, as it will be reviewed hereunder.

The ultimate aim of this thesis is to assess these requirements by interfacing high-quality TIs with well-ordered magnetic Metal-organic (MO) frameworks. Molecular Beam Epitaxy (MBE) has been proved to be the most suitable growth method for fine-tuning the electronic properties of TIs due to its ability to produce mono-crystalline thin films with accurate control over the chemical composition, structural defects and film thickness [52]. After the introductory Chapter 1 and description of the experimental techniques in Chapter 2, Chapter 3 focuses on the growth of chalcogen-based TI materials, i.e. the "Bismuth Telluride (Bi_2Te_3) family". They posses a van der Waals (vdW)-layered structure formed by Quintuple-layers (QLs) along the {111} crystallographic direction, which make them ideal TIs for MBE. Each QL consists of five atomic rows following the Te(1)-Bi-Te(2)-Bi-Te(1) sequence. The insulating behaviour of this family of TIs critically depends on their doping level, a challenging task in which alternative growth methods have typically failed [53–55]. In contrast, MBE capabilities allow a precise positioning of the Fermi Level (E_F), leading to pure bulk insulating films [56–60]. In part, this explains why QAHE has only been observed in MBE-grown TI samples [45].

On the other hand, several strategies have been followed to date aiming at introducing magnetic order in the TI, which can be divided into two main approaches: the introduction of magnetic impurities in the bulk during the crystal growth or the on-surface deposition of magnetic materials. The latter is foreseen

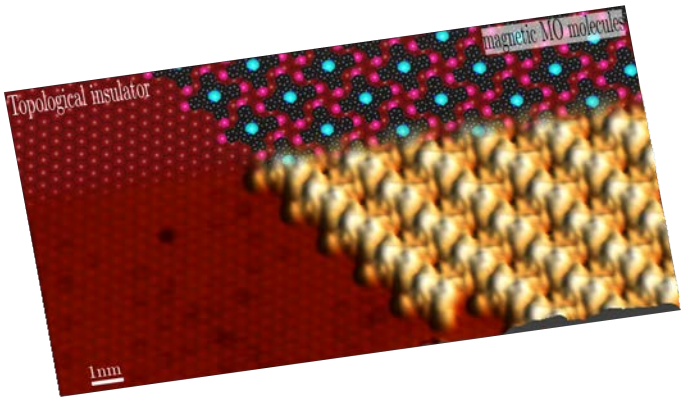

Figure 1.2: MO / TI heterostructure: 3D representation of a STM image (−1.8 V, 0.009 nA) of CoTBrPP molecular layer on $Bi_2Te_3(0001)$ surface, together with their corresponding molecular and crystal models (C: black, Co: light blue, N: dark blue, Br: pink, Te: maroon).

to allow independent engineering of the properties of the magnetic agent, such as the magnetic anisotropy, moment and order, and of the TI, such as the doping level and band bending. This would minimize the effect in the bulk properties, which could impact negatively the TSS. In this context, ferromagnetic thin films on TIs have been widely studied, finding that strong interactions can take place at the interface, such as atomic interdiffusion and hybridization. These may result in undesirable alloy formation, spin scattering or shunting effects, and eventual creation of interfacial "dead" layers that force the insertion of a less reactive spacer [43, 61] to pull the TSS apart from the magnetic material. This phenomenon has been observed for a large variety of 3d metals [62–67], evidencing the need to find an approach that involves weaker interactions. Alternatively to magnetic films, on-surface deposition of single magnetic adatoms has also been explored. Adatoms clustering [68] or segregation [69, 70] to the TI bulk, but more importantly the lack of control over the adsorption sites [71–76], can induce uncontrolled strong interactions like significant doping or hybridization that compromise the stability of the TSS. This makes this approach inefficient for controlling the magnetic order and anisotropies.

In this thesis we use MO frameworks hosting magnetic ions on TI surfaces, which is a promising approach for controlling interfacial interactions and overcome the above-mentioned drawbacks. Advantageous aspects of molecules over inorganic matter are: (i) structural perfection, specially at lower temperatures; (ii) small size, making them ideal building blocks for functional nanostructures; (iii) self-assembly and recognition [77, 78], leading to changes in the electronic structure, that may enable switching and sensing functionalities [79]; (iv) dynamical stereochemistry, providing multiple-functionality properties [80, 81]; (v) synthetic tailorability, allowing the rational design of structural, bonding, transport and optical properties [82]. The understanding [83] and exploitation of such features has already led to the creation of numerous applications in nowadays molecular electronics [84, 85], sensors [86], filtering [87] and energy production [88]. In this context Chapter 4 presents a detailed study illustrating how the magnetic interfacial interactions between a Co atom and a Au(111) surface can

be tuned by caging it in slightly different molecular ligands.

MO molecules have been traditionally explored on metallic surfaces in an extensive manner [89–96], and only a few works devoted to their study on TI surfaces have been published. These have confirmed the high tunability of interfacial interactions [97, 98], at the same time showing that the stability of the TSS can be compromised for certain MO / TI systems [99]. Therefore, further endeavour is needed in order to control these always delicate interfacial interactions.

Chapter 5 of this thesis reports a comprehensive study of the interface formed by self-assembled magnetic MO structures, meanwhile on-surface synthesized MO coordination structures are assessed in Chapter 6, constituting the first study in the literature in which on-surface reactions of MO molecules on TI are achieved. The interest in such structures relies in the fact that coordination bonds enhances strong magnetic interactions (ferro- or antiferro-magnetic exchange), thus promoting the emergence of magnetic order [97, 100–102].

The MO / TI heterostructures studied in this thesis have been characterized in a thorough manner, structurally by Scanning Tunneling Microscopy, chemically by X-ray Photoemission Spectroscopy, electronically by Scanning Tunneling Spectroscopy and Angle-Resolved Photoemission Spectroscopy and magnetically by X-ray Magnetic Circular Dichroism. Experimental results were frequently supported computationally by Density Functional Theory, in collaboration with R. Robles. These are introduced in Chapter 2, highlighting that in order to make a study at the atomic level like this, all sample preparation and characterization processes have been carried out at cryogenic temperatures and under UHV conditions.

Chapter 2

Experimental Techniques

Samples studied over the course of this thesis comprised heterostructures formed by Metal-organic (MO) molecules and Topological Insulator (TI) materials. They were prepared following this methodology: TI thin films were grown by Molecular Beam Epitaxy (MBE) in Ultra High Vacuum (UHV) conditions, and subsequently transferred to the pertinent ex-situ characterization setup. TI films were capped with a protective metallic layer in order to avoid surface degradation during the transfer. Subsequently, the protective layer was thermally removed, and MO molecules were deposited on the fresh TI surfaces by thermal evaporation.

In this chapter we introduce the main experimental methods used: the growth technique for the synthesis of the TI thin films (MBE), and the techniques to characterize morphologically, electronically, chemically and magnetically the MO / TI heterostructures. The latter include Scanning Tunneling Microscopy (STM), X-ray photoemission (XPS/ARPES) and X-ray absorption spectroscopic techniques (XAS/XMCD). The introduction is followed by a brief presentation of the actual setups and description of the sample preparation methods.

2.1 Molecular Beam Epitaxy

Molecular Beam Epitaxy (MBE) is an experimental technique that consists in growing single crystal films at UHV conditions, by condensation of molecular or atomic beams on a crystalline substrate. It was developed in 1968 by A. Y. Cho and J. R. Arthur[103], and it is nowadays widely used in the semiconductor industry and nanoscience research.

MBE offers a fine control over the growth parameters, and it is carried out in the contaminant-free UHV environment, permitting the fabrication of ultra clean crystals. A suitable choice of source materials and precise control over their evaporation rates allow the introduction of extrinsic dopants with atomic precision, the growth of layered heterostructures with atomically sharp interfaces, and of ternary compounds with precise stoichiometry. Additionally, the tunability of the substrate temperature widens the control over the kinetic processes occur-

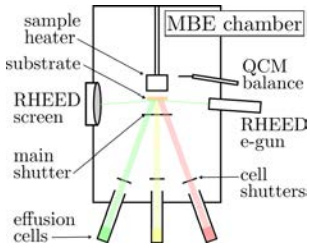

Figure 2.1: Schematic of an MBE chamber used for the growth of TI thin films.

ring during the growth, allowing engineering of atomic vacancies and density, size or shape of crystalline domains.

2.1.1 Implementation

The growth of films is performed by directing one ore more molecular or atomic beams onto a heated substrate, as it is schematically shown in Figure 2.1. Beams are generated by heating the material sources in thermal effusion cells. Working in UHV environment allows the mean free path of the atoms or molecules to be much larger than the geometrical size of the chamber in order to avoid particle scattering and beam dispersion. Meanwhile, the substrate is heated (generally at a constant temperature) in order to enhance the catalytic activity and difussion in its surface and favour the growth of crystalline materials.

2.1.2 Epitaxial Growth Mechanisms

The word epitaxy has its origin in the Greek roots *epi* ("above") and *taxis* ("an ordered manner"). In the context of materials fabrication, it refers to the growth of single crystalline materials on top of a substrate with similar structure. When the substrate and the grown material are not the same, it is referred as heteroeptiaxy. The growth mode and final material are determined by thermodynamics, that is the balance of energies between static states, and kinetic considerations, that is the competition between dynamic processes occurring at the surface.

The thermodynamics of a growth process is determined by the surface energy of the film to be grown (γ_{film}), the surface energy of the substrate (γ_{subs}) and the interface energy ($\gamma_{film-subs}$which incorporates the difference in lattice structure, hybridization and strain). These magnitudes are related through the Bauer criterion for wettability[104], and its compliance determines the energetic conditions for three different growth mechanisms:

- Frank-van der Merwe:
  $\gamma_{film} - \gamma_{subs} + \gamma_{film-subs} < 0$ makes the substrate surface area to be minimized, inducing the film to grow atom-layer by atom-layer (2D growth in Figure 2.2a).

- Stranski-Krastanov:
  $\gamma_{film} - \gamma_{subs} + \gamma_{film-subs} \lesssim 0$ together with elastic energy produced by a large lattice misfit provokes a sequence of layer-by-layer growth followed

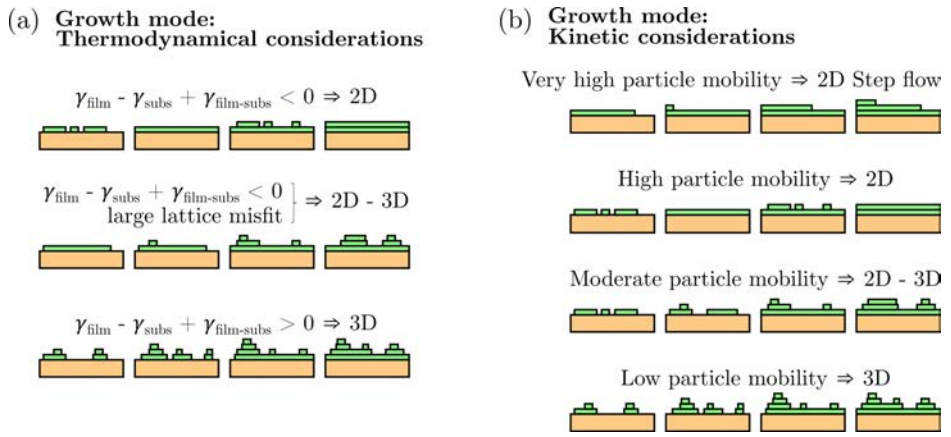

Figure 2.2: (a) Schematic showing how the growth mode depends of the substrate surface, film surface and interface energy γ_i, and by the lattice misfit. (b) Effect of the particles mobility in the growth method.

by the formation of three dimensional islands (2D to 3D growth in Figure 2.2a).

- Volmer-Weber:
  $\gamma_{film} - \gamma_{subs} + \gamma_{film-subs} > 0$ forces the interface and film surface area to be minimized, promoting the film to be grown through the formation of three-dimensional nuclei (3D growth in Figure 2.2a).

Furthermore, surface defects such as vacancies, antisites, adatoms or structural defects constitute another important growth parameter that can have great impact on the surface and interface energies γ_i. They tend to act as nucleation centres, which can induce the formation of in-plane rotated crystalline domains, and favour the 3D growth. Therefore, from the thermodynamic point of view, the most suitable choice of substrates for the growth of single crystalline films are those with atomically clean flat surfaces, small lattice misfit, and fulfilling the relation $\gamma_{film} - \gamma_{subs} + \gamma_{film-subs} < 0$.

In the situation in which no dangling bonds and only van der Waals (vdW) like forces act across the film-substrate junction, that is in the limit where $\gamma_{film-subs} \to 0$, heteroeptiaxial growths of layered materials such as graphite, MoS_2 or chalcogenide-based TIs can be achieved. This growth technique is known as van der Waals epitaxy, and it was experimentally realized for the first time by A. Koma [105]. And even if it was initially limited to the growth of layered material onto another layered material substrate, it was later extended to the heteroepitaxial growth onto 3-dimensional crystal substrates. Due to the weak interaction between substrate and film, the lattice matching condition is drastically relaxed, and an epilayer can be grown from the beginning with its own lattice constant, with an interface with very low amount of defects is formed, extending the growth to a large variety of different heterosctructures.

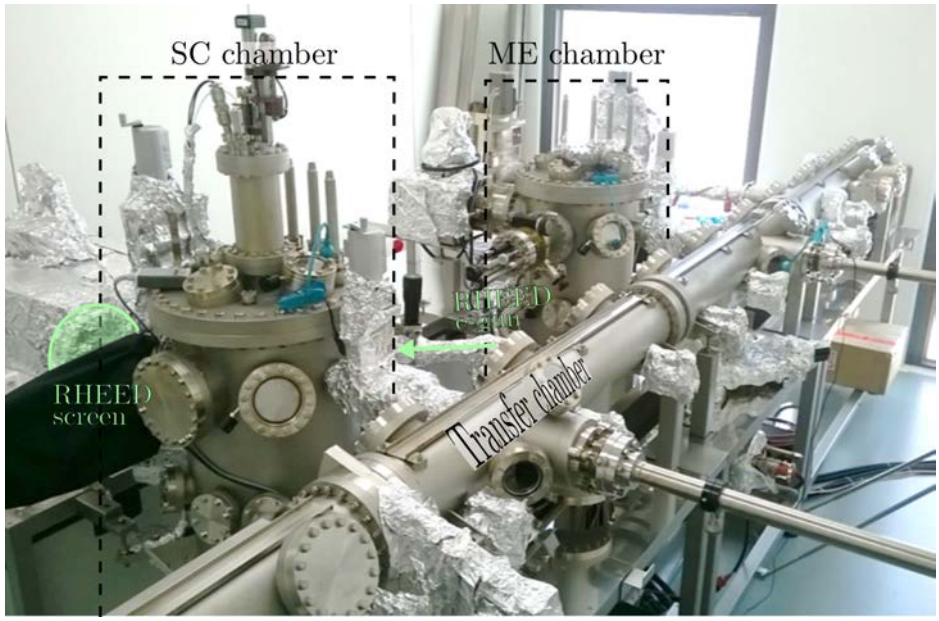

Figure 2.3: The MBE setup at ICN2, formed by two growing chambers, one devoted to the growth of semiconductors (SC) and the other of metals (ME). A transfer chamber enables the UHV connection between them.

The kinetic processes occurring at the surface further determine the growth mode beyond the thermodynamic conditions imposed by the film-substrate balance. Atoms or molecules reaching the substrate surface can be either adsorbed or reflected, and their ratio determines the sticking coefficient. Adsorbed species may experience surface diffusion, diffusion across steps, along edges, clustering or even desorption. Thus, the deposition rate $\frac{d\theta}{dt}$ can be described by

$$\frac{d\theta}{dt} = S\phi - \frac{\theta}{\tau_{des}}, \tag{2.1}$$

where θ is the coverage, S the sticking coefficient, ϕ the species flux, and τ_{des} the desorption characteristic time.

These processes are controlled by the substrate temperature and evaporation rates, which can be adjusted by the temperature of evaporation cells. High substrate temperature imprints higher particle mobility at the expense of lower sticking coefficient and higher desorption probability. Highly mobile particles favour the 2D growth, as they have larger surface diffusion lengths, and their probability to get anchored in a nucleation site or step is reduced. Figure 2.2b shows how the particle mobility affects the growth mode. In parallel, high evaporation leads to a larger number of particles reaching the surface. It makes them more likely to interact leading to clustering, and hence promoting the 3D growth (i.e. kinetic roughening).

2.1.3 Experimental Setup

TI thin films were grown in an MBE chamber by Createc Fischer & Co. GmbH Erligheim (Germany), shown in Figure 2.3a. The setup consists of two deposition chambers, one devoted to the growth of metallic alloys (ME chamber) and another one to chalcogenide semiconductors (SC chamber). Figure 2.3 shows an schematic of the SC chamber used for the growth of TIs. Both of them can host seven effusion cells, that consist of a ceramic crucible surrounded by a resistive filament. They are filled with the material sources to be evaporated, such as Bi, Sb, Te or Se for the SC chamber, and Ag, Al Co, Fe, MgO or NiFe for the ME chamber. The substrate is placed facing downwards with a resistive heater behind. Samples can reach 800°C, and the whole heater with sample can rotate continuously during the growth if needed, in order to achieve a homogeneous growth. Each effusion cell and sample holder has its own mechanical shutter, in order to minimize the contamination to the substrate and to the whole chamber due to the heating, thermalization or calibration processes. Moreover, Bi, Sb and Te cells are equipped with a second resistive filament, the cracker cell, which is placed at the very output of the cell and it is heated above the evaporation temperature. The aim of it is to favour pure atomic vapour beam of those materials that tend to form molecular species or bigger clusters.

Taking advantage of the UHV environment, the MBE setup possesses a Reflection High Energy Electron Diffractometer (RHEED) as an in-situ characterization tool that allows real time monitoring of the film surface structure during growth. RHEED is a 2D sensitive diffraction technique in which an electron beam of $E_\gamma = 15\text{keV}$ ($\lambda \sim 0.1$ Å) is directed to the surface sample at grazing incidence ($\sim 1°$, implying a penetration depth of ~ 1 nm and coherence length of ~ 5 nm). Diffracted electrons are collected in a fluorescent screen, creating a diffraction pattern that results from the intersection between the e-beam Ewald sphere and the crystal surface periodicity. Figure 2.4 shows how different structural features can be distinguished in a RHEED measurement. A RHEED RCU commercially available by Dr.Gassler Electron Eevices GmbH Ulm (Germany) was used in this thesis.

2.2 Scanning Tunneling Microscopy

Scanning Tunneling Microscopy (STM) is an experimental technique in surface science that allows direct imaging of conducting and semiconducting surfaces down to the atomic scale. Additionally, STM provides access to local spectroscopy at the molecular or atomic scale, allowing spatially resolved imaging of the electronic structure of the sample. Since its development in 1981 by G. Binning and H. Rohrer,[106] STM has become an important and widely used tool for fundamental studies of quantum mechanical properties of matter, for probing on-surface chemical reactions and for assessing 2D self-assembled structures, among others.

The working principle of an STM is based on quantum tunneling. A metallic

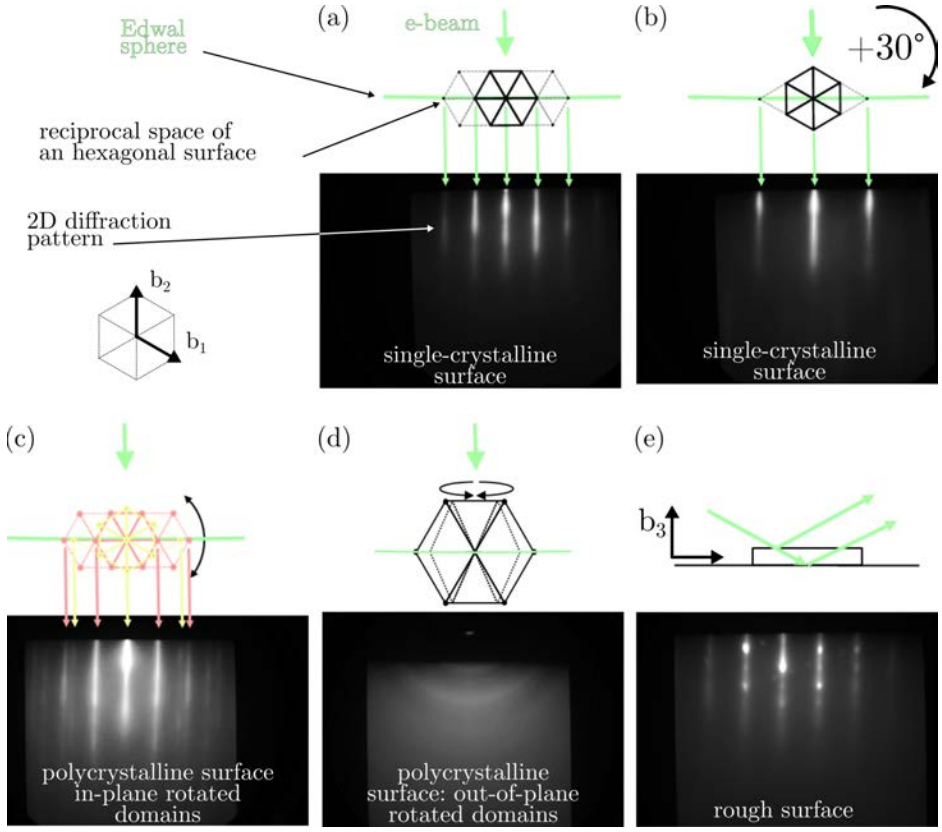

Figure 2.4: RHEED patterns for different films of a topological insulator as an example, together with the corresponding schematic showing the intersection of the Ewald sphere with the nodes of the reciprocal lattice of the hexagonal surface. (a) and (b) correspond to the same single-crystalline film, but with the incidence azimuthal angle rotated 30°. Pattern in (c) corresponds to a polycrystalline film possessing domains azimuthally rotated; Bragg diffraction condition is fulfilled by a continuous of rotational domains presented in (a) and (b) due to the screen dimensions. Pattern in (d) corresponds to a sample with rough surface, as the spots observed are an indication of 3D diffraction contribution.

and very sharp tip (ideally terminated by a single atom) is placed at a distance of about $1 - 10$ Å to the sample to be studied. When a bias voltage is applied between sample and tip, electrons tunnel from one to the other generating a measurable current. This current depends exponentially on the tip-sample distance, which allows extremely precise detection of changes in the sample-tip distance, typically in the range of 10 pA to 10 nA. If the tip scans an area of the surface, the current signal recorded point by point generates an image of the topography in real space.

2.2.1 Quantum Tunneling

According to classical mechanics, a particle of with mass m moving in a 1-dimensional space could never cross a potential barrier U if its kinetic energy is $E_k < U$. However, if the dimension of the system is reduced enough for quantum mechanics to be relevant, the system is described by the Schrödinger equation

$$-\frac{\hbar}{2m}\frac{d^2}{dz^2}\psi(z) + U(z)\psi(z) = E\psi(z), \tag{2.2}$$

where $\psi(z)$ is the wave function of the particle. For simplicity, the potential barrier can be considered as

$$U(z) = \begin{cases} U & \text{if } 0 \leq z \leq d \\ 0 & \text{if } z < 0,\ z > d, \end{cases} \tag{2.3}$$

Now, combining 2.2 and 2.3 we obtain

$$\psi(z) \propto e^{ikz}, \tag{2.4}$$

with

$$k = \hbar^{-1}\sqrt{2m(E - U(z))}, \tag{2.5}$$

where k is the particle wave vector. $U(z) \leq E$ has now physical meaning as κ can take imaginary values, which means that the Schrödinger equation 2.2 has solutions for any z value. These are

$$\psi(z) = \begin{cases} \psi(0)e^{ikz} & \text{if } z < 0 \\ \psi(0)e^{-\kappa z} & \text{if } 0 \leq z \leq d \\ \psi(0)e^{-\kappa d}e^{ikz} & \text{if } d < z, \end{cases} \tag{2.6}$$

where $\psi(0) \in R$ and $\psi(0) < 0$ for simplicity, and

$$\kappa = \hbar^{-1}\sqrt{2m(U - E)} = ik \in R. \tag{2.7}$$

The particle can now be found in z regions that were forbidden according to the classical approach. In other words, the particle has a finite probability to cross the potential barrier, which increases as the barrier height U decreases and

decays exponentially with the barrier width d. The transition probability T can be deduced from equation 2.6

$$T(z<0 \rightarrow z>d) = \frac{|\psi(z<0)|^2}{|\psi(z>d)|^2} = e^{-2\kappa d} \tag{2.8}$$

for $a<0$ and $b>d$.

In STM, tunneling processes occur when the tip is placed close enough to the sample to allow surface electrons tunnel to the tip (and vice versa). The tip - sample distance determine the width of the tunnel barrier, while the barrier height is defined by the energy needed to pull one electron from the surface to the free state, i.e. the work function Φ of the material. Hence, equation 2.8 can be rewritten in the form of

$$T_{sample \rightarrow tip} = \frac{|\psi_{tip}|^2}{|\psi_{sample}|^2} = e^{-\frac{2d\sqrt{2m_e\Phi}}{\hbar}} = e^{-1.02d\sqrt{\Phi}}, \tag{2.9}$$

where tip and sample are considered to be at the same potential ($E=0$), and d is expressed in Å and Φ in eV.

Going beyond the described 1D model requires the inclusion of the electronic structure of the tip and sample, and the geometry of the system in the three dimensions. In 1961, Bardeen introduced a first-order perturbation theory model [107], where the problem is described by the tunnelinng matrix $M_{\mu,\nu}$ that represents the overlap of the wave functions of the tip ψ_μ and sample ψ_ν. The transmission probability is now determined by

$$T = \frac{2\pi}{\hbar}|M|^2\delta(E_\mu - E_\nu), \tag{2.10}$$

where E_μ and E_ν are the tip and sample energies respectively.

In absence of a differential potential between tip and sample, there is not imbalance in the number of electrons tunneling. However, adding a bias voltage between sample and tip induces a net tunneling current flow

$$I = e\int_0^{eV} \rho_\mu(E_F - eV + \epsilon)\rho_\nu(E_F + \epsilon)Td\epsilon, \tag{2.11}$$

where $\rho_\mu(\varepsilon)$ and $\rho_\nu(\varepsilon)$ are the density of states of tip and sample respectively. Depending on the sign of V, electrons tunnel from occupied states of the tip to unoccupied states of the sample, or from occupied states of the sample to unoccupied states of the tip, as it is schematically represented in Figure 2.5.

In 1985, Tersoff and Hammann extended Bardeen's approach by introducing the effect of the electronic structure of the sample and tip geometry [108]. Here, the sample is considered to be a perfect flat surface whose states have a wave function that decays exponentially outside the sample in the perpendicular direction, and the tip is considered to be a sphere. Then, the following expression of the tunneling current is derived as follows:

$$I = 32\frac{\pi^3}{\hbar k^4}e^2V\Phi^2R^2e^{2kR}\frac{1}{V_{tip}}\sum_{\mu,\nu}|\psi_\nu(\boldsymbol{r_0})|^2\delta(E_\mu - E_F)\delta(E_\nu - E_F) \tag{2.12}$$

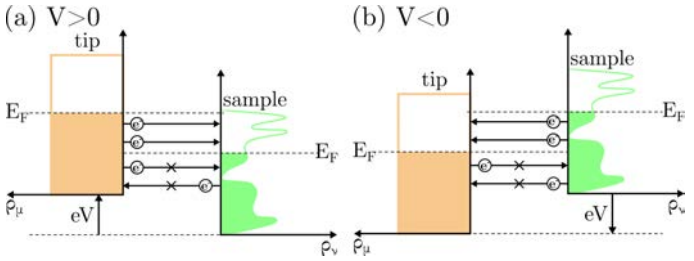

Figure 2.5: Energy schematic of the quantum tunneling process when a bias voltage V is applied. (a) Positive/negative bias allows the inspection of unoccupied/occupied states of the sample.

$$I \propto V \rho_{Tip}(E_F)\rho_{Sample}(E_F, \boldsymbol{r}_0), \tag{2.13}$$

where V_{tip} is a normalization constant related to the volume of the tip, and $\boldsymbol{r}_0$ is the center of the tip with radius R. A more realistic description defines the tunneling current by generalizing the integration over all states contributing to the tunneling current, that is over the surface and tip Density of States (DOS) with energies between E_F and $E_F + V$ [109–111].

$$I = \int_{E_F}^{E_F+eV} \rho_{sample}(\varepsilon - eV)\rho_{tip}(\varepsilon)T(d, \varepsilon, V)d\varepsilon \tag{2.14}$$

Thus, the tunneling current is primarily dependent on the convolution between the DOS of the tip and sample, integrated from E_F to the applied bias voltage $E_F \pm V$. Although the assumptions taken with this model do not represent a complete description of the tunneling process, it provides a reasonable picture for many standard situations in an STM.

2.2.2 Scanning Tunneling Microscopy

As explained in the preamble of this section, an STM measurement consists in the acquisition of an image representing the real space of a certain area of the sample. To do that, a bias voltage (V) inducing a tunneling current I is applied between the tip and the sample. The tip moves within a xy plane at a distance d from the sample surface, describing a scanning movement consisting of parallel straight lines that eventually cover the whole measured area. Since the scanning lateral length typically range from 1 to 1000 nm, the tip x- and y-motion has to be controlled in a very precise manner. This is achieved by applying directional voltages (U_x, U_y) to a piezoelectric actuator. The z component of the image is formed as a result of changes in the tunneling conditions, primarily due to surface morphology and local electronic structure. It depends on the free tunneling parameter during the acquisition (I or d), by setting either constant current or constant height mode.

In constant current mode (Figure 2.6a), the bias voltage V and tunneling current I are fixed and set by the user. A feedback loop reads the small deviations in I and applies a third voltage U_z to the piezoelectric actuator in order to keep the required distance d for the fixed V and I values. The U_z signal is recorded and mapped over (U_x, U_y), and it can be transformed to $z(x, y)$ by

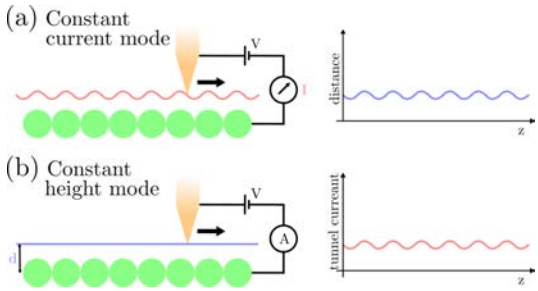

Figure 2.6: STM scanning modes. Representation of the scanning measurement (left column) and corresponding line scans (right column), for (a) constant current and (b) constant height modes.

knowing the X, Y and Z mechanical response to the voltage. The z component represents a surface of constant DOS, involving convolution between topography and electronic structure. Hence, it can not be interpreted as a direct topographic image.

On the other hand, in constant height mode (Figure 2.6b), I is left as free parameter and is determined by the user-fixed V and d. The tip scans over the sample at a constant d while recording the tunneling current, which generates an $I(U_x, U_y)$ map that can be converted to $z(x, y)$. The resulting images can not be interpreted as pure topography either, as the $I(x, y)$ signal is a constant integral of the DOS emerging from the sample surface.

Constant current mode is generally used for imaging large areas, as the feedback prevents the tip from crashing. However, the drawback of this mode is the slow scanning velocity limited by the feedback. On the other hand, constant height mode allows faster velocities, only limited by the pre-amplifier. It is commonly used for smaller and nearly atomically flat areas as it gives a "clean" picture completely independent from the feedback-induced artefacts.

2.2.3 Scanning Tunneling Spectroscopy

One of the main advantages of STM over other microscopy techniques is that it can acquire spectroscopic information about the electronic structure with molecular or atomic precision. Contrary to the STM scanning modes, in Scanning Tunneling Spectroscopy (STS) the bias voltage is not kept fixed. The tip is positioned over the point of the sample to be studied, and V is swept over the range of interest while the feedback loop is opened to allow I to vary, while keeping d constant. Making the derivative of equation 2.13 over V and assuming a metallic tip with a continuum of states near E_F, one can see that the differential conductance dI/dV is directly proportional to the local DOS at at applied bias voltage V_0,

$$\left.\frac{dI}{dV}\right|_{V_0} \propto \rho_{sample}(E_F - eV_0) \tag{2.15}$$

The differential conductance can be obtained numerically from the measured $I(V)$, however using a lock-in amplifier to directly acquire dI/dV leads to a higher signal to noise ratio and to a wider dynamic range. The working principle of a lock-in consists in the addition of a small sinusoidal voltage modulation to the

bias voltage, which results in a sinusoidal response in the tunneling current. For a given voltage modulation, the induced current amplitude is proportional to the slope of the $I(V)$ curve, i.e. to dI/dV. The amplitude and frequency of the signal modulator, as well as other lock-in parameter such as the time constant of the filter and sensitivity, have to be adjusted for every measurement in order to optimize the signal to noise ratio, energy dI/dV resolution, and acquisition time.

Applying high bias voltages with the tip fixed at close distance to the sample can modify the physical or electronic structure of the tip and sample in a undesired manner. In order to acquire electronic information within a higher range of V values and in a less invasive manner, the Scanning Tunneling Spectroscopy (STS) can also be operated in constant current mode. In this case V is swept while d is automatically adjusted to keep I constant.

A very powerful application of STM lies in the possibility of resolving spatially the electronic features found in STS. For this purpose, differential conductance maps can be taken, by measuring the dI/dV signal at each point of a scan. The results can not be interpreted as direct DOS maps at a certain height, as the morphology of the sample affects the tip - sample distance magnifying or reducing certain spectral features. This is the case of some of the molecules studied in this thesis, whose conformation upon adsorption on certain surfaces may alter the appearance of some molecular orbitals in the conductance maps. In order to decouple the electronic from molecular morphological contributions, complementary constant current and topographic measurements have been performed. Moreover, the time needed for every dI/dV acquisition can vary between a few minutes to some hours, causing that the effect of thermal drift may become important. In order to counteract it, adjustments in the x, y and z directions must be performed routinely.

2.2.4 Experimental Setup

The STM setup used in this thesis was a low temperature (LT-)STM commercialized by Createc Fischer and Co. GmbH Berlin (Germany) [112], based on a design by G. Meyer [113] (Figure 2.7a). The system operates in UHV ($p < 1 \cdot 10^{-11}$ mbar), at temperatures around 5 K by using a liquid helium bath cryostat, and it is isolated from mechanical vibrations with pneumatic dumpers. The STM setup consists of two chambers, one intended for sample preparation and a second for the STM/STS measurements.

The STM head, which is the principal part of an STM, uses three piezo tube actuators that move the tip macroscopically over the sample, and approach it to the surface until a tunneling current is detected. Maximum x and y range are approximately $4 - 5$ mm, and 300 μm for the range in z. A fourth piezo tube performs the actual x-y-z positioning during the STM and STS measurements. An in-situ exchangeable tip holder, attached at the end of the fourth piezo tube, holds the tip. The tips used during this thesis have been made in-house by cutting iridium and platinum wires with a sharply-edged blade.

Measurements on TI samples were performed using an in-house adapted LT-STM Createc sample holder (Figures 2.7b and 2.7c). Due to the low DOS at the

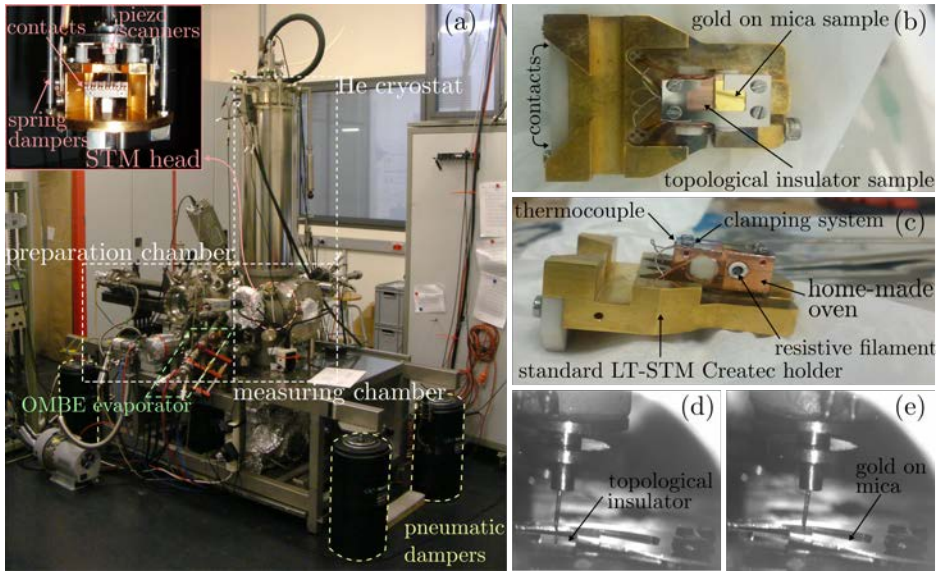

Figure 2.7: (a) The low temperature STM setup and (inset) the STM head, located below the cryostat. Top (b) and side (c) view of the in-house adapted Createc sample holder. This sample holder is placed between the piezo scanners and contacts of the STM head in order to perform measurements. Tip placed in tunneling regime above (d) the TI and (e) Au on mica samples.

surface of TIs, the STM tip has to scan at closer distances than in conventional measurements with conductive novel metals. Hence, the probability for the tip to interact destructively with the surface increases, and it has to be repaired more frequently. Since nobel metal surfaces are commonly used for this purpose, we designed and built an oven capable of holding a TI and a Au on mica sample. The tip could then be prepared without using an additional Au sample, which would imply transferring the TI sample out of the low temperature conditions, and the consequent contamination of its surface.

2.3 X-ray Photoemission and Angle-Resolved Photoemission Spectroscopies

X-ray Photoemission Spectroscopy (XPS) and Angle-Resolved Photoemission Spectroscopy (ARPES) are experimental techniques that give quantitative spectroscopic information of surface electronic properties. The working principle of both techniques is base on the photoelectric effect, discovered by R. Hertz in 1887 [114] and later explained by A. Einstein [115, 116].

X-ray Photoemission Spectroscopy (XPS) was developed in 1967 by K. Siegbahn [117], and it is used to spectroscopically investigate the chemical composition and structure of materials. In an XPS experiment, the energy distribution of the photoelectrons is measured, allowing spectroscopic information about the

sample DOS, from the Fermi level down to the core levels. Meanwhile in an Angle-Resolved Photoemission Spectroscopy (ARPES) experiment, the energy distribution is measured and resolved over photoelectron's momentum. ARPES is broadly considered the most powerful tool to investigate the electronic structure of solids.

2.3.1 The Photoelectric Effect

In the photoemission process, an electron is excited by a photon and gains enough energy to escape into the vacuum. In the case of solids, the electron is ejected if the adsorbed energy from the photon is larger than the sum of tis binding energy E_B and work function Φ of the host material. By conservation of energy, one can deduce that the kinetic energy of an emitted photoelectron is

$$E_K = h\nu - E_B - \Phi, \tag{2.16}$$

where $h\nu$ is the photon energy.

As discussed in the following subsections, the chemical composition, chemical bonding and (occupied) electronic structure can be obtained by measuring E_K. By adding angular information the electronic band structure or dispersion relation can be obtained.

2.3.2 X-ray Photoemission Spectroscopy

In an XPS measurement, an X-ray source emitting a monochromatic beam of photons is directed to the sample under study, which among other inelastic processes occurring inside the sample, induces the ejection of electrons because of photoelectric effect. Photoelectrons excited from atomic core levels can be probed, as the X-ray energies used can range from a few hundreds of eV to tens of keV. Therefore, quantitative information about the chemical composition, chemical state and electronic state of the elements can be obtained. A spectrometer measures the number of photoelectrons with respect to their kinetic energy, which leads to the energy distribution of photoelectrons in vacuum (i.e. electrons distribution in the occupied DOS of the sample).

Measured kinetic energy can be transformed to binding energy considering the schematic in Figure 2.8a. The energy transformations that a photoelectron undergoes when it is emitted from the sample and adsorbed by the spectrometer can be described by rewriting equation 2.16 as follows

$$\begin{aligned} E_K &= h\nu - E_B - \Phi_{sample} - (\Phi_{spec} - \Phi_{sample}) && (2.17)\\ &= h\nu - E_B - \Phi_{spec}, && (2.18) \end{aligned}$$

where Φ_{sample} and Φ_{spec} are the sample and spectrometer work functions. Then,

$$E_B = h\nu - E_K - \Phi_{spec}. \tag{2.19}$$

Therefore, the measured kinetic energy does not depend on ϕ_{sample}. This allows to directly transform from E_K to E_B by only knowing Φ_{spec}.

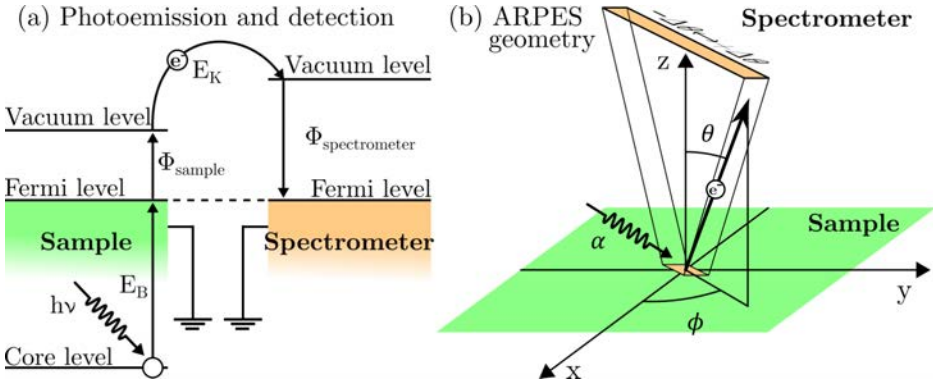

Figure 2.8: (a) Schematic of the energy transformations that a photoelectron undergoes when it is excited with energy enough to leave the sample and reach the spectrometer. (b) Schematic of a usual ARPES geometry. For every acquisition, the spectrometer measures the photoelectron intensity as a function of the kinetic energy and polar component of the emission angle.

It is important to draw special attention to the photoelectrons inelastic mean free path (IMFP) in matter, as it determines the probing depth of the instrument. Together with the photoionization cross section and transmission function of the analyser, IMFP have also to be taken into account in order to calculate the chemical composition of layered heterostructures like ours.

The behaviour of the electron mean free path (λ_{e^-}) with its kinetic energy obeys a universal curve [118], with small variations depending on the material. The photon energy used in this thesis has been $E_\gamma = 1486.6$ eV (see Section 2.3.4). Considering the core levels probed, the kinetic energies of the photoelectrons lie in the range of $\sim 300 - 1200$ eV, which results in an electron mean free path of ~7 and 10 Å. Therefore, the probing depth in our experiments is clearly determined by λ_{e^-}, and it is not higher than 1 nm.

2.3.3 Angle-Resolved Photoemission Spectroscopy

In addition to the energy resolution, in ARPES photoelectrons are discriminated with respect to their emission relative to the sample surface, which can be subsequently transformed to parallel momentum to the surface. This allows direct mapping of the occupied electronic structure, that is the occupied band dispersions of Bloch states for the case of the single-crystalline solids studied in this thesis.

Because of the crystal periodicity in the direction parallel to the surface of crystalline materials, and because of the negligible photon momentum for the typical energies used ($h\nu$ <10 keV), the parallel component of the crystalline momentum $k_\parallel$ is conserved. Therefore, the photoelectron parallel momentum out of the crystal $q_\parallel$ is related to the emission angles θ and ϕ by

$$\boldsymbol{q}_\parallel = (q_x, q_y) = \hbar^{-1}\sqrt{2m_e E_K} \cdot (sin\theta cos\phi, sin\theta sin\phi) \tag{2.20}$$

where m_e is the electron rest mass, and θ and ϕ the polar and azimuthal emission angles respectively. In the ARPES measurement, the azimuthal direction is generally fixed for every acquisition, obtaining a vertical section of the band structure in the (q_x, q_y, E_B) space. Additionally, a series of measurement scan be done while sweeping along the azimuthal direction in order to obtain the full $I_{photoem}(\theta, \phi, E_B)$ picture. The geometry of an ARPES setup is represented in Figure 2.8b. If one evaluates $I_{photoem}(\theta, \phi, E_B = 0)$, the DOS distribution in the reciprocal space (q_x, q_y) at the Fermi Level (E_F) is obtained. This sort of measurement provides information on the Fermi Surface (FS), and it is widely used to investigate, for instance, states contributing to the transport or charge transfer due to doping effects.

In contrast to the parallel component of the crystalline momentum, the perpendicular component is not conserved because of the lack of translational symmetry in that direction. Hence, it cannot be determined without additional information or certain assumptions (like free-electron-like final state bands). This is not relevant for 2D states as the Topological Surface State (TSS) studied here, since $\boldsymbol{k_z}$ components, which will be selected by the photon energy used.

The photoemission intensity can be derived from first order perturbation theory. The photocurrent generated in the transition between two Bloch states with energies E_i and E_f, and respective crystalline momentums $\boldsymbol{k_i}$ and $\boldsymbol{k_j}$ can be expressed as

$$j(E_K, \boldsymbol{q}_{\parallel}, h\nu) \propto \sum_{i,f,\boldsymbol{g}} T_f |M_{if}|^2 \delta(E_F - E_i - h\nu)\delta(\boldsymbol{k_f} - \boldsymbol{k_i})\delta(\boldsymbol{q}_{\parallel} - \boldsymbol{k_{f\parallel}} - \boldsymbol{g}), \quad (2.21)$$

where T_f is the transition probability of the final state to pass to the vacuum, δ operators account for energy and momentum conservation laws, $\boldsymbol{g}$ is a vector of the reciprocal surface lattice and $|M_{if}|^2$ is the transition rate matrix between the two Bloch ψ_i and ψ_j states. Following with the first order perturbation calculation, it can be found that $|M_{if}|^2$ is proportional to $\boldsymbol{A} \cdot \langle \psi_f | \nabla V | \psi_i \rangle$, with $\boldsymbol{A}$ the potential vector of the photon field, and V the crystal potential. This matrix component defines the allowed transitions according to the symmetry relations between the incident photon geometry and polarization, and initial and final wavefunctions. Therefore, the transition rate, and consequently the photocurrent, have their origin in the gradient of the crystal potential ∇V. The complete mathematical development can be found in [119].

2.3.4 Experimental Setup

Photoemission experiments were performed in the setup presented in Figure 2.9, consisting in the Phoibos 150 Analyser, the X-ray source XR50 M equipped with aluminium and silver targets, followed by the FOCUS 500 X-ray Monochromator, and the UVS 300 lamp followed by the TMM304 UV Monochromator. All these components are commercially available by SPECS GmbH Berlin (Germany). The setup also contains a sample manipulator with liquid nitrogen circuit to refrigerate samples. It is a flow cryostat that we used only with LN2, but can be

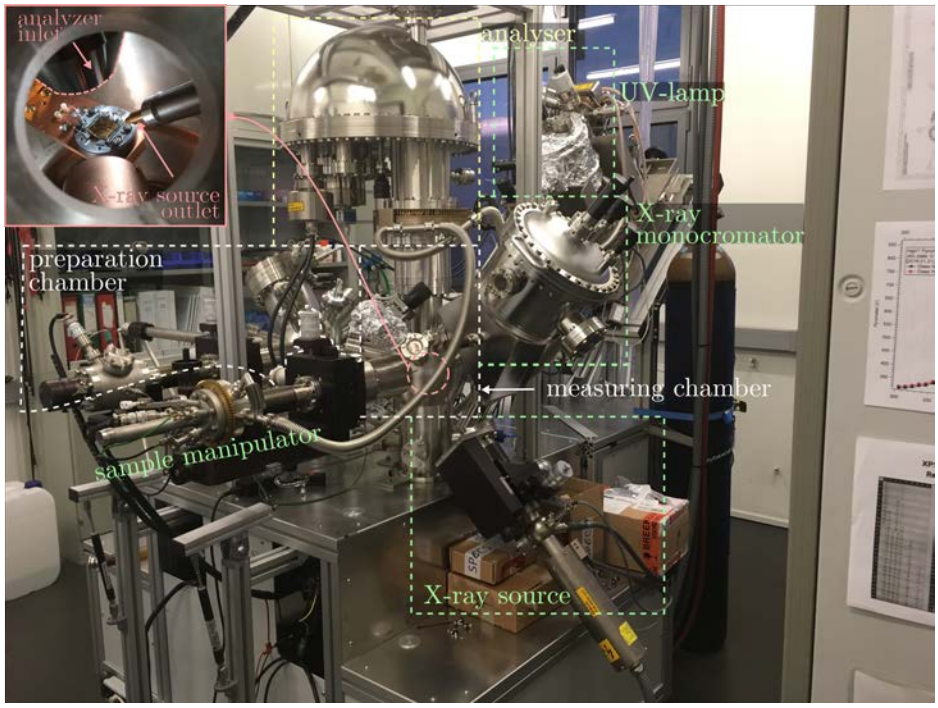

Figure 2.9: The XPS/ARPES setup, consisting of a chamber devoted to sample preparation, and the measuring chamber, equipped with the X-ray source and UV lamp, and corresponding monochromators. Inset: image of the X-ray source outlet, sample and analyser inlet geometry in XPS measurements.

used with LHe. For the XPS experiments, the photon energy was Al k-α line (1486.6 eV) provided by the X-ray source, while for the ARPES measurements, it was the HeI UV line (21.2 eV) provided by the UV lamp. Samples were kept at 80 K and in a pressure of $5 \cdot 10^{-10}$ mbar during the acquisition.

2.4 X-ray Absorption Spectroscopies

X-ray Absorption Spectroscopy (XAS) and X-ray Magnetic Circular Dichroism (XMCD) are an experimental technique that allows the study of electronic and magnetic properties of materials, offering elemental and chemical specificity and variable depth sensitivity. It is based on the magnetic circular dichroism effect, that is the differential absorption of left and right circularly polarized light by a material, in the presence of a strong magnetic field. Even though the effect had been theoretically described in the mid sixties [120, 121], due to the weak nature of the effect it was not untill twenty years later that the first XMCD detection was reported by G. van der Laan and collegues in 1986 [122]. For that, the use of synchrotron radiation as the circular polarized light source was crucial.

2.4.1 X-ray Absorption Spectroscopy

In a XAS experiment, the energy of a monochromatic X-ray beam is directed to the sample under study, and it is swept in energy over the desired range close to an edge jump. The fraction of X-ray absorbed is detected either directly by measuring the difference of incoming and transmitted intensities (transmission mode), or indirectly by measuring the intensity difference of the incoming beam and of the decay products such as fluorescent X-rays or Auger electrons (fluorescence or electron yield mode).

When X-rays interact with matter, the relation of incoming intensity I_0 and transmitted intensity I is given by

$$I = I_0 e^{-\mu(E_\gamma)t}, \tag{2.22}$$

where t is the material thickness in the direction parallel to the X-ray beam and $\mu(E_\gamma = h\nu)$ is the energy dependent X-ray coefficient, and can be approximated to $\mu \sim dZ^4/mE^3$ over large energy regions. Here d is the material density while Z and m are the atomic number and mass respectively, which means that the absorption coefficient decreases with increasing photon energy. Nevertheless, when the photon energy equals or exceeds the binding energy of a core level, a core electron is excited and a hole is created, leading to a new absorption channel. This provokes a sudden increase in the absorption coefficient, known as absorption edge. The core hole is filled in the fs time-scale by an electron from a higher energy state, and the corresponding energy difference is released via fluorescence or the emission of an Auger electron. A more detailed introduction to near edge strcture XAS is given in [123].

2.4.2 X-ray Magnetic Circular Dichroism

XMCD can be modelled using a two step model [124]. In order to understand the physical origin of this effect, let us consider a 2p photoelectron excited by circularly polarized X-ray photon. $2p_{1/2}$ and $2p_{3/2}$ are then involved in the so called L_2 and L_3 absorption edges. In the first step, part of the angular momentum carried by the photon is converted into spin momentum via spin orbit coupling as a consequence of the Fano effect [125]. The alignment between the helicity of the photon and the spin moment component parallel to the photon propagation direction determines the absorption. It leads to slight intensity changes between the signals acquired at opposite photon helicity, the L_2 and L_3 absorption edges in the case under consideration, as it is schematically shown in Figure 2.10. The second step is driven by the magnetic properties of the sample. The X-ray absorption is affected by the empty DOS available for a given angular momentum, which results from the symmetry of the initial core state and selection rules of the transition.

An XMCD spectra is obtained by making the subtraction between the two absorption spectra measured with opposite photon helicity. This difference, called dichroic signal, is related to a finite spin and orbital momentum by the so called

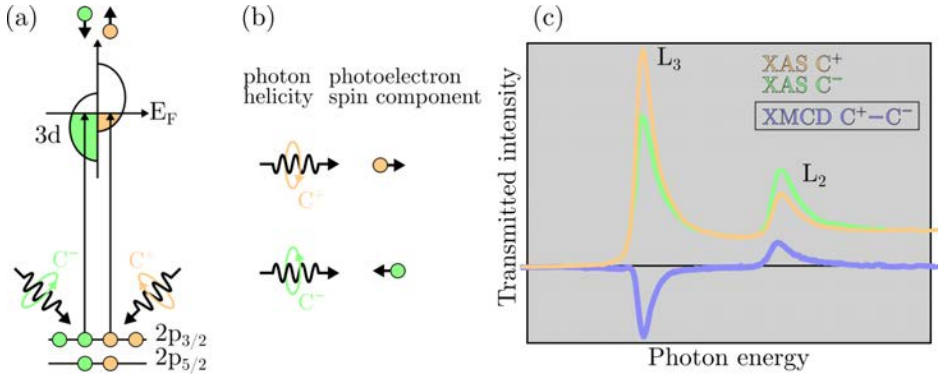

Figure 2.10: (a) Energy transitions promoted by circularly right (C^+) and left (C^-) polarized photons, involved in a 3d-metal with spin imbalance. (b) Momentum-spin coupling between photon and electron in function of the helicity of the circularly polarized photon. (c) Absorption spectra for (C^+) and (C^-) circularly polarized, and dichroic signal obtained from the subtraction

sum rules. In XMCD experiments, samples are generally exposed to high magnetic fields, low temperatures and different geometries in order to observe magnetic anisotropies. Hysteresis magnetic cycles can be measured as well, by detecting the dichroic signal at different intensities of magnetic field.

2.4.3 Experimental Setup

XMCD measurements are done using polarized synchrotron radiation due to the mentioned need of varying the photon energy. Synchrotron light offers a highly collimated and stable beam, with a high flux covering a broad spectrum from microwaves to hard X-rays. The photon energy can be continuously tuned and polarized linearly or circularly.

X-ray absorption experiments in this thesis were performed in the BOREAS beamline [126], at ALBA synchrotron. BOREAS is a soft X-ray beamline dedicated to polarization-dependent spectroscopic investigations comprised of two endstations; HECTOR, equipped with a 6T vector magnet, is instead devoted to XMCD measurements, and MARES, devoted scattering and reflection approaches. Our experiments were performed in HECTOR, measuring the total electron yield (TEY), using the photo-induced sample drain current. XAS and XMCD spectra were taken with right (C^+) and left (C^-) circularly polarized photons, in the presence of magnetic field (up to ± 6 T), at 7.5 K and with a base pressure of $1 \cdot 10^{-10}$ mbar. The geometry of the measurements is schematically shown in Figure 2.11a, together with the BOREAS experimental setup, in Figure 2.11b.

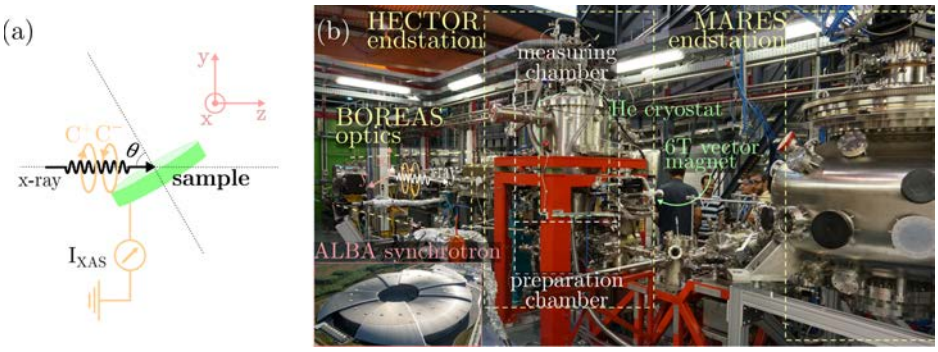

Figure 2.11: (a) Geometry of the XMCD measurement; circularly polarized photons are directed to the sample in the direction parallel to z axis generating a measurable photocurrent when they are adsorbed. The sample can be rotated an angle θ around the x axis, allowing the study of the angle dependent abortion in the range between grazing and normal incidence. (b) The BOREAS beamline composed by the beamline optics and HECTOR and MARES endstations. Pink axis are drawn in order to correlate the beamline geometry with the measurement geometry in (a). Inset: aerial picture of the ALBA synchrotron.

2.5 Sample Preparation Methods

Samples measured by STM during this thesis were composed by molecules adsorbed on two different substrates; Bismuth Telluride (Bi_2Te_3) thin films grown by MBE, and a Au single crystal. Therefore, different preparation methods were carried out for the two different families of samples measured.

Bi_2Te_3 thin films that were capped with a 20 nm protective Te layer in the MBE setup (Chapter 3) were exposed to air for less than 10 minutes during the transfer process to the STM setup. Once transferred, the protective Te layer was removed by annealing at 130°C, leaving an atomically clean $Bi_2Te_3(0001)$ surface. On the other side, gold monocrystals were prepared by repeated sputtering with Ar^+ ions (typically 0.8 keV, 15 minutes) and subsequent annealing (500°C, 8 minutes), until the Au(111) surface showed atomically clean terraces with sizes of at least 10 nm, and visible herringbone reconstruction.

molecule	T (°C)
CoTBrPP	415
CoTPP	360
CoPc	410

Table 2.1: Typical temperatures at which evaporator cells were heated in order to sublimate each molecular specie.

Regarding the MO compounds, Cobalt - Phthalocyanine (CoPc) were acquired commercially from Sgima-Aldrich, Inc. Darmstadt (Germany), meanwhile Cobalt - Tetraphenyl Porphyrin (CoTPP) and Cobalt - Tetrakis (4-Promophenyl) Porphyrin (CoTBrPP) were synthesized in-house by and I. Imaz and H. Xu from

the team of D. Maspoch. Molecules were evaporated from an Organic Molecular Beam Epitaxy (OMBE) evaporator, equipped with alumina cells that were resistively heated at the temperature given in Table 2.1, above the sublimation temperature of each molecule. Both Au and Bi_2Te_3 substrates were placed within the molecular beams, enabling molecules to stick on their surfaces. TI and Au surfaces were kept at 77 K and room temperature (RT) respectively during the evaporations, and immediately transferred to the corresponding measuring chamber.

Chapter 3

MBE Growth of Chalcogen-Based Topological Insulator Thin Films

The capability of growing Topological Insulator (TI) materials with the Fermi level located within the bulk gap is essential to exploit the novel physical phenomena emerging from the spin-momentum locking of their surface carriers. Topological Surface State (TSS) are very sensitive to doping induced by structural defects [59, 127–129], bulk impurities [130–132] or molecular species adsorbed on the surface [133, 134], which generally induce n-doping and hence shift the the Fermi Level (E_F) above the minimum of the bulk conduction band. As a consequence, electronic conduction is not limited to the surface, and bulk carriers can bury the contribution from surface carriers. Indeed, it has become one of the major issues for the detection of the helical surface currents, and great efforts have been devoted to the growth of truly bulk insulating TIs, a task that has proved to be very challenging.

Chalcogenide-based TIs with van der Waals (vdW) stacked structure are typically synthesized by solvothermal techniques, like the self-flux method [23, 55, 135, 136], or by sonothermal techniques. So far TI crystals prepared by these two methods have been found to be strongly n-doped [53–55], bringing the E_F inside the bulk conduction band. This activates bulk conductivity that bury the detection novel physical properties emerging from the TSS. Molecular Beam Epitaxy (MBE) can to overcome this hindranc, as the precise control over the impurities level and crystal quality (under Ultra High Vacuum (UHV) environment) has allowed the growth of TI thin films with the E_F within the bulk gap [56–60]. The versatility of this technique also allows the introduction of extrinsic impurities with atomic precision [137–142] and the growth of hybrid TI hetero-

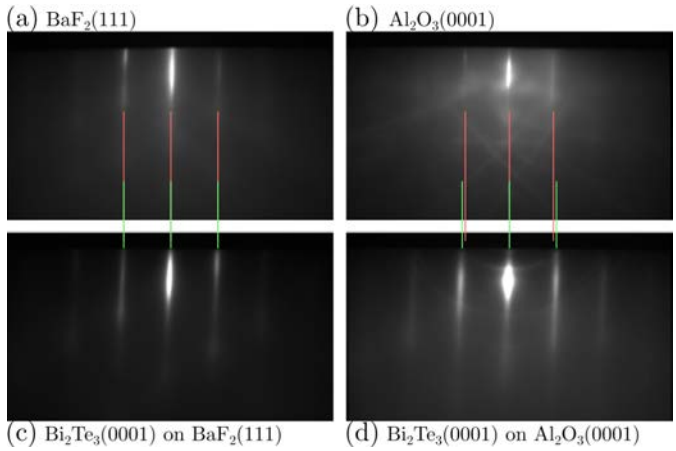

Figure 3.1: RHEED patterns corresponding to (a) $BaF_2(111)$, (b) $Al_2O_3(0001)$, (c) Bi_2Te_3 thin film grown on BaF_2 and (d) on Al_2O_3. Higher crystal quality is achieved in (c). Red and green vertical lines evidence the almost perfect match of $Bi_2Te_3(0001)$ with $BaF_2(111)$, and the misfit with $Al_2O_3(0001)$.

structures with controlled thickness [59], which emerge as suitable systems to exploit interfacial effects with other materials.

In this chapter, we report the growth of chalcogen-based thin films, and discuss the impact of the substrate choice and growth parameters to the growth mode and final result. Ex-situ characterization tools force us to use a Te layer in order to protect the TI surface while transferring the samples in atmospheric conditions. We show how it does not affect negatively their morphology, stoichiometry and surface state. Thereafter, we present two distinct routes for the MBE growth of TIs, in which control over both structural and chemical properties allow the experimental realization of TIs with precise positioning of the E_F.

3.1 Growth of Bi_2Te_3

3.1.1 Substrate Choice

The choice of a large gap insulator (11 eV, [143]) Barium Fluoride (BaF_2) as substrate for the growth of Bismuth Telluride (Bi_2Te_3) was motivated by the almost perfect matching between their (111) and (0001) facets respectively; $BaF_2(111)$ presents hexagonal symmetry and has a lattice parameter of 4.34 Å, leading to a misfit of 0.9 %. This is confirmed by the Reflection High-Energy Electron Diffraction (RHEED) diffraction patterns in Figures 3.1a and 3.1c corresponding to the clean $BaF_2(111)$ and $Bi_2Te_3(0001)$. More importantly, the long, sharp, unmodulated and intense diffraction rods in Figure 3.1 reveals that the growth results in a Bi_2Te_3 monocrytalline film.

In other to assess the influence of the substrate, a series of Bi_2Te_3 films were grown on the highly mismatched (9.4% misfit) $Al_2O_3(0001)$ substrate (7.5 ± 2.3 %). It resulted in polycrystalline films, as revealed by the concentric rings observed in the RHEED pattern in Figure 3.1d, indicating the presence of out-of-plane rotated domains. Moreover, broader diffraction rods and more intense background

Bi	Effusion cell T(°C)	570
	Cracker cell T(°C)	1100
	Flux (Å/min)	1.5
Te	Effusion cell T(°C)	280
	Cracker cell T(°C)	600
	Flux (Å/min)	3.0
Substrate T(°C)		300-500

Table 3.1: MBE parameters used for the growth of Bi_2Te_3 thin films on BaF_2. Fluxes are orientative, as for a fixed cell temperature they are sensitive to the geometry of the source material, and it changes every time that the cell is refilled.

than those of Bi_2Te_3 on BaF_2 indicate lower crystal quality. Changing the Al_2O_3 substrate temperature and Bi and Te fluxes resulted in polycrystalline samples, meanwhile the growth on BaF_2 resulted to produce monocrystals over a wider range of substrate temperatures. Both BaF_2 and Al_2O_3 substrates were prepared by pre-annealing at 800°C during 2h prior to the growth.

Because of the increased crystal quality and higher reproducibility, all MBE TI thin films studied in this thesis were grown on BaF_2.

3.1.2 Growth Conditions

Bi_2Te_3 thin films were grown on $BaF_2(111)$ (Crystal GmbH) by coevaporation of elemental Bi and Te (6N purity), in the MBE setup presented in Section 2.1.3, with a base pressure of $2 \cdot 10^{-10}$ mbar. Growth parameters are summarized in Table 3.1, showing that the Te/Bi flux ratio was set to ~ 2, much lower than flux ratios of $10 - 20$ enerally used for setups without cracker cells [127, 144]. The reason for using higher flux ratios than the 1.5 stoichiometry is to avoid Te deficiency, as the sticking coefficient of atomic Te at the deposition temperature of the substrate is nearly 0. The introduction of Bi allows the formation of heavier Bi-Te compounds that do stick on the surface. The growth rate is therefore limited by the Bi flux. Fluxes were measured by a previously calibrated quartz crystal microbalance.

A series of Bi_2Te_3 samples were grown at different substrate temperature (T_G), covering the range from 300°C to 500°C. Figure 3.2 shows the morphology of the obtained films measured by Atomic Force Microscopy (AFM). Two common features in all images can be identified: First, the presence of the characteristic spiral islands in which chalcogenide TIs generally grow, but presenting smaller areas and more rounded edges than those generally reported [59, 130, 142, 145, 146]. Small islands can not be attributed only to the fact that the low surface energy of the insulating BaF_2 substrate promotes the 3D growth over 2D. Multiple kinetic processes occurring at the surface, like step diffusion, pinning or clustering may be influenced by the substrate morphology and can also play an important role. The difficulty of unravelling the origin of these features relies on the complexity of decoupling the effects of such entangled processes.

On the other hand, correlation between the increase of substrate tempera-

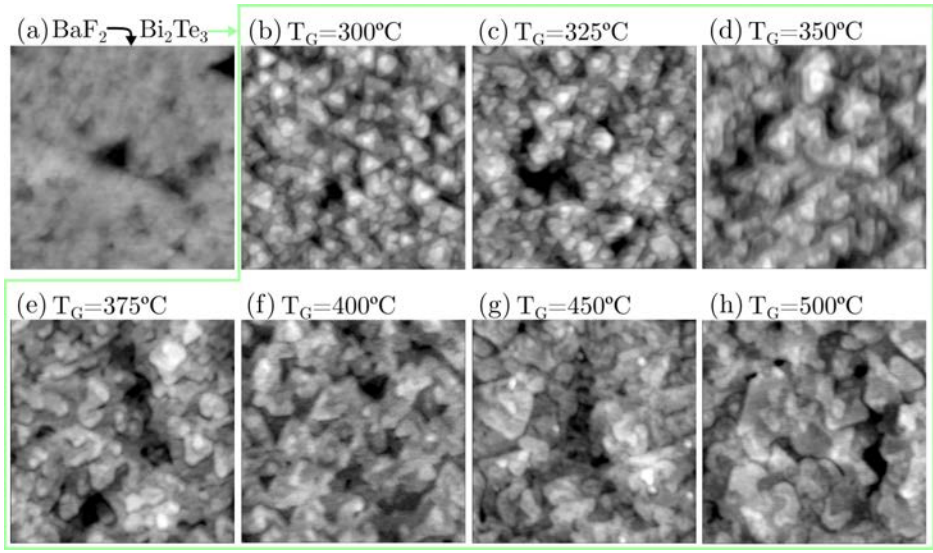

Figure 3.2: (a) AFM image of the $BaF_2(111)$ surface that would be subsequently used as substrate. (b)-(h) Comparison of AFM images corresponding to Bi_2Te_3 films grown on BaF_2 under the same Bi and Te fluxes but different substrate temperature (T_G). Image dimensions are 450×450 nm^2.

ture and islands area is clearly observed. This is consistent with the fact that higher temperatures enhance the particles mobility, promoting 2D over 3D growth modes. Higher particle mobility increases the step length, enhancing the probability of coalescence between islands and leading to larger terraces. This effect becomes evident at T_G =500°C, in Figure 3.2g. Furthermore, the orientation of the almost-triangular spiral islands is fixed for temperatures higher than 350°C. This is related with the suppression of one of the two mirror growth modes typical of MBE Bi-chalcogenide thin films. An extensive study of this effect is presented in Section 3.3.

AFM and X-ray diffraction experiments were performed on the as-grown films exposed to air. AFM images were recorded a few hours after the growth. X-ray diffraction and reflectivity measurements were performed on a PANalytical X'Pert Pro diffractometer operating with Cu K_α radiation.

After the growth, our Bi_2Te_3 thin films had to be exposed to air in order to be transferred from the MBE setup to ex-situ characterization setups. Therefore, and with the purpose of avoiding surface degradation, films were in-situ covered with a protective Te layer, the "capping layer". This would be later removed in the destination characterization setups.

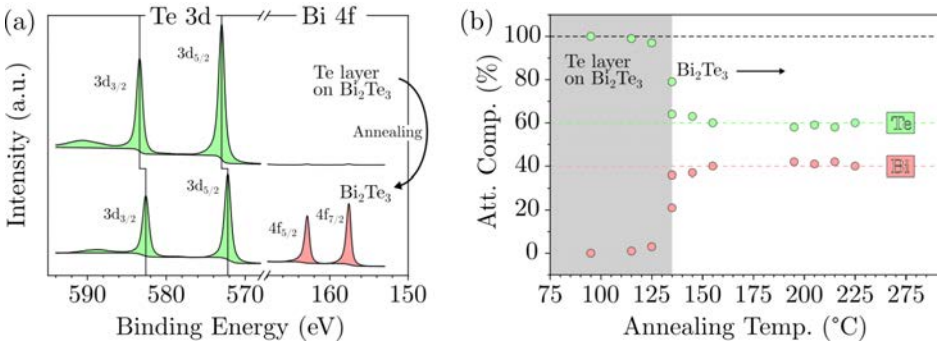

Figure 3.3: (a) XPS spectra centred at the binding energy of the Te 3d and Bi 4f doublet, measured on the Te layer on Bi_2Te_3 sample (top), and measured after thermal desorption of the Te layer (bottom). (b) Evolution of Bi and Te atomic concentration upon annealing temperature.

3.2 Te Capping and Decapping of Bi_2Te_3

The robustness of the TSS against non-magnetic dopants is well known, nevertheless, exposing their surface to ambient conditions induces water condensation that buries the non trivial-vacuum interface under a layer of trivial material. Molecules contained in air can also induce undesired doping effects. H. Benia et al. [133] studied the evolution of the surface electronic structure of Bismuth Selenide (Bi_2Se_3) as a function of water vapour exposure, finding that H_2O reacts inducing n-doping effect. Similarly, B. Zhou et al. [134] showed that the combined effect of H_2, CO and O_2 gases over Bi_2Se_3 and Bi_2Te_3 also produces electron-doping. For this reason, our samples were capped with a Te layer prior to be transferred to other ex-situ characterization UHV setups, a procedure that has been succesfuly used by other groups [142, 147, 148]. We found that transfer times ensuring no oxidation and no doping were limited to about 15 minutes.

The deposition of the capping layer was performed as follows: Once the growth of the Bi_2Te_3 film is stopped by shutting the Te and Bi cells, the substrate heater is turned off, leaving the sample cooling down to room temperature. When the temperature goes below 100°C, which in the geometry of our setup occurs after ~ 1 h, the Te shutter is opened again. Since the sticking coefficient of the surface can be considered to be 1 at this temperature range, the thickness of the deposited Te is the same as measured by the QCM balance. The Te deposition is stopped when the layer reaches a thickness of 20 nm. The sample was taken out from the MBE UHV setup, and transferred in air to the UHV setup of the pertinent characterization system Subsequently, the Te layer was removed by thermal annealing ("decapping" process).

3.2.1 Desorption Temperature and Chemical Properties

Cycles of 10 minutes of annealing were performed followed by X-ray Photoemission Spectroscopy (XPS) inspection of the Te 3d and Bi 4f peaks in order to

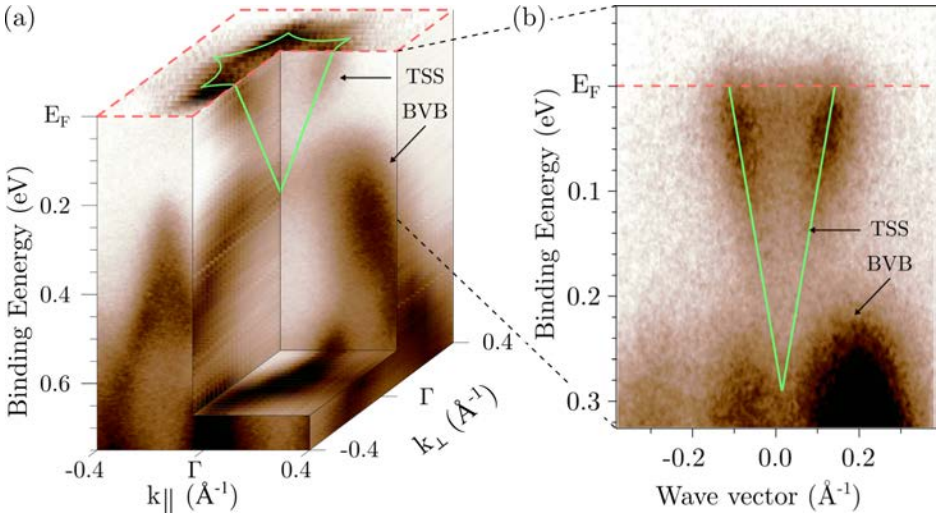

Figure 3.4: (a) Electronic band structure of Bi_2Te_3 measured by ARPES presents the TSS and the bulk valence band. (b) ARPES intensity map measured close to E_F shows the TSS in higher resolution.

determine the desorption temperature of the Te layer. Since XPS allows the inspection of the relative content of each element contained in a sample as well as its chemical environment, it arises as the most suitable characterization tool to assess the decaping process.

Figure 3.3a shows the three features that reveal the complete removal of the Te layer; First, an apparent energy shift ($\Delta E = 0.7$ eV) of the Te 3d doublet towards lower binding energies. The center of the $3d_{5/2}$ peak moves from 572.9 eV, attributed to elemental Te [149], to 572.2 eV, attributed to Te within the Bi_2Te_3 chemical environment [60]. Secondly, the emergence of the Bi 4f doublet. And thirdly, decrease of the Te 3d intensity, which combined with the intensity of the Bi 4f peaks gives rise to the expected 3 to 2 ratio of Te to Bi.

The evolution of the Bi and Te atomic concentrations obtained from the Te $3d_{5/2}$ and Bi $4f_{7/2}$ peaks with the temperature reached in each annealing are shown in Figure 3.3b evidencing that the desorption temperature of the Te layer is 130°C, and that the decaped Bi_2Te_3 crystal keeps its pristine 3/2 stoichiometry. Further annealing cycles ensure the chemical stability of the film up to 230°C, as the atomic composition is kept constant within the apparatus accuracy. Annealing to higher temperatures leads to film desorption.

3.2.2 Electronic Properties

The null contribution from the bulk conduction band observed in the Angle-Resolved Photoemission Spectroscopy (ARPES) maps of a Bi_2Te_3 thin film shown in Figure 3.4 reveals that the E_F is positioned well below the bulk conduction band, and ensures that the capped, transferred and decapped films still posses

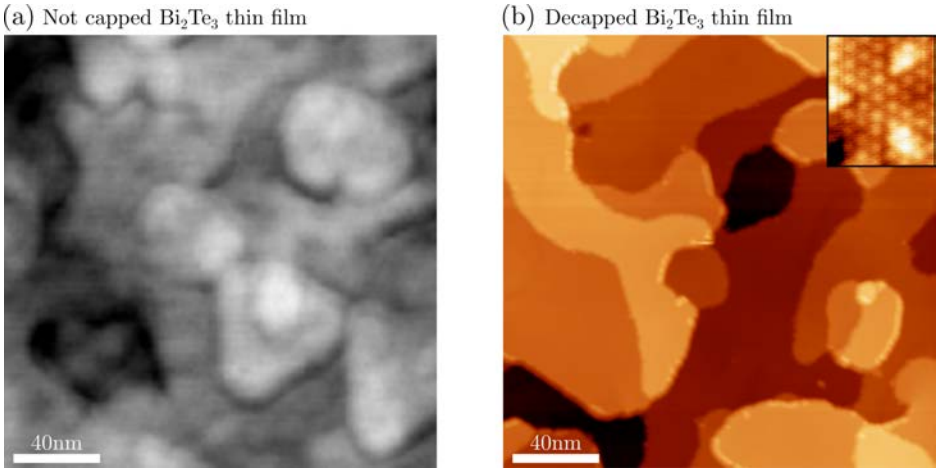

Figure 3.5: Morphology of two Bi_2Te_3 thin films grown in identical conditions. Film in AFM image (a) was taken out to from UHV conditions and subsequently measured. Film in STM image (b) was in-situ capped with the protective Te layer, transferred under atmospheric conditions to the STM UHV setup where a Te layer was thermally removed. Size and shape of the terraces are altered after the Te desorption processes. Inset: Atomically resolved Scanning Tunneling Microscopy (STM) image of a characteristic defect of Bi_2Te_3 surface, confirming the successful decapping ($V_{bias} = 0.4$ V, 2.2×2.7 nm^2).

bulk insulating behaviour. TSS dispersing as the characteristic 6-fold wrapped Dirac cone is also observed, together with intense features at higher binding energies attributed to the bulk valence band. Therefore, the main purpose of the Te layer of preserving the pristine surface state of the Bi_2Te_3 films is achieved, as it can be observed in the (k_x, k_y, E_B) space.

3.2.3 Surface Morphology

In order to assess whether the Te capping and decapping process induces alteration in the surface topography, two samples were grown under the same MBE conditions; one of them was taken to air to be measured by AFM, and the other was in-situ capped, transferred to the UHV setup of the STM, thermally decapped and finally measured. Manifest changes are visible in the comparison between their respective surfaces presented in Figure 3.5. The characteristic triangular shape of the islands seems to vanish, together with an enhancement of the terraces size.

The STM was not UHV connected to the XPS setup, meaning that a complementary method using the capabilities of STM had to be employed in order to assess the proper removal of the Te layer. For this purpose, a series of measuring and annealing at incrementing temperatures were performed. Above 130°C, the following features emerged and were used as fingerprint of the successful decapping. Atomically resolved images of the surface reveal an hexagonal lattice (with $a = 4.4$ Å), as well as different atomic defects characteristic of Bi_2Te_3 crystals.

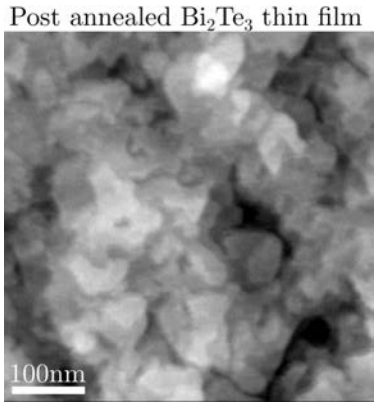

Figure 3.6: AFM image of a Bi_2Te_3 film in-situ post annealed during 1h at 400°C, under Te flux in order to avoid the creation of Te vacancies. The film was not capped.

As an example, inset in Figure 3.5b shows a defect attributed to a Bi_{Te} antisite allocated in the fifth atomic row [150]. Moreover, terraces morphology and field emission resonance spectra changed drastically but then remained unaltered up to the maximum annealing temperature reached (250°C), suggesting that the Te layer had been completely removed.

For comparison, a Bi_2Te_3 thin film grown under the optimized conditions was annealed at 400°C during 1 h after the Bi and Te fluxes were stopped, and measured afterwards by AFM without prior capping. Figure 3.6 shows that this process erases the characteristic triangular shape of the islands and increases the terrace sizes. We hypothesise that, analogous to the decapping annealing, the particle mobility in the surface is enhanced due to the increase of temperature, enabling islands to expand without any preferential direction, and flattening the overall topography. The resulting aspect of the surfaces are comparable for both post-annealed and capped-and-decapped samples, which indicates that surface reorganization is the responsible of the morphological changes occurring during the thermal removal of the Te layer.

Measured height (Å)	Height
4.1 ± 0.4	4.0 Å = 0.4 QL
6.5 ± 0.4	6.1 Å = 0.6 QL
10.7 ± 0.8	10.1 Å = 1 QL
14.2 ± 0.5	14.1 Å = 1.4 QL

Table 3.2: Aparent step heights measured by STM in several decapped Bi_2Te_3 surfaces, together with their correspondence with fractions of Quintuple-layer (QL), assuming the STM height of one QL reported in [128].

Besides the changes in the size and shape of terraces, steps height is also modified by the decapping process. Decapped Bi_2Te_3 surfaces exhibit steps corresponding not only to the expected quintuple layer (QL) height, but also to fractional-QL heights (see Table 3.2). These are reported in Table 3.2.

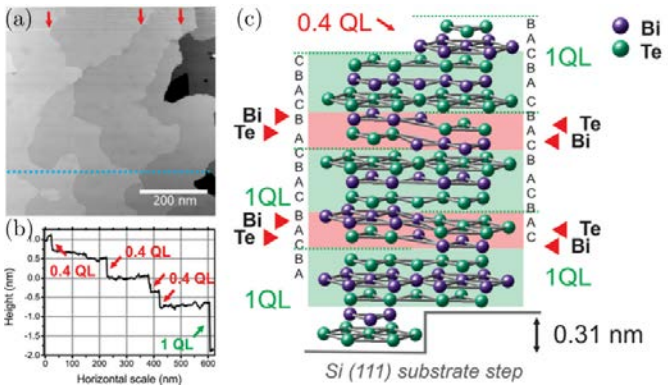

Figure 3.7: Figure directly reproduced from [151].

Even though it seems very unlikely that fractions of QL can be stabilized in Bi_2Te_3 crystals due to their strong intra-QL binding forces and weak vdW inter-QL forces, Borisova et al. [151] reported a model to explain the appearance of sub-QL steps. They measured step heights corresponding to 0.4 QL in Bi_2Te_3 grown by MBE on Si(111) and subsequently annealed, and proposed that these emerge as a consequence of a vertical translation between two adjacent domains. It was proved that this shift is induced by the 3.1 Å-high steps of the Si(111) substrate, and that this new stacking configuration can be stabilized by creating new bonds between non equivalent atomic planes of adjacent QLs, as it can be observed in Figure 3.7c.

Since atomic planes in the (111) direction of BaF_2 are separated by 3.58 Å, it is reasonable to assume that steps corresponding to 0.4 QL measured in our decapped Bi_2Te_3 films are also induced by the morphology of our substrate. Experimentally, steps of 4 Å have been measured in BaF_2 grown on Si(111) [152]. Values of steps reported in Table 3.2 have been measured in several STM images, and they can be appreciated in the illustrative STM image in Figures 3.8a and 3.8b. Line profile in Figure 3.8c shows the expected 1 QL steps and also the 0.4 QL steps, which can be explained as schematically illustrated in Figures 3.8e and 3.8f respectively. Line profile in Figure 3.8e reveals that some atomic terraces are not completely flat, suggesting that some QLs can still be piled up as they were in the spiral islands before the decapping. Therefore, 0.6 QL steps observed also in this line profile can be explained as $(1 - 0.4)$ QL $= 0.6$ QL (see the schematic in Figure 3.8h). Other steps corresponding to 1.4 and 1.6 QL were observed in other STM images not reported here, and they can be understood as single QL mounted on top of the upper QL forming steps of 0.4 and 0.6 respectively ($(0.4 + 1)$ QL $= 1.4$ QL and $(0.6 + 1)$ QL $= 1.6$ QL).

K. Schouteden et al. [153] also measured steps of 0.39, 0.63 and 1 QL, and demonstrated that these appear because of the annealing-induced formation of a Bi bilayer on Bi_2Te_3. Nevertheless, the following arguments discard this explanation to be valid in our case: (i) Te vacancies were claimed to appear above 375°C and emergence of the sub-QL steps was observed at 420°C, which contrasts with the lower decapping temperature (130°C) of our Bi_2Te_3 films. (ii)

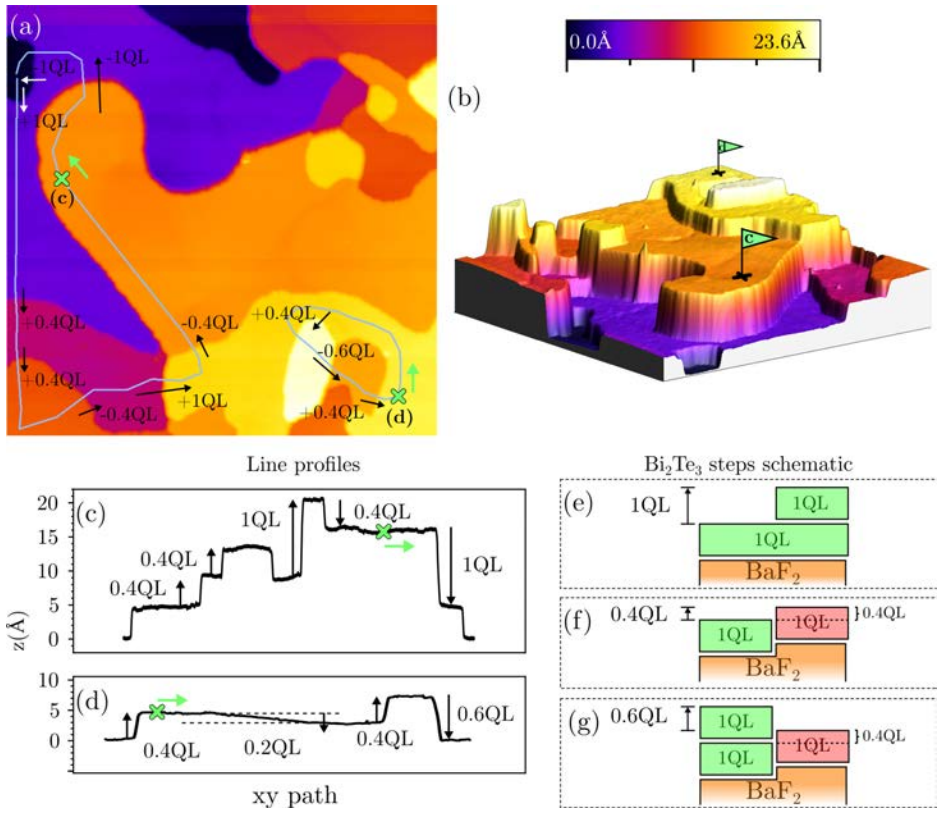

Figure 3.8: (a) STM image of a Bi_2Te_3 thin film after thermal desorption of the Te protective layer. (b) 3D projection of the same STM image, with an arbitrary z to $x = y$ ratio. (c)-(d) Line profiles taken along grey paths drawn in (a), showing steps corresponding to 1QL and to sub-QL. (e)-(g) Schematics of the steps configuration in terms of QLs.

The Density Functional Theory (DFT) calculations reported, indicate that the surface state dispersion would be substantially altered as a consequence of the Bi bilayer, which contradicts the pristine Bi_2Te_3 Dirac cone of our films measured by ARPES (Figure 3.4). (iii) Bi bilayer was reported to present a rough surface at the Å scale, which is in contrast with the sub-Å flat surfaces measured in our films. Additionally, we estimate (using the Beer-Lambert law) that the atomic concentration of Bi measured by XPS would increase from 40%, for the Bi_2Te_3 case, to at least 49.5 %, for the Bi-bilayer on Bi_2Te_3 case. Since this difference is larger than the sensitivity of our XPS apparatus, formation of Bi-bilayer should have been measured in our XPS experiments, and it is not the case.

Cross-section inspection of the decapped films by high resolution scanning transmission electron microscopy (HR-STEM) would be the definitive route to elucidate the piling geometry that give rise to the measured fractional-QL steps, as well as it would further confirm if their origin relies in the the surface morphology of the BaF_2 substrate.

3.2.4 Summary

XPS, ARPES and STM study of the decapped Bi_2Te_3 surface reveals that the thermal removal of the Te protective layer maintains the chemical properties of the film unaltered. However, it modifies the surface morphology by increasing the average terrace size and altering the QL stacking structure. Overall, this surface reorganization does not modify the electronic properties of the film, as ARPES intensity maps show that the TSS is preserved with the pristine level of doping (i.e. insulating bulk). Larger atomically flat surfaces are highly suitable for the long-range self-assembly of Metal-organic (MO) magnetic dopants that will be reported in Chapters 5 and 6, meanwhile the increased terrace areas and consequent reduction in the density of steps should pave the way for the TI surface carriers to have higher diffusion lengths.

3.3 Growth of Twin-free Bi_2Te_3

The capability to grow bicompound TIs with truly insulating behaviour by reducing the bulk impurities and crystalline defects is of great interest. Indeed, structural defects impact negatively the transport properties by coupling surface and bulk channels, by reducing the carrier mobility, or by suppressing the surface states in the case of strain localized at grain boundaries [154]. In particular, mirror-symmetric twin domains are of special importance owing to the extended planar nature of their boundaries, as shown in Figure 3.9. It has been demonstrated that twin boundaries hold a spontaneous polarization responsible for self-doping of the surface states, which may reach several hundreds of meV [155].

TIs usually grow on conventional substrates such as Al_2O_3(0001) [59, 127, 142] and Si(111) [57, 62, 127, 131, 144, 150, 151] despite lattice misfits close to 15 %. On such substrates, the growth generally proceeds by the formation of a polycrystalline or amorphous seed layer [142, 144, 156], followed by the growth of a (0001)-textured film in which 30° rotational domains and twins are inevitably present. Lattice-matched InP(111) (0.2 % misfit) was shown to ensure a much better crystallinity of Bi_2Se_3, characterized by reduced mosaicity twist and the suppression of 30° domains [142, 156]. On flat InP(111) substrates, a reduction of twinning was also observed, with the dominant twin occupying 66% of the total volume [157]. Further reduction down to full suppression of the minority twin was achieved by the use of rough substrates, at the expense of additional antiphase domains and, possibly, increased roughness of the films. Notably, twin suppression correlated with a reduction of the carrier density by almost one order of magnitude, demonstrating the relevance of structural improvement to achieve superior transport properties [157]. Suppression of twinning was also realized in Bi_2Te_3 grown at very low rate on Te-passivated Si(111), showing that improvement of the crystallinity can be achieved by controlling the growth kinetics [131]. In this case, single crystal epitaxy was likely promoted by the 7:8 incommensurate matching of the Si and Bi_2Te_3 lattices (1 % misfit). Nonetheless, no reduction in

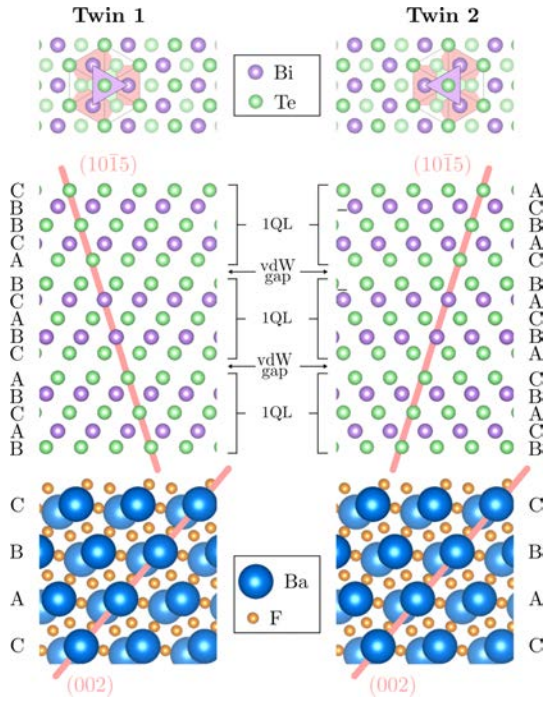

Figure 3.9: Schematic showing the atomic arrangement of the two twins occurring in (0001) Bi_2Te_3 ∥ (111) BaF_2 epitaxy. The twins differ by their ABCAB or ACBAC stacking, as apparent in both the Bi_2Te_3 (1$\bar{2}$10) side view and (0001) top view. The [10$\bar{1}$5] planes are highlighted in pink and their 3-fold symmetry is visible in the top view.

the carrier concentration could be observed: the films remained highly n-doped, which suggests that the incommensurate epitaxy was not able to suppress other kinds of structural imperfections. Lower doping was obtained by growing Bi_2Te_3 on lattice-matched BaF_2(111) (0.1 % misfit) [128, 147, 148, 158], but complete suppression of twinning has never been reported.

The data and discussions presented in this subsection are included in the work published by F. Bonell, M. G. Cuxart et al. [159], in which the study is also extended to Bi_2Se_3 and Antimony Telluride (Sb_2Te_3) thin films, and complemented with ab initio and kinematic deffraction theroy-based calculations. Figures have also been adapted from this publication.

3.3.1 Surface Morphology and Structural Properties

A series of Bi_2Te_3 thin films were grown at various temperatures T_G in the range of $300 - 500°C$, and they were in-situ characterized by RHEED and ex-situ by X-ray Diffraction (XRD) in order to quantify the density of twins. Figure 3.10 shows the results obtained for films grown at two representative T_G, together with an image of the surface measured by AFM. The position of diffraction rods in RHEED patterns is broadly characterized by a 6-fold symmetry, which reflects the hexagonal symmetry of the outermost atomic layer, independently of the stacking order of the rest of atomic layers within the QL. However, because of their finite penetration depth, electrons can be transmitted through islands of

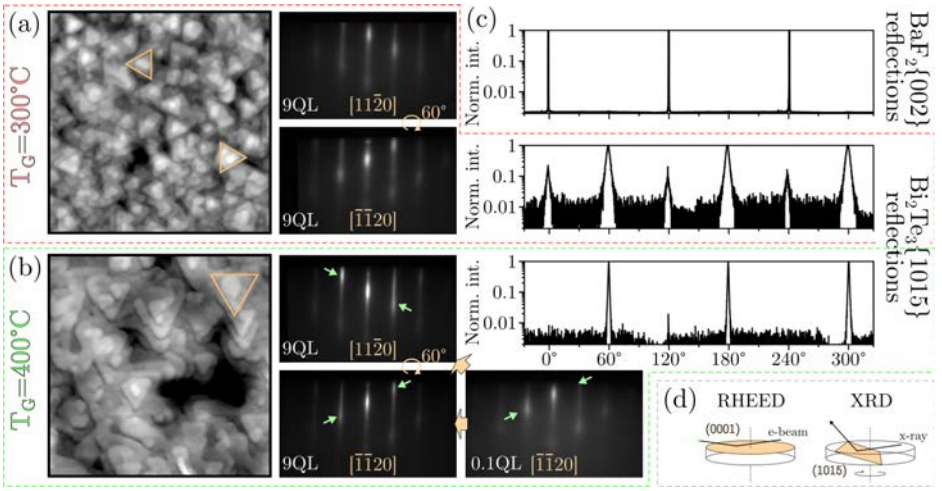

Figure 3.10: Two films grown at two representative temperatures (a) 300°C and (b) 400°C measured by AFM, RHEED and XRD pole scan. Film in (a) presents two groups of triangular islands rotated by 60°, consistent with its corresponding 6-fold symmetric XRD pattern, and Meanwhile only one twin is observed in the AFM image of (b), consistent with its corresponding 3-fold symmetric XRD pattern. RHEED patterns in (b) present clear opposite intensity modulation upon 60° rotation (from the very first stages of growth), and much sharper rods than in (a). (c) XRD pole scan of the BaF_2 substrate. (d) Geometry schematic of RHEED and XRD used to measure the Bi_2Te_3 films.

few tens of nanometers and are able to trace twins that differ by their ABCAB or ACBAC stacking (see Figure 3.9). As a result, the intensity along the rods is modulated, with maxima corresponding to 3D Bragg conditions and reflecting the trigonal symmetry of the crystal. The modulation is visible in all our RHEED measurements and is highlighted with arrows in Figures 3.10a and 3.10b. In the case of films grown at > 350°C, it is clear that RHEED shows the absence of 30° rotational domains, which would result in mixed [1$\bar{1}$00] and [11$\bar{2}$0] patterns. Diffraction patterns are invariant under a 120° rotation whereas a 60° rotation results in mirror-symmetric image, leading to the conclusion that one twin is dominant.

Remarkably, the RHEED patterns of ultrathin films of just 0.5 QL display the characteristic diagonal modulation of a "twin-free" crystal Figures 3.10a and 3.10b, which shows that the $BaF_2(111)$ surface forces the nucleation of islands with a definite stacking. This also demonstrates excellent epiitaxy since the very first stages of the growth and a $BaF_2(111)$ / Bi_2Te_3 interface of high quality, which is in clear contrast with the $1-2$ QL-thick amorphous or partly disordered seed layers observed on $Al_2O_3(0001)$, Si(111) and even InP(111) [142, 156, 157].

In order to quantify the degree of twinning, we measured pole scans of the [10$\bar{1}$5] reflections by XRD. Twin-free films should give rise 3-fold symmetric scans, while films containing twins in equal proportion are expected to show a perfect 6-fold symmetry, with equal intensity peak triplets at 60, 180 and 300°, and at 0, 120 and 240°. For both films grown at two different T_G, we observe that the

intensity at the 60, 180 and 300° is always stronger than at 0, 120 and 240°, indicating that one twin is dominant (Figure 3.10). The most intense reflections occur systematically at 60° of the {002} BaF_2 reflections, revealing that the ABC stacking of the BaF_2(111) substrate tends to be conserved in the grown Bi_2Te_3 and confirming that the dominant twin is determined by interaction with the substrate. Additionally, the suppression of twins correlates with a decrease of the peaks linewidth, which denotes a sharp reduction of the mosaïcity twist.

We observe spiral-like growth and steps with 1 QL height in AFM images. Bi_2Te_3 presents characteristic triangular islands in which chalcogenide-based TIs grow [127, 128, 130, 144–146, 156, 157, 160], denoting an anisotropic growth rate of the different island edges. At temperatures below 350°C, the triangular islands can be oriented in two opposite directions, depending on the twin orientation [142, 157, 161]. In contrast, the twinning is partially suppressed in films grown at > 350°C. This is illustrated by two films grown at 300°C and 400°C in Figure 3.10. The size of islands increases and even merge for sufficient high T_G, which means that the diffusion length of the adatoms is of the order of the terrace width.

Correlation between the spiralling island sizes and twin domains show that higher temperatures promote the diffusion of surface species and lead to extended islands. Following initial nucleation, the enhanced diffusion promotes spiral-like growth, without noticeable nucleation, as we do not observe RHEED oscillations. Incoming species stick to the terrace edges, ensuring the conservation of the stacking order and the absence of twin domains.

3.3.2 Physical Origin of Twin Suppression

Figure 3.11 compares the AFM images and pole scans of two films grown at 350°C onto epi-ready and cleaved BaF_2, respectively. The very (111) surface plane of BaF_2 has hexagonal symmetry and should, in principle, lead to the formation of both twins with equal probability. To induce single-twin growth, 3D information from the substrate must be transferred to the epilayer, either through the contribution of the subsurface plane to the adsorption potential [131] or by interaction with the atomic steps present on the substrate [156]. The surface of epi-ready substrates systematically shows a high density of nm-deep pits stemming from the chemo-mechanical polishing process, which are readily observable in the topography of the films (Figure 3.11c). In contrast, the surface of a cleaved BaF_2(111) is atomically flat over tens of micrometers, while no pits are found (Figure 3.11g). In spite of this, the surface condition of the substrate has a negligible influence on the islands density. Moreover, the growth on cleaved substrates results in further improvement of the film crystallinity, as inferred from the much sharper diffraction peaks and the full suppression of twinning at moderate growth temperature (Figures 3.11b and 3.11f). This implies that, instead of promoting single-twin growth, as reported for growth in InP(111) [156], the surface roughness in BaF_2(111) tends to pin disoriented domains, while the atomically flat substrate extends the optimal T_G window to lower temperatures.

Note that in the RHEED pattern corresponding to the epi-ready substrate

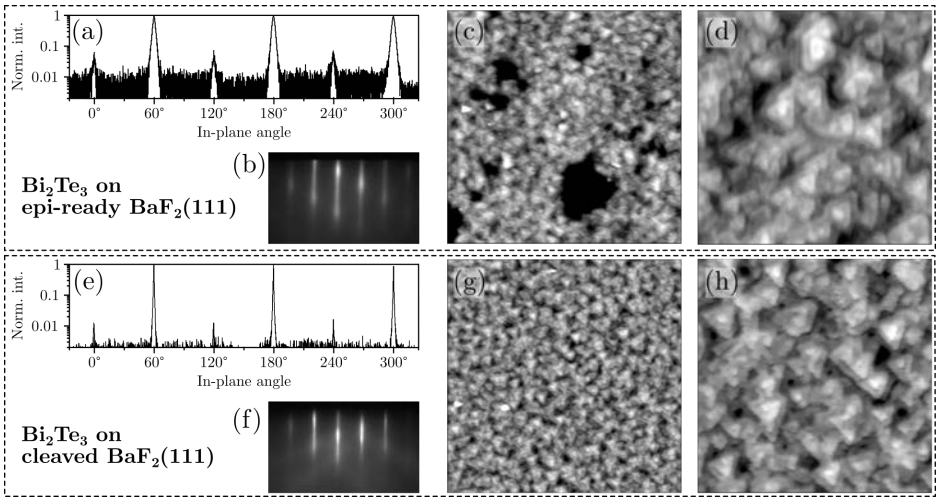

Figure 3.11: (a)-(e) $\{101\bar{5}\}$ XRD pole scans and (b)-(f) $[11\bar{2}0]$ RHEED patterns of 9 QL-thick Bi_2Te_3 thin films deposited at 350°C on chemo-mechanically polished (epi-ready) $BaF_2(111)$ and on cleaved $BaF_2(111)$. (c)-(d) and (g)-(h) AFM images associated with XRD scans (a) and (e) respectively. Image dimensions are: (c)-(g) 1800×1800 nm^2 and (d)-(h) 450×450 nm^2. Epi-ready substrates display nanometer-deep pits due to the polishing process.

(Figures 3.11h and 3.11), the diagonal modulation characteristic of single-twin surface is not clearly observed due to de convolution with Kikuchi lines. Nevertheless, the bulk sensitive XRD scans show unambiguously the 3-fold symmetry of twin-free thin films.

The direct interaction between BaF_2 and Bi_2Te_3 therefore promotes single-twin growth. In order to further support this conclusion, we performed DFT calculations of $BaF_2(111)$ on Bi_2Te_3 (1 QL) slabs with the two possible stacking orders (reported in the supporting information of our published work [159]). The energy difference between the two configurations amounts to 5 meV/cell (2 mJ/m^2) in favour of the experimentally observed dominant twin. Whether such a small difference can eventually account for the complete suppression is not clear, but it definitely favours one stacking configuration. In addition, the calculations confirm the low chemical interaction between Bi_2Te_3 and $BaF_2(111)$, with a charge transfer of only 0.15 e$^-$/cell and a binding energy dominated by the vdW interaction (+392 meV/cell).

3.3.3 Electronic Properties

ARPES maps in Figure 3.15a of twin-free Bi_2Te_3 grown under the optimized conditions for twin suppression ($T_G = 380°$) demonstrate very low doping levels (Figure 3.12a), with the Fermi level lying in the bulk gap. In contrast, the Fermi level of Bi_2Te_3 grown at $T_G = 380°$ lies in the conduction band (Figure 3.12b), which demonstrates the large electron doping introduced by crystal defects such as mosaïcity, twinning and roughness.

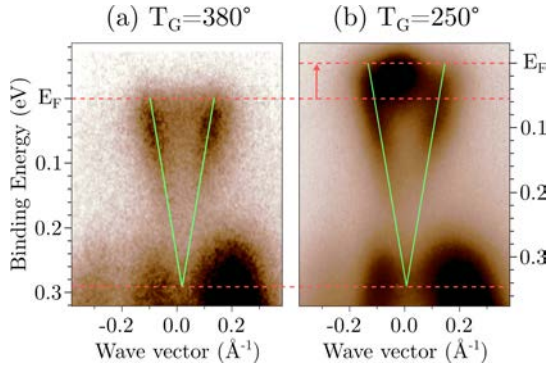

Figure 3.12: ARPES intensity maps showing how the Dirac cone of a Bi_2Te_3 film remains (a) undoped for T_G=380°C (single-twin) and (b) doped for T_G=250°C. Both measurements have been performed along the $\Gamma \rightarrow M$ direction.

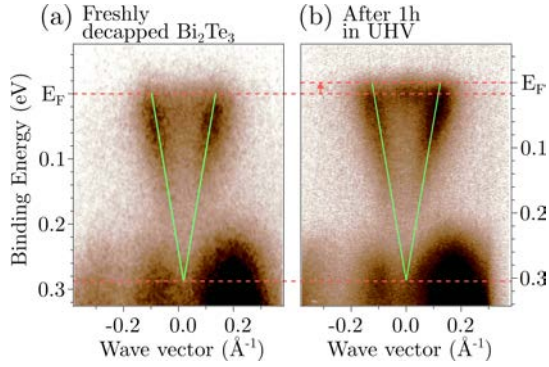

Figure 3.13: (a) ARPES intensity maps of a (single-twin) Bi_2Te_3 acquired after a few minutes after the decapping process and (b) after exposed to an atmosphere of $5 \cdot 10^{-10}$ mbar and to UV/X-ray during ~ 1 hour. It shows the aging n-doping tendency.

Nevertheless, the exposure of the freshly decapped films to UHV residual gases and UV/X-ray during about one hour turned out to n-dope a few hundreds of meV. This effect has been already reported to occur within minutes-time on Bi_2Te_3 and Bi_2Se_3 [56, 60, 134]. It is noteworthy to mention that all ARPES images that will be shown in Chapters 5 and 6 correspond to samples suffering from this aging effect.

3.3.4 Summary

Lattice-matched BaF_2(111) substrates enable the growth of high quality Bi_2Te_3 by MBE epitaxy, with an excellent BaF_2(111) / Bi_2Te_3 interface quality. The complete suppression of twins is achieved by a combination of the initial interaction with the substrate and the spiral-like growth mode favoured by high working temperatures. As a result, Bi_2Te_3 films are shown to be exceptionally low-doped, with their Fermi level well within the bulk band gap. Such low doping contrasts with measurements of twin-free Si(111) / Bi_2Te_3, in which the Fermi level lies in the conduction band [131]. This shows that the growth on lattice-matched BaF_2(111) results in a general structural improvement, preventing the formation of defects that cannot be suppressed by the incommensurate epitaxy on Si(111).

3.4 Growth of $(Bi_{1-x}Sb_x)_2Te_3$ Ternary Compounds

The Bismuth-Antimony Telluride ($(Bi_{1-x}Sb_x)_2Te_3$) represents a suitable benchmark TI as gradual change of the atomic content from Bi to Sb results in a gradual p-dope effect, at the same time that the Dirac point progressively emerges from the bulk valence band [58, 162]. Alternatively to the growth of twin-free crystals reported so far, it represents a complementary approach for controlling the doping level of TIs. In this section, instead of addressing structural properties, chemical properties are modified by means of tuning the stoichiometric concentration.

3.4.1 Growth Conditions

A series of $(Bi_{1-x}Sb_x)_2Te_3$ covering the whole $x\epsilon(0,1)$ range were grown, and subsequently characterized chemically with XPS and electronically with ARPES. The experimental parameters used in the MBE growth of each sample are summarized in Table 3.3, and shows that the Te flux (ϕ_{Te}) was kept constant while Bi and Sb fluxes were changed in such a way that the ratio $\phi_{Te}/(\phi_{Bi}+\phi_{Sb})$ was kept constant and close to 2, that represents the same Te-rich condition used for the growth of Bi_2Te_3 ($\phi_{Te}/\phi_{Bi} \sim 2$, see subsection 3.1). Te 4d, Sb 4d and Bi 5d peaks for each sample with a given x concentration are presented in Figure 3.14, confirming the expected gradual decrease of Bi 5d consequently accompanied by the increase of Sb 4d.

$x \rightarrow$		**0.00**	**0.25**	**0.34**	**0.51**	**0.75**	**1.00**
Bi	Effusion cell T(°C)		550	530	500	420	-
	Cracker cell T(°C)	1100					-
	Flux ϕ (Å/min)	2.2	1.9	1.6	1.2	0.6	-
Sb	Effusion cell T(°C)	-	355	360	375	385	390
	Cracker cell T(°C)	-	850				
	Flux ϕ (Å/min)	-	0.5	0.7	1.1	1.6	1.9
Te	Effusion cell T(°C)		280	280	280	283	277
	Cracker cell T(°C)	600					
	Flux ϕ (Å/min)	3.8	3.6	3.8	4.5	4.5	3.5
Substrate T(°C)		380	400	400	400	400	400
$\phi_{Te}/(\phi_{Bi}+\phi_{Sb})$		1.7	1.5	1.7	2.0	2.0	2.2

Table 3.3: MBE parameters used for the growth of the ternary $(Bi_{1-x}Sb_x)_2Te_3$ thin films.

3.4.2 Electronic Properties

Figure 3.15 shows ARPES intensity maps corresponding to three $(Bi_{1-x}Sb_x)_2Te_3$ thin films with $x = 0$, 0.25 and 1, in which TSS with massless Dira-like dispersions (Dirac cone, in green) and bulk valence bands are the main features observed, evidencing the robustness of the surface state in the whole ternary range. They are illustrative x concentrations, as they show how the addition of Sb at the

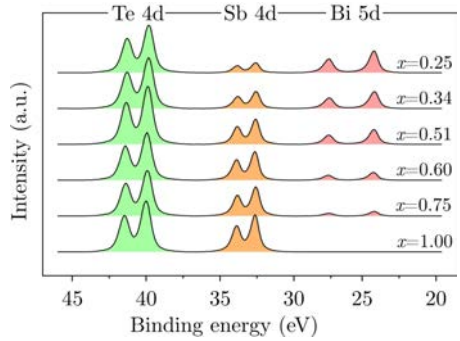

Figure 3.14: Single XPS region showing Te 4d, Sb 4d and Bi 5d peaks, measured on different $(Bi_{1-x}Sb_x)_2Te_3$ films with different Sb content (x).

expense of Bi shifts the Fermi level downwards, that is introduces p-doping, and how the Dirac point emerges from the bulk valence band and is positioned in the gap, as it is depicted in the schematic in Figure 3.15. J. Zhang et al. [58] showed, by ARPES and resistance vs. temperature measurements, that two separate regimes where the conduction governed by electron- or hole-like Dirac fermions emerge. They are separated by the charge neutrality point, that is when the E_F and Dirac point meet (between $x = 0.94$ and 0.96 in their case).

3.4.3 Summary

We were able to grow $(Bi_{1-x}Sb_x)_2Te_3$ over the whole x range by MBE and to track the electronic band structure by ARPES evolution. The addition of Sb at the expense of Bi gradually shifts the Dirac point to the bulk gap and, more importantly, induces p-doping to the crystal. Therefore, the adequate choice of x allows to position E_F well within the bulk gap or in the valence bulk band. This low doping level makes this ternary compound a very promising TI to preserve the bulk insulating behaviour after the eventual deposition of magnetic materials that tend to n-dope, and that are required for the study of spin-related phenomena. Nevertheless, Bi_2Te_3 thin films were used in the study of magnetic MO molecules on TIs reported in the following chapters. The deposition of such magnetic dopants on $(Bi_{1-x}Sb_x)_2Te_3$ with an appropriate x remains opened for future investigations.

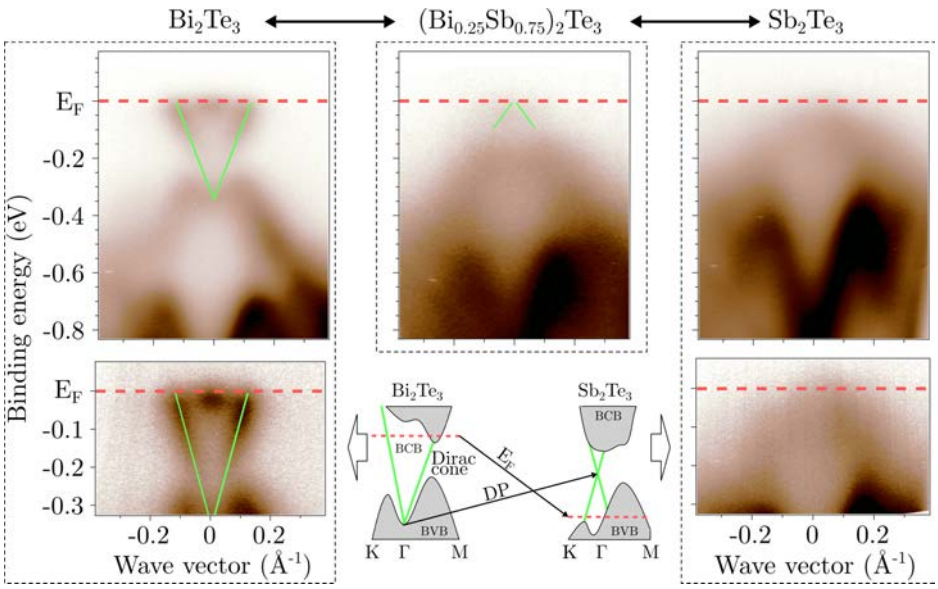

Figure 3.15: Top row: ARPES intensity maps of three $(Bi_{1-x}Sb_x)_2Te_3$ thin films with different concentrations x = showing a clear p-doping tendency upon introduction of Sb content. Bottom row: High resolution ARPES images of the Dirac cone and schematics depicting the evolution of the band structure with x (based on previous theoretical calculations [24] and ARPES experiments [58]). Maps have been acquired along the $\Gamma \rightarrow K$ direction.

Chapter 4

Fine Tunning of Magnetic Interactions on Surfaces via Ligand Chemistry

Magnetic properties of individual magnetic atoms on surfaces dramatically depend on the interaction with substrate states [163]. These can be effectively tuned by ligand chemistry [163, 164]. Organic ligands impose a well defined crystal field that splits the metal ion energy levels, defines the spin configuration and, together with a strong enough spin orbit coupling, introduces magnetocrystalline anisotropy (i.e. a preferred direction for the magnetic moment) [165]. On a surface, organic ligands tune the ion-surface distance, controlling the substrate contribution to the crystal field [165], the molecule-metal state hybridization [166, 167] or the charge transfer and Coulomb screening [67, 168]. This interaction leads to a spin reconfiguration that can affect the magnitude and magnetocrystalline anisotropy of the molecular magnetic moment, or even quench it [94, 166, 167, 169]. Thus the practical implementation of molecular spintronics depends critically on a profound understanding of molecule-substrate interactions, that can eventually enable higher control over the spin state of molecules [83].

One of the most sensitive probes for magnetic interactions in metallic surfaces is the Kondo effect [170]. This arises from the antiferromagnetic coupling between a localized spin of a magnetic impurity and those of the surrounding conduction of a non-magnetic metal. Below the characteristic Kondo Temperature (T_K), the spin-flip scattering processes related to the antiferromagnetic coupling leads to a screening of the magnetic impurity by the creation of a many-body singlet ground state. The strength of the Kondo interaction is then characterized by T_K, defined as the energy gained by the system through the formation of the Kondo singlet, and depends on the position (E_d) and width of the impurity energy level (Γ), and on the Coulomb repulsion (U) as described in the following expression [171]:

$$T_K = \frac{1}{2}(\Gamma U)^2 exp\left(\frac{\pi E_d(E_d+U)}{\Gamma U}\right) \tag{4.1}$$

where E_d, Γ and U are strongly affected by the molecule-substrate interaction.

Interestingly, the Kondo screening leads to a resonance at the Fermi Level (E_F) that can be readily detected by Scanning Tunneling Microscopy (STM) without the need of any spin-sensitive probe [170]. The width of the resonance is directly related to T_K as $2k_BT_K$, thus giving us direct access to probe the strength of the Kondo interaction. The Kondo feature should be accessible by Scanning Tunneling Spectroscopy (STS) if the system is measured at temperatures below T_K. However, interferences between the Kondo scattering and direct tunneling channels can perturb the shape of the resonance, giving rise to Fano-like asymmetric resonances [172].

The sensitivity of T_K on the interaction between the magnetic ion and substrate electronic states have been studied in different ways, either modifiying the ligand chemistry and conformation [166, 173–176] or the adsorption site of the metal ion [177, 178], by inter-molecular interactions [90], choosing different metallic substrates [179], or even gradually lifting the magnetic molecule with the tip [168, 180].

While the Kondo zero bias resonance allows local investigation of magnetic impurities, X-ray Magnetic Circular Dichroism (XMCD) provides non-local but more versatile way to investigate magnetic properties. Complementary to the STS studies presented above, magnetic Metal-organic (MO) molecules on metallic surfaces have been widely explored by XMCD and X-ray Absorption Spectroscopy (XAS). Substrate choice [167, 169, 181–186], on-surface chemical modifications of the ligands [79, 96, 184, 187–189] or electronic doping [95, 182] have been found again to be key tunable parameters affecting the magnetic properties. Additionally, XMCD has allowed the study of magnetic properties beyond the value of spin and orbital momentum, such as the magnetic anisotropy [165], or the molecular magnetic coupling through ferromagnetic or antiferromagnetic substrates [93, 190–192].

In this line, MO phthalocyanines and porphyrines represent an excellent benchmark to probe and control magnetic properties [94, 164, 167, 193]. Both are planar molecules that can host a single Transition Metal (TM) ion coordinated by four nitrogen atoms in its center. The TM ion is coordinative unsaturated, thus presenting a local reactive site that opens unique possibilities to control the magnetic properties via the two remaining vertical coordination sites. The effect of a supporting surface can modify this scheme, charge can be transferred within the substrate and d orbitals of the TM centres altering charge and spin states, influencing the magnetization of both molecules and substrate [93, 96, 184, 186, 189, 194]. Hybridization between molecular and substrate states induces more entangled interactions altering drastically the TM ligand field, or even favouring magnetic exchange. Therefore, depending on the interaction regime, hybridization can lead to complete quenching of the magnetic moment, as observed for CoPc on Au(111) [166] and Au(110) [169], for CoTPP on

Ag(111) [182] and for CoOEP on Ag(110) [195], or to partial reducion, observed for FePc on Au(111) [167]. On the other hand, preserved magnetic moment after adsorption was reported for CuPc on Ag(100) [181].

The non-magnetic state found for CoPc on Au(111) surface was reported to appear as a result of strong mixing of molecular and substrate states. It brings the system in a mixed valence regime, where the d occupancy cannot be measured as an integer number of electrons due to the delocalization or fluctuation of charge between molecule and substrate. The same scenario was assumed to explain the subsequent studies on the CoPc on Au(110) and CoTPP on Ag(111) systems. At the opposite limit of interactions, in the case of FePc the orbital mixing contribution of Au states is considerably smaller, though it still affects the groundstate by reducing $S = 1$ to $S = 1/2$. This scenario is related that to an underscreened Kondo interaction. These examples illustrate how relevant is to address efficient strategies to control molecular-substrate interaction in order to optimize the electronic and magnetic properties of molecular systems.

In this chapter we show how the adequate choice of rationally designed molecular ligands allow a progressive control over the magnetic interactions between a hosted Co ion and a Au surface. The spin states and magnetic moments are comprehensively studied thanks to the complementary use of local electron tunneling spectroscopy (STS) and element sensitive magnetic XMCD techniques supported theoretically by Density Functional Theory (DFT) (the former in collaboration with R. Robles). We are able to continuously cover the range of magnetic Co ion-substrate interactions. In addition, by changing the Au surface for a Topological Insulator (TI) surface, we extend interactions to the weak limit in which the molecular spin is completely decoupled.

4.1 Co-based Organic Molecules Used in This Study

Figure 4.1 presents the MO molecular compounds used for the study presented in this chapter. They consist of aromatic phthalocyanine and porphyrin macrocycles. We make use of Cobalt - Phthalocyanine (CoPc), Cobalt - Tetrakis (4-Promophenyl) Porphyrin (CoTBrPP), CoTPP and covalently linked CoTPP (cov-CoTPP), in which a Co ion is 4-fold coordinated with the 4 neighbour nitrogen anions (see round insets in Figure 4.1), yielding a very similar Co crystal field. Nevertheless, the different peripheral ligand environments leads to a dissimilar geometry and chemical environment when relaxed in gas phase or physisorbed on surfaces (see side views in Figure 4.1); CoPc ligand remains completely planar, while CoTPP ligands suffer a folding of the planar macrocycle (i.e. saddle conformation [173, 196]). Overall, the use of these 4 ligands confers a gradual tunability of the stacking geometry while maintaining the same macrocycle core.

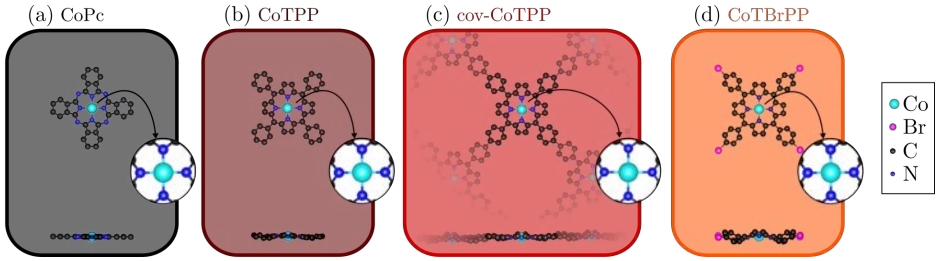

Figure 4.1: Top and side-view molecules used in this chapter: (a) CoPc, (b) CoTPP, (c) covalently linked CoTPP (cov-CoTPP) and (d) CoTBrPP. Round insets highlight the similar macrocycle core coordinating the Co ion of each molecule.

4.2 Molecular Self Assembly

The molecules were deposited on Au(111) and ("twin-free") Bismuth Telluride (Bi_2Te_3)(0001) surfaces by thermal evaporation in Ultra High Vacuum (UHV) conditions and subsequently measured by STM (see Chapter 3 for more details about the growth of the "twin-free" Bi_2Te_3 thin films). An independent experiment was performed for each system presented in Figure 4.2, where we can see that the different interaction of each molecule with the surface is already reflected in the self-assembly: CoPc interacts stronger than CoTPP and CoTBrPP. In the reconstructed surface of Au(111), the assembly of CoPc (Figure 4.2a) is guided by the surface interaction, they arrange in linear structures that follow the most favourable fcc tracks of the herringbone reconstruction. The assembly of 2D extended islands is inhibited even after post-annealing at 100°C, in agreement with previous results [197]. It is not the case of CoTPP or CoTBrPP (Figures 4.2b and 4.2d) on Au(111), where condensed molecular islands are formed at RT, in agreement to previous results [176, 198]. intra-molecular interactions dominate over substrate interactions and lead to the formation of 2D molecular lattices with 4-fold symmetric unit cell. Indeed molecular interactions are still dominating on more interacting substrates such as Ag(111) [91] or Cu(111) [199] surfaces.

Thermal annealing of the CoTBrPP networks on Au(111) leads to debromination and formation of C-C covalent bonds between phenyl rings of adjacent molecules. This kind of Ullman-assisted reaction has been widely used to construct covalent 2D nano-architectures since the pioneer work by L. Grill et al. was published in 2007 [82]. In our case, the resulting structures consists in islands of covalently linked CoTPP molecules (Figure 4.2c). The strong and directional C-C bonds forces the structures to have a 4-folded unit cell, regardless the surface symmetry.

Deposition of CoTBrPP onto Bi_2Te_3 substrate leads to a similar scenario as CoTPP and CoTBrPP on Au(111) as the molecular symmetry drives the self assembly regardless the 6-fold symmetric Bi_2Te_3(0001) surface (Figure 4.2e). Chapter 5 contains an exhaustive analysis of the stacking geometry of CoTBrPP on Bi_2Te_3.

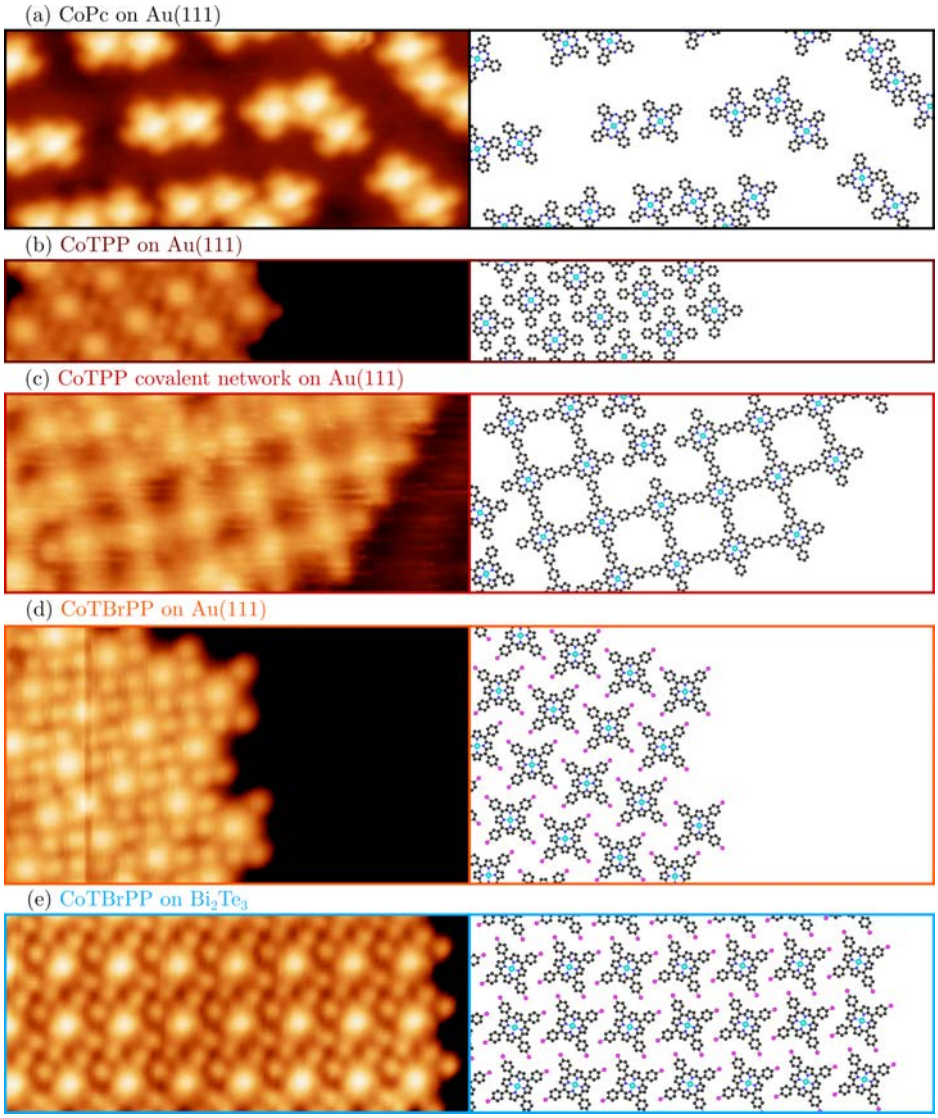

Figure 4.2: Left Panels: Constant current topographic images (lateral size: 11.0 nm). Right panels: Molecular models representing the molecular system of each image. (a) $V_{bias} = 0.50$ V, (b) $V_{bias} = 0.51$ V, (c) $V_{bias} = 0.60$ V, (d) $V_{bias} = 0.60$ V, (e) $V_{bias} = 0.51$ V. CoTBrPP and cov-CoTPP on Au(111) data courtesy of J. Huille.

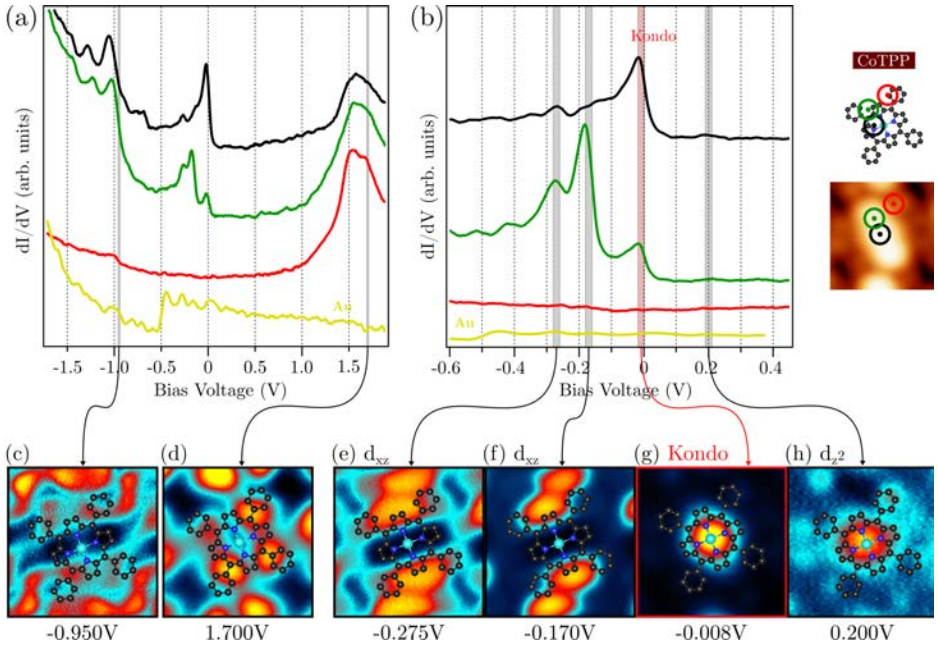

Figure 4.3: (a) Long and (b) short range dI/dV conductance spectra of CoTPP on Au(111) taken on the Co center (black), pyrrole (green), phenyl ring (red) and bare Au(111) (yellow) as a reference. (c)-(h) dI/dV conductance maps showing the spatial distribution of the spectral features highlighted in panes (a) and (b).

4.3 CoTPP Electronic Structure on Au(111)

A full set of STS measurements complemented by DFT calculations were performed in order to identify the CoTPP molecular orbitals on Au(111). The description of Co d levels subsequently reported for this system can be taken as model for the rest of the molecules used in this study, due to the similar crystal field experienced by the Co ions.

STS spectra were taken on three representative sites of the molecule, Co ion, pyrrole and phenyl rings (represented in black, green and red respectively in Figure 4.3a). The main features observed are; (i) a double peak at -0.8 to -1.0 eV with Co and pyrrole contribution, (ii) another double peak present at -0.1 to -0.3 also with pyrrole and Co contributions, (iii) a strong peak at E_F with basically only Co contribution and (iv) a broad peak at around 1.5 eV with strong phenyl contribution. The spatial localization of these peaks can be seen in the dI/dV maps taken at the mentioned energies; (i) show an incipient 4-fold symmetry with the charge located along the direction of two opposite phenyl rings, (ii) presents a 2-fold symmetric distribution of each peak of the doublet, both aligned along the same pair of opposite pyrroles , (iii) and (iv) exhibit spherical symmetry located on the Co ion.

In order to identify the orbital origin of each spectral feature, DFT calcula-

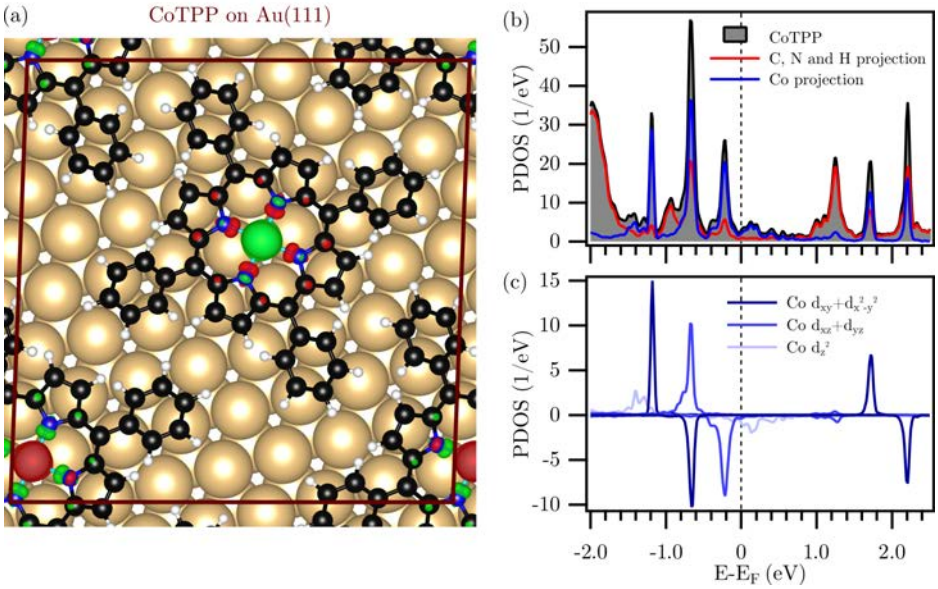

Figure 4.4: Calculated CoTPP adsorption geometry on Au(111) calculated by DFT. PDOS on (b) the different CoTPP elements and on (c) the different Co d orbitals. Calculations by R. Robles.

tions were performed in the same CoTPP on Au(111) system. From the DOS projected on the different Co and C orbitals (PDOS) shown in Figure 4.4, the experimental peaks can be assigned to molecular orbitals. The broad feature (iv) at 1.5 eV can be easily related to the first unoccupied pure ligand represented as a broad contribution around 1.3 eV (red curve in Figure 4.4b). Following the same reasoning, the peaks (i) at -0.8 to -1.0 eV can be assigned to a mixture of C and Co states. The latter consists of majority d_{z^2} and d_{xz}/d_{yz}, and both majority and minority d_{xy}. The double peak (ii) at -0.1 to -0.3 eV can be assigned to the minority d_{xz}/d_{yz}. Its peak and shoulder structure arises from the break of the degenerate d_{xz} and d_{yz} orbitals, induced by the out-of-plane distortion of the pyrroles (i.e. saddle conformation) and the consequent D_{4h} to C_{2v} symmetry reduction. The orbital closer to E_F extends along the upper pyrole pairs, labelled as d_{xz} here (we note that the identical alignment of the two lobes in the dI/dV maps of the d_{xz}/d_{yz} doublet in Figures 4.3e and 4.3f is related to the fact that the signal coming from the upper pyroles always dominates in constant height measurements due to their proximity to the tip).

In contrast to the above described features, the remaining sharp peak (iii) at E_F localized in the Co ion, cannot be explained by any Co d contribution in this energy range. From its spherical symmetry, one could tentatively relate it to the minority d_{z^2} orbital, which is located slightly above E_F in the calculations. However, its broad orbital spread over an energy range of ~ 1 eV (Figure 4.4c) as a consequence of the hybridization with Au states is in stark contrast with

its sharp experimental linewidth (black line in Figure 4.3b and dI/dV map in Figure 4.3h). An alternative natural origin of a sharp peak at E_F is the Kondo resonance, as has already been suggested for CoTPP on Au(111) in previous studies [176, 200]. The fact that its spatial distribution reproduces the d_{z^2}, the only spin carrying orbital, further supports the proposed Kondo scenario.

4.4 Kondo Screening

The presence of a resonance at E_F is common in the Co-based compounds studied, which allowed us to carry out a systematic study of the effect of the different ligands in the Kondo interaction strength. The spectra acquired at 5 K around E_F for all compounds is summarized in Figure 4.5. Slight differences can readily be observed in the linewidth, which can be directly related to the Kondo interaction strength, represented by T_K. In order to extract T_K for each system showing Kondo resonance, the peak can be fitted with a Fano function [201], which accounts for interferences between two tunneling channels, the Kondo resonance and conduction states of the substrate [170]. In this context, the conductance dI/dV is proportional to

$$\rho_0 + (q+\epsilon)^2/(1+\epsilon^2)$$

, where $\epsilon = (E - E_K)/\Gamma$ is a renormalized energy , with E_K as the peak position and Γ_K the half-width at half maximum of the Fano resonance, which is given by

$$2\Gamma_K = [(\alpha k_B T)^2 + 2(k_B T_K)^2]^{1/2}$$

. The lineshape is defined by the so called q form factor, which is determined by the ratio of the two interfering channels. Values of q close to 0 result in a dip and are originated by a dominating direct tunneling to conduction electrons. On the other hand, values $|q| > 1$ give a progressively more symmetric peak and indicate a dominating Kondo channel. For 5 K, the thermal broadening contribution is only of 1 K, < 1 % of the total linewidth, and hence we hereafter directly relate Γ_K to $k_B T_K$.

In line with previous works reported in literature [166], the STS spectra of CoPc in Figure 4.5 presents a broad feature that can be related to Co d states and no Kondo resonance. Both characteristics are related to a strong interaction with the Au substrate that results in a partial filling of the Co d_{z^2} and its hybridization with Au sp states, bringing the system to a mixed-valence regime [166, 167]. In contrast, the three porphyrin-based compounds on Au(111) studied show a Kondo resonance, together with the d features at around -0.1 to -0.3 eV discussed in detail before for the CoTPP on Au(111) case. The smaller Kondo resonance is found for CoTPP with a resultant $T_K = 209 \pm 2$ K (at $E_K = -1.0 \pm 0.3$ meV). CoTPP forming a covalent network (cov-CoTPP) shows a slightly smaller $T_K = 149 \pm 4$ K (at $E_K = 0.9 \pm 0.4$ meV), meanwhile the Br-functionalized Tetraphenyl Porphyrin (CoTBrPP) presents the weakest resonance $T_K = 132 \pm 3$ K (at $E_K = -1.0 \pm 0.3$ meV). The q factor varies from -2.8, -3.3 to -4.8 respectively. The larger $|q|$, as compared to the 0.5-0.6 obtained

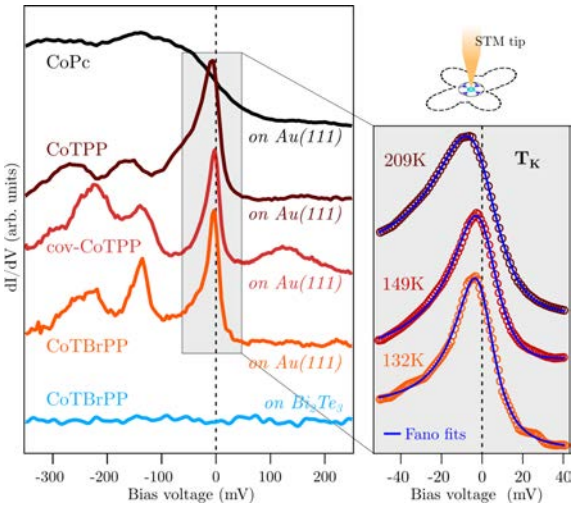

Figure 4.5: dI/dV spectra taken on the molecule centre of each different molecular systems. Inset: Fano-like function fits to the zero bias Kondo resonance peaks, and calculated T_K depicting the magnetic interaction strength of each case. CoTBrPP and cov-CoTPP on Au(111) data courtesy of J. Huille.

for bare Co on different metals [170] reflects a lower contribution of direct tunnelling to substrate conduction states, as expected for a more decoupled ion in the molecule.

Finally, by changing the substrate where CoTBrPP is deposited, from Au(111) to Bi_2Te_3,the spectra becomes flat around E_F (light blue curve in Figure 4.5). Separation of molecular orbitals away from E_F is a consequence of a higher intra-molecular Coulomb repulsion (U), enhanced because of weaker molecular-substrate interaction and of the reduced, two dimensional Density of States (DOS) of the TI around E_F. This reduction of the molecule-substrate interactions, when first deposited on Au(111) and later on Bi_2Te_3 surface has also been observed in one of the very few theoretical studies of organic compounds on TI surfaces [202]. An extended STS characterization and detailed discussion about the electronic structure of CoTBrPP molecules on Bi_2Te_3 is reported in Chapter 5.

According to the above arguments, the largest T_K found for CoTPP on Au(111) indicates that this is the TPP-based molecule with the strongest interaction with the substrate, whereas similar but weaker interactions can be attributed to the brominated CoTBrPP and covalently linked CoTPP. The weaker molecule-substrate interaction derived for CoTBrPP as compared to CoTPP correlates with a slighter larger Co-Au distance obtained by DFT calculations (Figure 4.7b and Table 4.1). We attribute the different interactions found for each molecular compound to conformational effects, either directly related to the presence of Br atoms in CoTBrPP or covalent inter-molecular bonds in cov-CoTPP, or indirectly by the influence of the saddle distortion on the porphyrin core. Indeed, a significant changes on the T_K upon conformational switching of CoTBrPP on Cu(111), from saddle to planar, has been observed for [173].

Table 4.1: DFT calculated adsorption distances and magnetic moments.

	d_{Co-Au} /Å	μ_{Co} /μ_B
CoTPP/Au(111)	3.25	0.88
CoTBrPP/Au(111)	3.27	0.87

	d_{Co-Te} /Å	μ_{Co} /μ_B
CoTBrPP/Bi_2Te_3	3.82	1.11

4.5 Kondo Screening

The local characterization performed by tunnelling spectroscopy has been complemented by non-local XAS/XMCD measurements, where the Kondo screening can be measured as a reduced XMCD signal. Spectra were acquired at the photon energy to excite an electron from the Co 2p level to the spin-carrying 3d level, that is at the Co $L_{2,3}$ edge energy range. Spectra were taken at normal and grazing incident angles to study the mangetocrystalline anisotropy. In all compounds, the XMCD signal was more pronounced for grazing angles as shown in detail in Chapter 5, revealing an easy plane anisotropy. Based on that, the spectra shown in this chapter correspond to those acquired at grazing incidence configuration ($\theta = 70°$), sensitive to the projection of the magnetic moments to the sample plane. Samples close to the molecular Mono-Layer (ML) saturation were measured for all compounds. The molecular coverage, self-assembled structure and homogeneity was checked by in-situ STM measurements thanks to the capability of coupling our variable temperature STM (Aarhus 150 - SPECS) to the BOREAS beamline in ALBA synchrotron.

The studied Pc- and TPP-based molecules show a Co L_2 edge in the XAS spectra composed of a narrow peak at 777 eV and a multiplet structure within 779 - 783 eV. The intensity ratio between the peak and the multiplet gradually increases as going from CoPc on Au(111) to CoTBrPP on TIs, that is from black to blue in Figure 4.6a, as well as the multiplet structure becomes progressively more defined. This is a consequence of the direct contact of the molecules with the Au(111) surface, which promotes the hybridization between Co d orbitals and conduction electrons thus broadening the spectral features of the molecules. This effect was previously highlighted by comparing the Co $L_{2,3}$ edge of CoPc single and multiple ML on Ag(100) [167], and of other complexes [195].

XMCD spectra in Figure 4.6b show a gradual recovering of the dichroic signal from the vanished situation for CoPc and CoTPP on Au(111), to a progressive increase for CoTBrPP and cov-TPP on Au(111), and finally for CoTBrPP on Bi_2Te_3.

The absence of XMCD magnetic signals in CoPc and CoTPP on Au(111) systems obeys to a completely different physical mechanism. In the case of CoPc, the magnetic moment is quenched as a consequence of the formation of strong hybridization of the spin-carrying d electrons with the substrate conduction electrons. This has been discussed extensively in [167], where the quenching of the Co

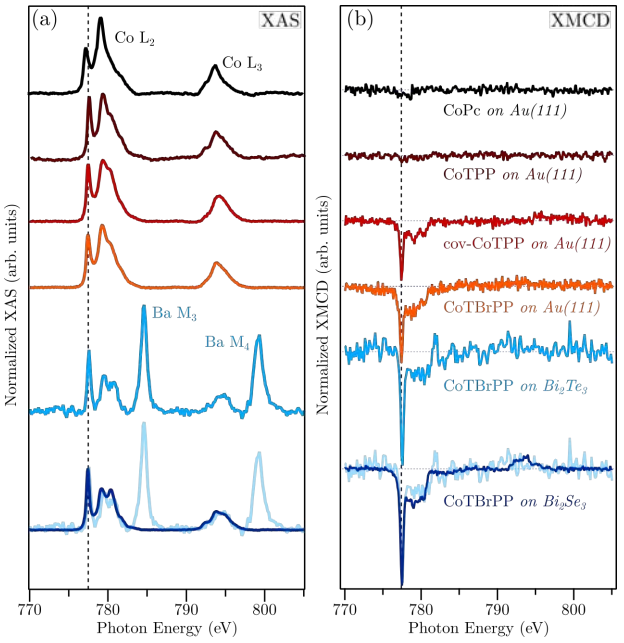

Figure 4.6: (a) XAS and (b) XMCD Co $L_{2,3}$ edge measured at grazing incidence angle ($\theta = 70$ °, in plane sensitive) at 7.5 K. CoPc on Au(111) data courtesy of S. Stepanow. Calculations by R. Robles.

magnetic moment was attributed to a renormalization of the ground state after charge electron transfer from the substrate, resulting in a dynamical mixed valence configuration consequence of strong hybridization with the substrate. The Co ion assumes a d^7 configuration while the substrate is modeled as a state with one electron. The surface electron can hop into the d_{z^2} Co orbital, leading to the mixed $d^7E+ d^8$ configuration (where E denotes the surface electron). This results in a lowered energy robust ground state with $S = 0$, as the first magnetic state (with $S = 1$ character) lies above 1.1 eV [181]. The same model was assumed to explain the absence of XMCD signal and the consequent quenching of magnetic moments of CoTPP on Ag(111) [182], and CoPc on Au(110) [169].

Even that CoTPP molecules on Au(111) do not show dichroic signal, its magnetic moment is not quenched as it is evidenced by the presence of a Kondo resonance (Figure 4.5) and the DFT calculations (Table 4.1). We propose that the vanishing of the dichroic signal results from an effective screening of the magnetic impurity by the surrounding conduction electrons driven by the strong Kondo interaction. The Kondo screened quenching of the dichroic signal has already been reported for Fe atoms on Cu(111) [203].

In the case of cov-CoTPP and CoTBrPP on Au(111), the gradual increase of dichroic signal correlates with the decrease of the strength of the Kondo interaction (T_K) and of the DFT calculated absorption distance (d_z), as evidenced in Figure 4.5. Although one would expect an effective Kondo screening of the magnetic moment at the measuring temperatures, finite XMCD signals have already been observed in dilute Fe:Cu alloys well below T_K [204].

Finally, the increased XMCD signal for CoTBrPP on Bi_2Te_3 is a fingerprint

Table 4.2: Summary of the spin ($\mu_{S_{eff}}$) and orbital (μ_L) moments extracted from the XMCD data. Calculations by R. Robles.

	$\mu_{S_{eff}}$ $/\mu_B$	μ_L $/\mu_B$
CoTPP / Au(111)	0.0 ± 0.01	0.0 ± 0.01
cov-CoTPP / Au(111)	0.26 ± 0.03	0.09 ± 0.03
CoTBrPP / Au(111)	0.37 ± 0.03	0.14 ± 0.02
CoTBrPP / Bi_2Se_3	0.60 ± 0.04	0.26 ± 0.02

of a well decoupled system, in line with the sharp multiplet lineshape measured by XAS [184, 186, 190]. Indeed, DFT calculated absorption distance and Co magnetic moment present higher values 3.82 Å and 1.11 μ_B as compared to the same molecule on Au(111) surface, as shown in Table 4.1.

In order to finely assess the degree of interaction between the molecular compounds and substrates, the Co effective spin ($\mu_{S_{eff}}$) and orbital magnetic (μ_L) moments were calculated by sum rules analysis (Table 4.2). The absolute values have to be taken carefully since they were calculated from a highly non-saturated situation, as revealed by the magnetization curves (not shown here), and assuming isotropic X-ray absorption. An additional error arises from the assumption of isotropic X-ray adsorption, where deviations from the generally assumed value of $I_0 = (I^+ + I^-)/2$ are substantial for anisotropic compounds such as our planar molecules [167]. Despite these approximations, the increasing orbital and spin moment can be clearly correlated with the continuous decoupling tracked by the Kondo STS analysis.

Note that in this part of the study we have introduced data corresponding to CoTBrPP on Bi_2Se_3 exfoliated crystal, a chalcogen-based TI owing the same layered van der Waals (vdW) structure as Bi_2Te_3. The reason is that the sum rule analysis results in large uncertainties when applied to the thin film Bi_2Te_3 sample due to the presence of the Ba $M_{3,4}$ edge (at 784 and 799 eV) within the same range used of the Co $L_{2,3}$, arising from the BaF_2 substrate (refer to Chapter 2 for more details about the growth of the Bi_2Te_3 thin films). Therefore, the quantitative analysis of orbital and spin moments has been carried out in Bi_2Se_3, relying that the molecule is similarly decoupled in both systems, as indicated by DFT results (not shown).

The Co L_3 XMCD intensity for three molecular systems is plotted together with T_K and the surface distance d_z respectively in Figures 4.7a and 4.7b. The decrease of the magnetic dichroic signals correlates with the increase of Kondo interaction and with the decrease of absorption height. These tendencies evidence the crucial role of the molecular conformation induced by the modifications on the CoTPP phenyl groups in the magnetic interactions between molecules and substrates.

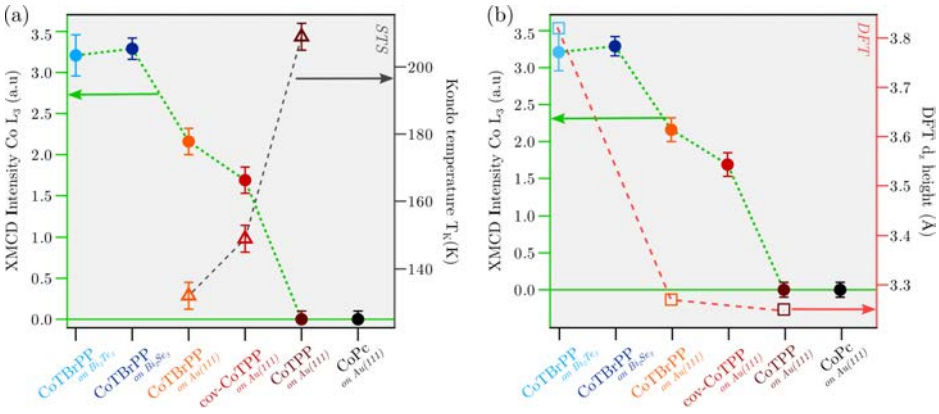

Figure 4.7: Correlations between the magnetic dichroic signal (XMCD intensity) measured for each molecular system and the (a) strength of the Kondo resonance (T_K) and (b) the adsorption distance (d_z). Calculations by R. Robles.

4.6 Summary

By using different organic ligands to host a Co ion in the same 4-fold N coordination, we are able to tune magnetic interactions with the substrate across the whole interaction range from the mixed valence regime in strongly interacting systems, to the Kondo regime with progressively decreasing T_K, and finally to the non-interacting regime.

For CoPc, we find strongly hybridized d levels combined with the absence of Kondo and dicrhoic signatures, both characteristic of strongly interacting mixed valence regime.

The interaction between CoTPP and Au is weaker, as indicated by the sharper Co d-related electronic states, and the broad Kondo resonance of $T_K = 209$ K. The Kondo interaction in this molecule is strong enough to screen the total magnetic moment at the (XMCD) measuring temperature. On the other hand, CoTBrPP and cov-CoTPP exhibit Kondo resonances of smaller Kondo Temperature ($T_K = 149$ K and 132 K respectively) as compared to CoTPP, indicating a sizeable decoupling of the Co ion by the different ligand conformation. The reduction of the Kondo interaction correlates with the gradual increase of the projection of the magnetic moment measured by XMCD.

Finally, the considerably larger magnetic moment, closer to the nominal Bohr magneton of a $S = 1/2$ system and the absence of a Kondo resonance for CoTBrPP on TI substrates, indicate an effective decoupling of the Co magnetic moment that leads to the recovery of the value of the pristine molecule. These results demonstrate that ligand chemistry can be employed for tuning magnetic interactions across the whole interaction regime in a progressive manner. The results on Bi_2Te_3 further illustrates that unperturbed magnetic / TI interfaces can be realized by controlling interactions by ligand chemistry. This scenario encourages the deeper study presented in Chapter 5 on the stability of the Topological Surface

State, in views of the realization of an interface were both agents preserve their pristine features, key aspect in the realization of the novel magnetoelectronic phenomena emerging from TIs.

Chapter 5

Metal-organic Topological Insulator Heterostructures: vdW Phase

Interfacing Topological Insulators (TIs) with magnetic materials can give rise to interesting phenomena involving the manipulation of spins with charge currents and viceversa. The spin polarization generated by helical currents at the surface of a TI via Edelstein Effect can switch the magnetization of a ferromagnetic ovelayer by the efficicent transfer of spin-orbit torques [205, 206]. Conversely, spin currents injected from the ferromagnetic layer to the TI can be converted into helical charge currents (Inverse Edelstein Effect) [43]. More entangled magnetic interactions at the topological boundary can also lead to the QAHE, where an out-of plane long-range magnetic ordering turns helical surface states insulating and give rise to metallic, spin polarized edge states [45, 207, 208].

In order to realize all the above phenomena in magnetic / TI heterostructures, one needs to control how the magnetic moments, anisotropy and long-range order of the magnetic layer, as well as the spin texture, the Fermi Level (E_F) and band dispersion of helical states are affected by the interfacial interaction. Ideally, a rational design of heterostructures would require non-perturbative interactions where the properties of the magnetic and topological materials could be designed independently. Unfortunately, this is not the case when we interface the TI directly with metallic ferromagnets. Previous attempts directly interfacing TIs with 3d transition metals have evidenced the difficulties of controlling the highly correlated properties of each component of the heterostruture. Strong interactions lead to the formation of interdiffused dead magnetic layers [62–67], and to the quenching of helical states, which can only be prevented by the intercalation of less reactive spacers [43, 209].

Strong structural distortions already occur locally at the single 3d impurity level [71, 72, 210], which seems to affect the doping behaviour as well as the magnetic anisotropy. Significant Coulomb interactions with such 3d impurities

generally induce significant charge transfer and hybridization to the Topological Surface State (TSS) [72, 73, 211]. Long-range order of magnetization between surface adatoms is complex to achieve. Their intrinsic doping effect in the TI blocks the mediation of magnetic order by the Dirac surface electrons via Ruderman-Kittle-Kasuya-Yosida (RKKY) [74, 212], meanwhile their uncontrolled adsorption configuration affecting the interatomic distance leads to different electronic and magnetic states [71, 76]. Indeed, the first direct demonstration of long-range interaction between surface 3d impurities indicates the existence of a complex correlation between the size and signature of the interaction and the doping level, and interatomic distance [213], highlighting the need of controlling the spatial distribution and interaction of surface impurities.

Coordinating the bare magnetic atoms with organic ligands offers a promising alternative to control magnetic interactions with the surface, as well as to introduce order in the magnetic molecular lattice [187]. Rational design of ligands and exchangeability of the atoms lead to a vast variety of charge and spin states, and to different adsorption geometries. These have been traditionally explored at metallic surfaces in an extensively manner [90, 91, 94, 166, 173, 176, 214]. Additionally, the fact that they typically present a bandgap is of particular interest for applications in real devices, as it limits the electronic transport only to the TSS.

Likewise, the few systematic studies of molecules on TIs reflect a similar tunability of interactions both by the metal ion [98] and the ligand [215]. Surprisingly, despite the considerably larger distance from the surface as compared to bare impurities, both the molecular ion and the helical state can still be strongly perturbed by interactions. This can lead to charge transfer, destroying the insulating bulk behaviour of the TI [216], to strong hybridization and the formation of interface states, as found for planr FePc [217] and MnPc [218, 219] on Bismuth Telluride (Bi_2Te_3), and more dramaticaly to the burial of helical states into subsurface Quintuple-layer (QL), as recently found for CoPc con Bi_2Se_3 [99]. The later scenario has led to a succeeding study to conclude that planar Metal-organic (MO) molecules are not suitable for non-perturbative interactions [220].

This chapter describes how non-perturbative interfaces can also be attained by using planar organic molecules that expose the magnetic ion directly to the surface, if the ligand and substrate are appropriately chosen. For that, we deposit Cobalt - Tetrakis (4-Promophenyl) Porphyrin (CoTBrPP) on the (0001) surface of the "twin-free" Bi_2Te_3 thin films reported in Chapter 3, and employ a set of complementary techniques to carry out a comprehensive characterization of the interfacial electronic and magnetic properties. The structural and electronic characterization of the molecule is carried out by Scanning Tunneling Microscopy (STM) and Scanning Tunneling Spectroscopy (STS), the magnetic properties of the latter are probed by X-ray Magnetic Circular Dichroism (XMCD) and a full energy-momentum description of the helical Dirac bands (TSS) is obtained by Angle-Resolved Photoemission Spectroscopy (ARPES). Our findings are supported theoretically by Density Functional Theory (DFT) calculations (in collaboration with R. Robles). Finally, a comparative study has also been carried out performing similar coverage dependent ARPES measurements with Cobalt -

Phthalocyanine (CoPc) on the same Bi_2Te_3 surface.

5.1 Study of CoTBrPP Molecules on Bi_2Te_3

5.1.1 Structural Properties

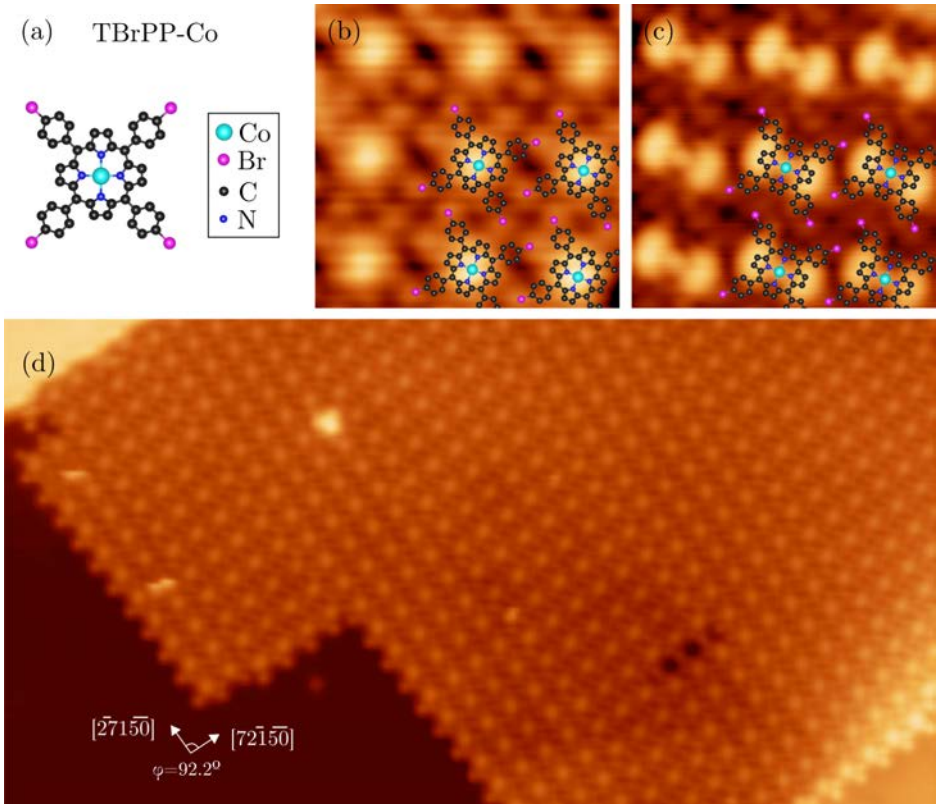

Figure 5.1: (a) Schematic of the CoTBrPP molecule. Constant-current topographic images of the detailed molecular structure scanned at (b) $V_{bias} = 1.6$ V, $I_t = 0.05$ nA, 5×5 nm^2 and at (c) $V_{bias} = -1.2$ V, $I_t = 0.02$ nA, 5×5 nm^2, and of a molecular island adsorbed on Bi_2Te_3 surface $V_{bias} = 1.4$ V, $I_t = 0.01$ nA, 54×28 nm^2 (d). White vectors describe the two crystallographic directions in which the presented molecular lattice is aligned.

The structural characterization of CoTBrPP on Bi_2Te_3 surface is presented in Figure 5.1. CoTBrPP molecules deposited at room temperature aggregate in well structured large islands, as shown in Figure 5.1d. For coverages well below the Mono-Layer saturation, 2D extended islands separated by large areas of clean surface are typically found in contact to substrate steps. It reflects a high surface diffusion rate of the molecules that prevents them to pin in the atomically flat surfaces and promotes nucleation at the substrate steps, a first indication of a

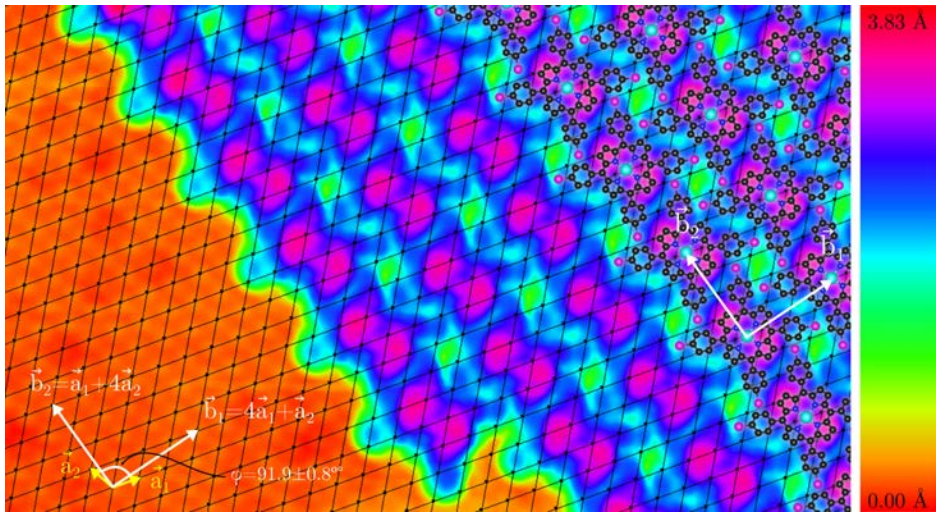

Figure 5.2: STM topographic image measured in constant current mode ($V_{bias} = -1.8$ V, 0.009 nA, 14.5 nm lateral size) with atomic and sub-molecular resolution of a CoTBrPP island on $Bi_2Te_3(0001)$ surface (corresponding to the Domain A described below in the text). Superposed black lattice has been fit to the Te-terminated Bi_2Te_3 surface lattice, and allows the identification of the bridge adsorption site of the molecules. Base vectors of the surface lattice $\boldsymbol{a}_1$ and $\boldsymbol{a}_2$ are represented in yellow and base vectors of the molecular lattice $\boldsymbol{b}_1$ and $\boldsymbol{b}_2$ in white.

weak interaction with the substrate. Molecules present bright circular centres at positive bias (Figures 5.1b and 5.1d), and "dumbbell-like" structure always oriented in the same pyrrole-pyrrole direction at negative bias (Figure 5.1c).

The STM image shown in Figure 5.2 allows a complete description of the molecular lattice: its unit cell, the molecular azimuthal angle with respect to the lattice, and their stacking relation with respect to the surface lattice. Molecular centres are separated by 16.6 ± 0.7 Å and always sit on the same Te-Te bridge position. The molecular lattice vectors ($\boldsymbol{b_1}$ and $\boldsymbol{b_1}$) form an angle of $\varphi = 91.9 \pm 0.8°$ instead of the expected 90° for a square lattice, reducing its symmetry from 4 to 2-fold, so that $\boldsymbol{b_i}$ can be expressed in terms of underlying lattice vectors $\boldsymbol{a_i}$ as follows:

$$\begin{pmatrix} b_1 \\ b_2 \end{pmatrix} = \begin{pmatrix} 4 & 1 \\ 1 & 4 \end{pmatrix} \begin{pmatrix} a_1 \\ a_2 \end{pmatrix} \tag{5.1}$$

This stacking predicts the angle between the molecular lattice vectors to be $\varphi = 92.2°$ and the lattice parameter to be $b_1 = b_2 = \sqrt{52}a/2 = 15.8$ $\mathring{A}$, in excellent agreement with the experimental values, and defines a quasi-square molecular lattice commensurate with the substrate.

Quasi-square molecular lattices were found in three equivalent orientations rotated each by 120° ("rotational" domains shown in Figure 5.3), as expected for a commensurate 2-fold molecular lattice with a 6-fold symmetry (considering the Te-terminated outermost layer). The unit lattice of the three equivalent domains

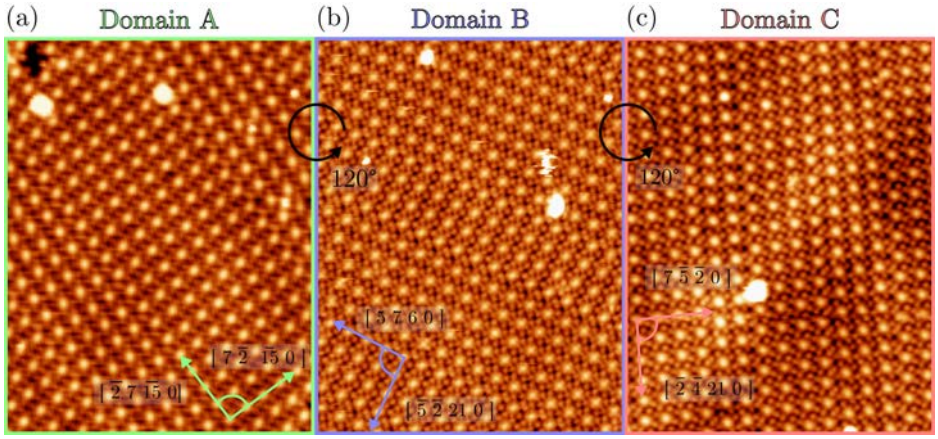

Figure 5.3: STM topographic images measured at constant current mode corresponding to the three possible domains of CoTBrPP on Bi_2Te_3. (a) $V_b = 1.4$ V and 0.026 nA, (b) $V_b = 1.1$ Vand 0.060 nA, and (c) $V_b = 1.3$ V and 0.020 nA. $\boldsymbol{b}_1$ and $\boldsymbol{b}_2$ are the molecular base vectors of each domain expressed in the notation of the HCP crystallographic directions. Images size 25×32 nm^2.

defined by $\boldsymbol{b_i}$ can be expressed in terms of the surface unit lattice vectors $\boldsymbol{a_i}$ by the following relations:

$$Domain\ A: \begin{pmatrix} b_1 \\ b_2 \end{pmatrix} = \begin{pmatrix} 4 & 1 \\ 1 & 4 \end{pmatrix} \begin{pmatrix} a_1 \\ a_2 \end{pmatrix} \tag{5.2}$$

$$Domain\ B: \begin{pmatrix} b_1 \\ b_2 \end{pmatrix} = \begin{pmatrix} -1 & 3 \\ -4 & -3 \end{pmatrix} \begin{pmatrix} a_1 \\ a_2 \end{pmatrix} \tag{5.3}$$

$$Domain\ C: \begin{pmatrix} b_1 \\ b_2 \end{pmatrix} = \begin{pmatrix} -3 & -4 \\ 3 & -1 \end{pmatrix} \begin{pmatrix} a_1 \\ a_2 \end{pmatrix} \tag{5.4}$$

with $a_1 = a_2 = a = 4.38$ Å. A statistical study analysing the orientation of various molecular lattices is reported in Appendix A, confirming the sole presence of the rotational domains and thus reinforcing the model of the commensurate quasi-square lattice.

The non-punctual symmetry of the molecules play an important role in defining their azimuthal orientation. Therefore, it is important to take into account the deformation induced after adsorption on the surface, the saddle conformaiton. It consists of pairs of opposite pyrrole rings tilted upwards and downwards, and opposite phenyl legs rotated in opposite directions around the C-C bond connecting to the macrocycle. It has been widely observed for TPP-based adsorbed on metallic surfaces [91, 173, 221–223]. On our TI surface, the saddle conformation is confirmed by the presence of only one 2-fold symmetric orbital aligned on the pyrrole-pyrrole direction (Figures 5.9a and 5.9b), by the phenyl legs resembling to point towards opposite directions (red arrows superposed in Figure 5.4) and by the DFT relaxed CoTBrPP lattice on Bi_2Te_3 shown in the inset of Figure 5.4a. DFT calculations also reveal that the resulting adsorption distance

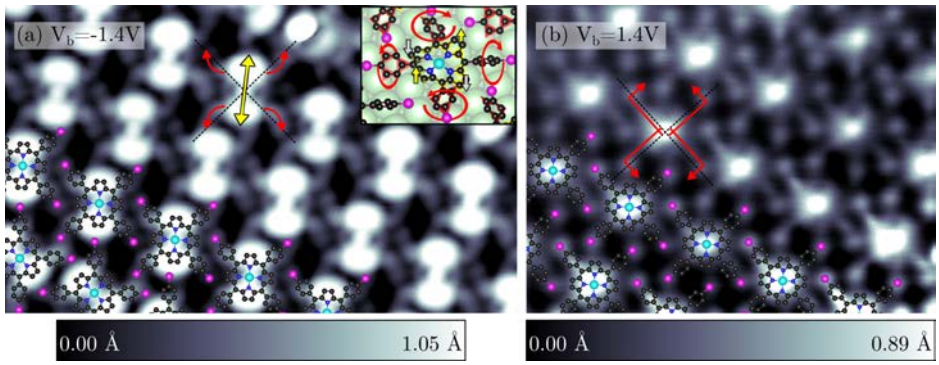

Figure 5.4: STM topographic images of the same CoTBrPP island but slightly different areas, measured in (a) constant current (−1.4 V, 0.029 nA, 10×6 nm^2) and (b) constant height mode (1.4 V, 8×6 nm^2). Features emerging from the molecular saddle conformation are observed in both images; Red arrows depict a non-chiral structure resulting from the rotation of the phenyl groups, meanwhile yellow arrow highlights that only one Co d_{xz} or d_{yz} orbital is visible, and it is aligned with the two up-bended pyrrole groups. Inset: Schematic of CoTBrPP molecule on Bi_2Te_3 surface suffering saddle conformation. (a) and (b) are represented in two different color scales for an optimum visualization.

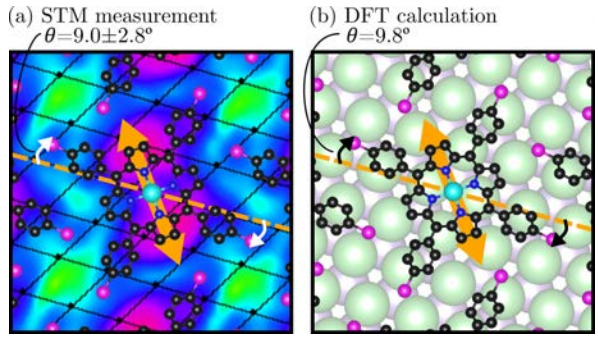

Figure 5.5: (a) STM image and (b) DFT calculation showing excellent agreement in the adsorption site and relative orientation (θ) of the CoTBrPP respect the Bi_2Te_3(0001) surface. Surface lattice has been superimposed on the molecular lattice in (a). Orange double arrows represent the molecule symmetry and dashed orange lines the direction defined by the Te-Te bridge site. Calculations by R. Robles.

is 3.82 Å (defined by the perpendicular distance between the Co ion and the Te plane). Overall, the saddle conformation reduces the apparent 4-fold symmetry to 2-fold.

This 2-fold symmetric appearance reveal that all molecules within the same lattice present the same azimuthal angle, resulting in a complete alignment. The relative orientation between molecules and molecular lattice is $\gamma = 21.7 \pm 2.8°$, as given by the symmetry axis of the Co d_{xz} orbital (orange axis in Figure 5.2) and $\boldsymbol{b_2}$ (white). Meanwhile the relative orientation with respect to the underlying surface is $\theta = 9.0 \pm 2.8°$, defined by $\boldsymbol{a_1}$ and the nearest phenyl direction (θ in Figure 5.5a).

DFT calculations of the quasi-square CoTBrPP lattice were performed in order to assess the energy differences between distinct adsorption sites (top, hollow and bridge) and various molecular orientations with respect to the substrate (θ). They confirmed that the most stable configuration is that defined by a Te-Te

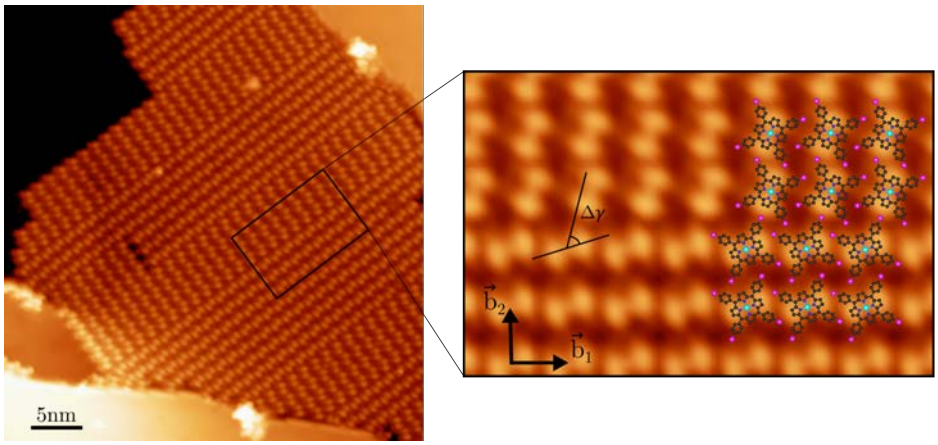

Figure 5.6: STM topographic image measured in constant current mode (−1.3 V, 0.037 nA) shows parallel linear dislocations within one CoTBrPP island, leading to aligned subdomains. Inset of clipped area highlights the relative azimuthal rotation between molecules of adjacent subdomains.

bridge adsorption site and a relative orientation with the substrate of $\theta = 9.8°$, shown in Figure 5.5b. These results are in excellent agreement with the experiments, and represent a big asset to understand the formation of "shifted" subdomains presented subsequently.

Each particular molecular island has been invariably found to be composed by only one rotational domain. Each domain can show different subdomains defined by lateral dislocation line boundary, aligned always parallel to the same molecular axis. These can be observed clearly in the STM images in Figure 5.6, revealing that molecules within adjacent subdomains are translated by around ~ 3 of molecular lattice cell and azimuthally rotated by $\Delta\gamma = 49.0 \pm 2.8°$. By applying this operation to the atomic models shown in Figure 5.7, molecules transiting between subdomains end up in an equivalent adsorption configuration to that defined by the bridge adsorption site and $\theta = 9.8°$ in Figure 5.5b, thus explaining the coexistence of the different subdomains with similar sizes.

More precisely, two similar $\boldsymbol{\Delta r}$ vectors translate the molecules to the equivalent bridge position,

$$\boldsymbol{\Delta r} = \frac{31}{30}\boldsymbol{b_1} + \frac{11}{30}\boldsymbol{b_2} \tag{5.5}$$

$$\boldsymbol{\Delta r'} = \frac{29}{30}\boldsymbol{b_1} - \frac{11}{30}\boldsymbol{b_2} \tag{5.6}$$

Both of them fulfilling $\boldsymbol{\Delta r} \sim \boldsymbol{b_1} \pm \boldsymbol{b_2}/3$, represented in Figure 5.7. The combination of any of these two vectors with $\pm\Delta\gamma$ bring the molecules to the equivalent configurations and describe the formation of the shifted subdomains.

Finally, the fact that linear dislocations appear invariably parallel to each other within the same rotational domain can be explained considering the symmetries of the system. The 6-fold symmetry of the substrate makes the two

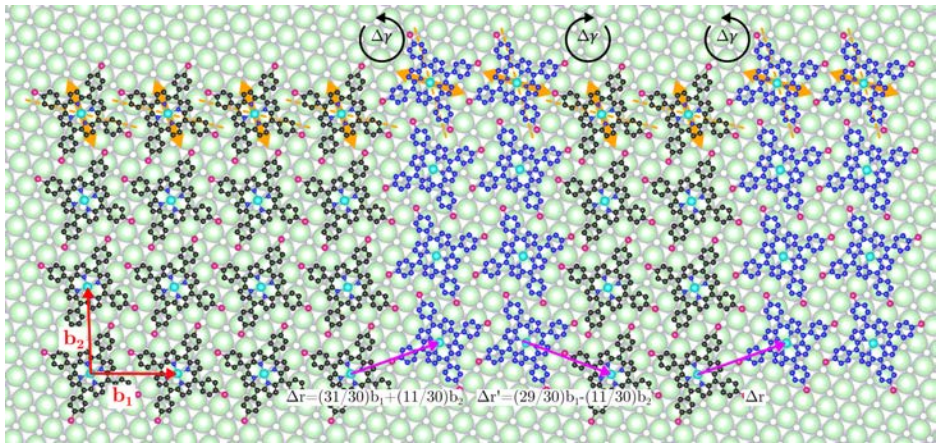

Figure 5.7: Schematic of CoTBrPP on Bi_2Te_3 showing the combined translation and rotation operation that brings a CoTBrPP to an energetically equivalent adsorption configuration, thus describing the shifted subdomains observed on Bi_2Te_3. Orange axis represents the 2-fold symmetry of the molecule and dashed lines highlighting the adsorption bridge site evidence the equivalent adsorption configuration.

possible dislocations at 92.2° with respect to each other energetically inequivalent, thus bringing anisotropy in the formation of subdomains.

Summarizing the structural characterization, the adsorption configuration and self-assembly of CoTBrPP on Bi_2Te_3 is governed by an interplay between inter-molecular and molecule-substrate interactions. The inter-molecular interaction dominates the self-assembly by imposing its 4-fold symmetry over the 6-fold surface at first sight. However, the substrate is capable of pinning the molecules onto Te-Te bridge sites, defining an optimum azimuthal angle. The commensurability with the surface lattice forces a slight distortion of the square molecular arrangement, and introduces 3 equivalent orientations. Finally we find that each of these domains contain arrays of parallel linear dislocations that separate molecular crystal structures where the lattice is shifted parallel to the boundary by $\sim 1/3$ of lattice vector, and the molecule rotated by 49°. This combined operation brings the molecule to the same minimum energy adsorption configuration an explain the coexistence of domains of similar size. The overall scenario scenario described by the structural study is that of a fairly but not completely decoupled molecule / TI interface, which can fit in the range of an interacting but non-perturbating heterostructure interfaces, as shown in the following sections.

5.1.2 Electronic Properties

In order to assess the electronic structure of the molecular lattice adsorbed on Bi_2Te_3 surface, STS measurements at the single CoTBrPP level were performed. Spectroscopy acquired on different sites of the molecule show the most representative electronic features (Figure 5.8a). Spectral features can be assigned to different molecular levels by comparing them with theoretical predictions and

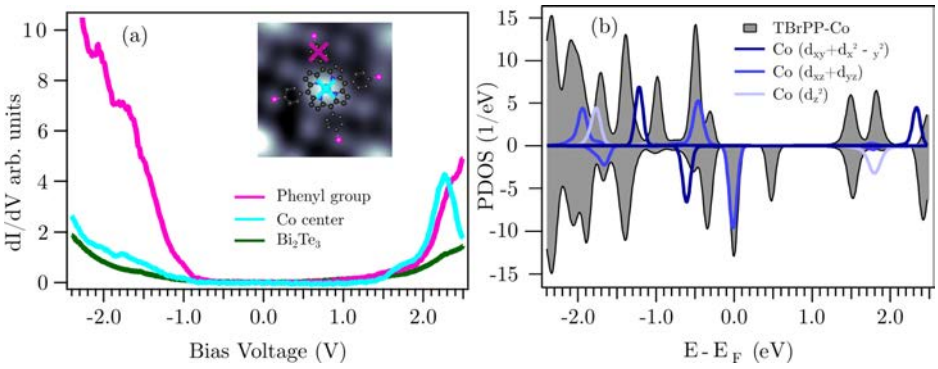

Figure 5.8: (a) STS spectra measured on top of a phenyl group (pink line), on the Co atom (light blue) and on the clean Bi_2Te_3 (green) as reference. Inset: Topographic image acquired in constant-height mode ($V_{bias} = 0.6$ V, 2.5×2.5 nm^2). (b) DFT-calculated DOS projected on the Co d states (blue lines) and on the whole molecule (grey shadowed line). Calculations by R. Robles.

conductance maps. In order to do that, Projected Density of States (PDOS) spectra were DFT-calculated (Figure 5.8b) and constant height dI/dV maps covering a molecular unit cell were taken (Figure 5.9) respectively.

The first noticeable spectral feature in STS is a large flat gap of ~ 2.5 V, defined by intense onsets emerging at -0.9 V and at 1.6 V, corresponding to the HOMO and LUMO tails respectively. The onset at negative energy presents a double peak structure at -2.0 V and -1.8 V, corresponding a 2-folded feature possessing charge density on two opposite pyrrole rings in the conductance maps. This is the characteristic shape of the d_{xz}/d_{xy} orbitals, and shows a qualitative agreement with the DFT calculations, as these are also the first spectral features appearing at negative bias. The map at gap energy (-0.2 eV) was acquired at a significant smaller distance than the rest because of the faint intensity, mostly coming from the Tetraphenyl Porphyrin (TPP) ligand. It reveals the absence of any d orbital within the gap, again in agreement with the calculations. A bright protrusion with spherical symmetry is observed in the maps taken at 2.1 V and 1.6 V, signature of the d_{z^2} orbital. This is consistent with the calculations, as d_{z^2} is also the first orbital appearing at positive bias. The d_{z^2} vanishes at higher bias voltages, as observed in the STS and the calculations, and evidenced by the emergence of a 4-fold structure in the conductance map taken at 2.4 eV. Additionally, most of the predicted d peaks (blue lines in Figure 5.8b) show a symmetric and sharp shape, an evidence of no sign of hybridization with the conduction electrons of the substrate.

This scenario contrasts with the electronic structure of the same CoTBrPP molecule on Au(111) reported in Chapter 4, showing the presence of hybrid d levels near E_F. Such differences can be explained in terms of intra-molecular Coulomb repulsion (U); the lower density of conduction electrons at the TI surface, as compared to a metallic substrate, induces a smaller screening potential to the molecule that leads to a higher U. The effect of U is to separate singly

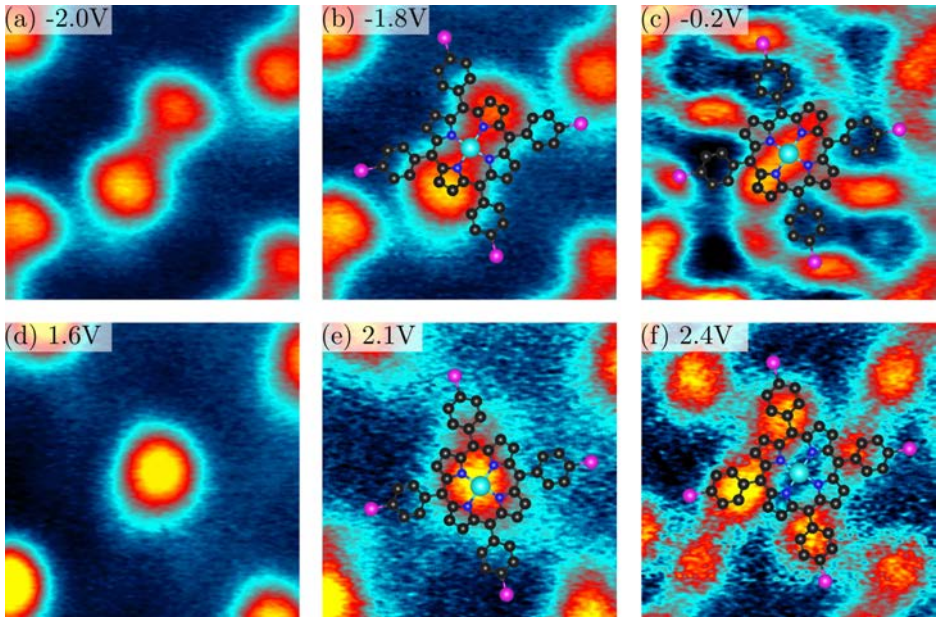

Figure 5.9: (a) - (f) Constant height dI/dV maps of the same molecule where dI/dV spectra were taken (25.5×25.5 nm^2). Molecule-tip distance was set individually for each bias voltage, in order to maximize the tunneling current.

and doubly occupied levels, and eventually pull them away from E_F. This is corroborated by the DFT calculations, as a relatively large Coulomb repulsion ($U - J = 2$ eV) has been used in order to best fit the spectral features of the experimental data. Otherwise, the use of lower U values leads to configurations with smaller gaps, incompatible configurations with our system.

Overall, the large gap and the lack of hybridization signs showed by the electronic characterizaion define a well decoupled molecular layer from the substrate. This is in contrast to more interacting systems reported in previous studies, such as TMPcs on metallic surfaces, where Coulomb interactions can induce charge transfer between molecules and substrate, responsible of charge reorganization within the molecule [90, 94, 224], or even hybridization involving d_{z^2} orbitals [94, 167, 174].

5.1.3 Magnetic Properties

In order to examine how the electronic decoupling correlates with the molecular magnetic properties, an XMCD study (complemented by X-ray Absorption Spectroscopy (XAS)) was carried out. XMCD measurements were performed at 7.5 K, using normal (0°) and grazing (70°) photon incidence to probe magnetic anisotropies. More details about the experimental geometry can be found in Chapter 2. The samples consisted on $\lesssim 1$ ML of CoTBrPP on Bi_2Te_3, as determined by the intensity increase of the XAS Co L_3 edge, previously calibrated with

in-situ STM measurements. Nevertheless, the data presented in this section was acquired in a different sample than those used in the STS study in the previous section.

Figure 5.10a shows XAS spectra at the energy range of Co $L_{2,3}$ edge, at normal and grazing incidence, that is sensitive to the in-plane and out-of-plane projection of the unoccupied Co d orbitals. As described in Chapter 4, this is characterized by the presence of a sharp intense peak at the low energy side (777 eV), which represents a transition to the unnocupied d_{z^2}, as can be observed by the strong angular dependence and negligible intensity in the out of-plane spectra. This lineshape is comparable to the well decoupled cases of CoPc multilayers on Au(111) [167] and CoOEP on graphene [184], but differs considerably with the more interacting single layer CoPc on Au(111) system, where multiplets are broadened by the higher degree of electronic interaction with the substrate and the d_{z^2} peak is substantially suppressed [167].

Remarkably, the magnetic moment of CoTBrPP is not quenched upon adsorption on the Bi_2Te_3 surface, in contrast to CoTPP on Au(111) and on Ag(111) [182], where no dichroic signal is observed at the Co L edge. The XMCD signal, although accompanied by a broad shoulder that covers the whole L_3 multiplet, is dominated by the sharp d_{z^2} contribution. The negligible signal in the out-of-plane direction indicates a strong in-plane magnetocrystalline anisotropy, as expected for a d_{z^2} system. An accurate quantitative measurement of the effective spin and the orbital magnetic moments by sum rules is not possible due the presence of the Ba M $_{3,4}$ edges in the same energy range as the Co $L_{2,3}$. They emerge from the BaF_2 substrate in which Bi_2Te_3 are grown (see Chapter 3), and impede the proper determination of the Co $L_{2,3}$ XAS intensity. In any case, from the XAS spectral multiplet lineshape and the angular dependence of XAS and XMCD, one can qualitatively assign the observed behaviour to a $S = 1/2$ system, with a single unpaired electron in the d_{z^2} level, as expected for Co^{2+} in a square planar ligand field.

Therefore, we can assert that XAS and XMCD results corroborate the weak interaction between the molecular lattice and TI, which had already been suggested by the structural and electronic STM study. They describe an interface where the CoTBrPP molecules maintain their pristine magnetic properties upon adsorption, which together with the persistence of unperturbed TSS constitutes an essential ingredient for the rational engineering of magnetic TI interfaces. Although one would be tempted to attribute this effective decoupling solely to the corrugated nature of the ligand and the corresponding increased separation of the Co ion from the surface, the choice of TI also seems to play an important role in the interfacial interactions, as it is presented in the following section.

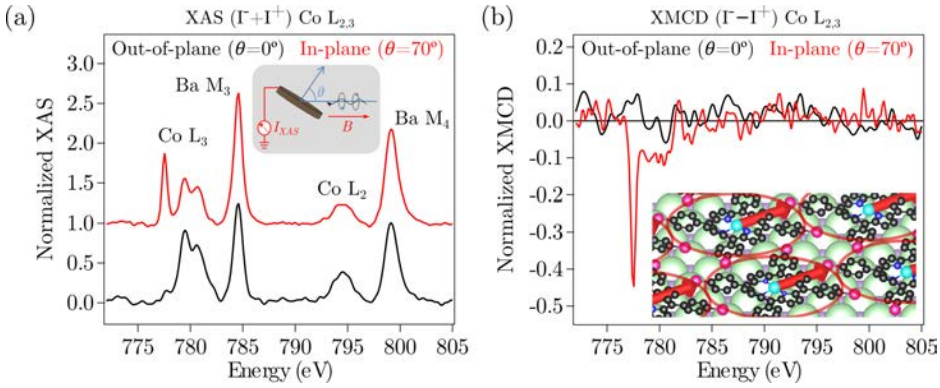

Figure 5.10: (a) XAS and (b) XMCD spectra, measured at the Co $L_{2,3}$-edge energy range. Normal ($\theta = 0°$) and grazing ($\theta = 70°$) X-ray incidence are represented by black and red lines respectively. Spectra are represented as the average ($I^- + I^+$) and difference ($I^- - I^+$) of the negative and positive circularly polarized absorption, respectively. Features at 784 eV and 799 eV are attributed to the Ba M_4-edge, as BaF_2 is the substrate where Molecular Beam Epitaxy (MBE) Bi_2Te_3 thin film was grown. Measurements were done close to the saturation point of magnetization, with an applied magnetic field of $B = 6\ T$ always parallel to the beam, with the sample at $T = 7.5\ K$.

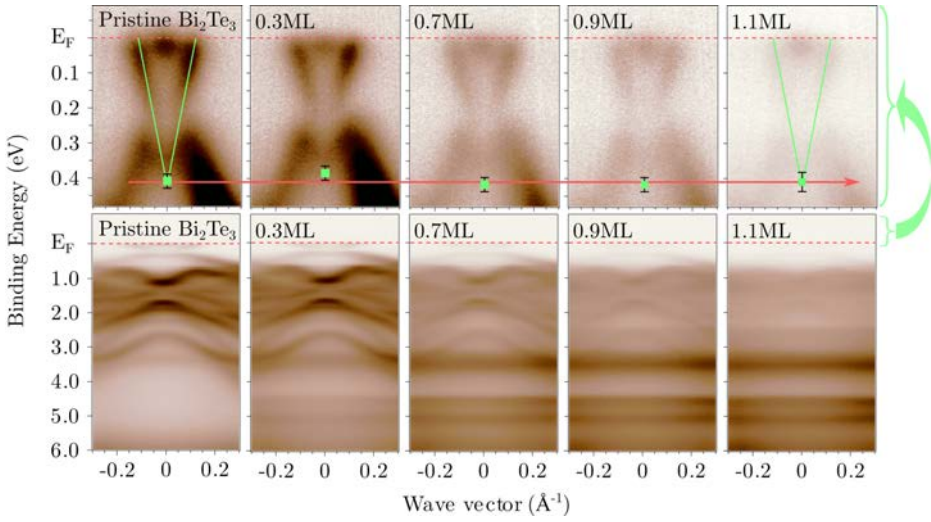

Figure 5.11: ARPES intensity maps in the top panels show the TSS evolution of Bi_2Te_3 upon CoTBrPP coverage, and of the bulk bands and molecular levels in the bottom panels. Green linear fits to the Dirac cones highlight the presence of unperturbed TSS upon coverage, red arrow crossing the upper panels acts as a guide for the eyes depicting the horizontal trend of the Dirac point. Intensities in the top and bottom maps have been normalized by a common factor in each row, so that absolute changes can be appreciated.

5.2 Study of Bi_2Te_3 upon Deposition of MO molecules

5.2.1 Electronic Properties upon CoTBrPP Deposition

An ARPES study as a function of the CoTBrPP molecular coverage was performed in order to assess the impact of the CoTBrPP molecules on the Dirac surface states. The data presented in this section was measured at 77 K, and corresponds to a sequence of X-ray Photoemission Spectroscopy (XPS) and ARPES acquisitions preceded by in-situ evaporations on Bi_2Te_3. A complete description of the experimental setup can be found in Chapter 2. The data presented in this section was acquired in a different sample than those used in the STM and XMCD studies of the previous sections. In order to confirm the compatibility between them, XPS measurements were performed here to probe the molecular integrity (not shown here), and calculate the molecular coverages (see Appendix B).

Top panels in Figure 5.11 were acquired in a narrow energy range to observe the characteristic Bi_2Te_3 surface state, i.e. the Dirac cone. On the other hand, the measurements in the bottom panels cover a wider energy range so that the evolution of the Bi_2Te_3 bulk bands and molecular levels against the coverage can be appreciated. The coverage values reported in this section were calculated from the attenuation of the substrate Bi $4f_{7/2}$ peak, as explained in Appendix B.

The spectral evolution as a function of molecular coverage shows a gradual decrease of the Dirac cone intensity, which at first sight point towards a quenching of the TSS. However if one normalizes the intensity of the Dirac bands to that of bulk bands observed in the lower panels, a constant trend is obtained, as shown in Figure 5.12, meaning that the signal from both Dirac and bulk levels is decreasing at the same rate. This is indeed expected if the only effect is the attenuation of photoelectrons by the molecular overlayer.

In parallel, a careful analysis of the evolution of Dirac point energy with the coverage reveals that no charge transfer takes place between the molecular layer and the Bi_2Te_3. It is highlighted by the horizontal trend of the red arrow following the Dirac points (green square markers in Figure 5.11). Since the Dirac point in Bi_2Te_3 is embedded in the bulk valence band, their energy was acquired by extrapolating Dirac bands down to their intersection point in each ARPES map. This extrapolation was done by first taking various Momentum Dispersion Curves (MDCs) in the Dirac cone range, second by fitting Lorentzian functions to the MDCs, and finally by interpolating between the maxima of the Lorentzian fits.

This finding differs from most of the Pc-based on TI systems studied so far, where significant charge transfer shifts the Fermi level in to the bulk conduction band [98, 99, 215, 218, 219]. More remarkably, the counterpart CoPc molecule, with the same Co^{+2} ion in a square planar ligand environment as CoTBrPP, when deposited on Bi_2Se_3 can even quench the spectral weight of the TSS at the outermost QL for coverages > 0.73 ML [99]. Motivated by this different

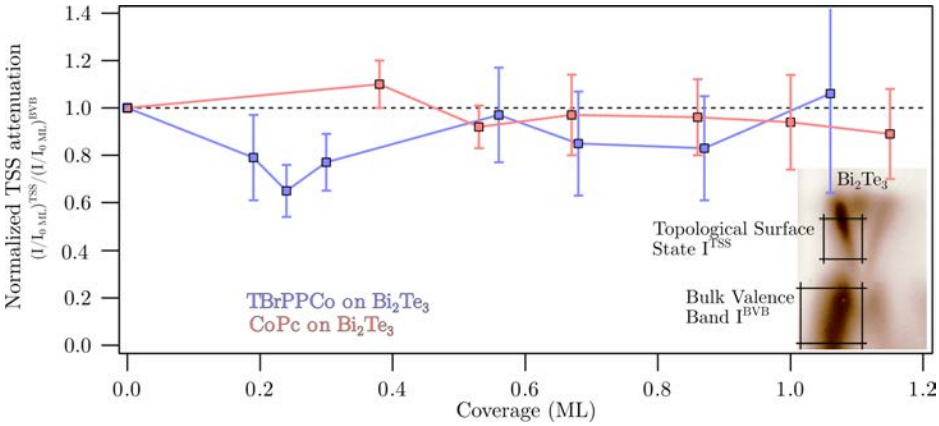

Figure 5.12: (a) Evolution of ratio between the photoemission intensity coming fro the TSS and bulk valence band with the molecular coverage. Intensities for each coverage point have been integrated over the defined areas in the ARPES map in the inset, and later normalized to the initial value of each system.

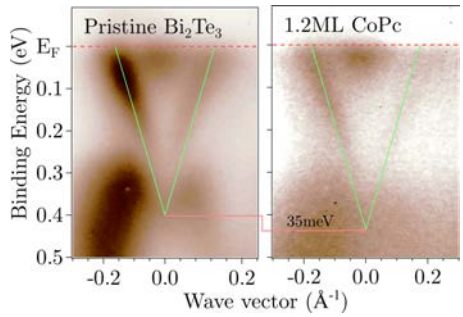

Figure 5.13: ARPES intensity maps showing the TSS for the pristine Bi_2Te_3 surface and after adsorption of 1.2 ML of CoPc. Green fits highlight the presence of the Dirac cone. Intensities have been normalized separately in each image for an better visualization of the features.

behaviour, we decided to extend our studies to CoPc on Bi_2Te_3.

5.2.2 Electronic Properties upon CoPc Deposition

Figure 5.13 shows a similar coverage dependent ARPES study as that shown for CoTBrPP. In stark contrast to that measured in Bi_2Se_3, CoPc does not seem to quench the TSS of the Bi_2Te_3, as it is evidence by the presence of the Dirac bands for > 1 ML of coverage. Nevertheless it does induce a sizeable n-doping of 35 meV. Note that molecular coverages were determined as in Appendix B.

These results highlight the role of the ligand in controlling interactions at the surface. The fact that the interactions still remain in the non-perturbative regime for both compounds in Bi_2Te_3, where only a slight charge transfer can be seen for the more interacting CoPc, suggest that ligand chemistry could also be used to tune magnetic interactions without affecting the properties of each constituent, namely the MO molecule and the TI.

5.3 Summary

Summarizing the combined STM, ARPES and XMCD study showed in this chapter, we find that the two explored Co-based MO compounds adsorbed on Bi_2Te_3 form a robust interface where both TSS and magnetic properties of the molecular film are conserved pristine.

Evidences for weak, non-perturbative interactions have been identified in all explored properties: structurally, the quasi 4-fold symmetry of the molecular lattice indicates that inter-molecular interactions dominate over those with the underlying 6-fold surface. Yet, the interaction with the surface is strong enough to force a commensurate bridge-type stacking of the Co ions by slightly distorting the square lattice, and to induce a 3-fold domain multiplicity. These results are in contrast with the case of CoPc on Bi_2Te_3 [98] (and on Bi_2Se_3 [99]), where the observed hexagonal arrangements reveal a dominating interaction with the substrate. Electronically, the largely split Co d orbitals, and in particular the sharp unoccupied d_{z^2} orbital probed by STS, indicate weak molecule-substrate hybridization and screening. This is supported by DFT calculations. Regarding the TSS probed by ARPES, we find that they are barely affected by the molecular film, with no indication of doping or variation in the dispersion. Finally, the Co ion d states probed by XAS and XMCD reveal an identical configuration as for decouopled molecules, with an in-plane easy axes that agrees with a $S = 1/2$ in the d_{z^2} orbital.

The overall results lead us to the conclusion that the non-perturbative regime in this surface is robust, and the comparison to the behaviour of CoPc on Bi_2Se_3 highlights the relevance of the substrate electronic properties. Although a direct footprint of magnetic interactions between the molecular spin and the TSS has not been obtained, from the differences found in the self-assembly and doping of Dirac bands when going from CoPc to CoTBrPP on Bi_2Te_3, we expect that ligand chemistry in Bi_2Te_3 could be employed to tune the magnetic interactions between Co ions and helical states within this non-perturbative regime.

Chapter 6

Metal-organic Topological Insulator Heterostructures: Coordination Phase

The bottom-up self-assembly of molecules on atomically clean and flat surfaces can be a very efficient method to fabricate supra-molecular structures. For many years, this approach has been widely employed to grow an unlimited variety of 2D molecular structures by the use of weak inter-molecular interactions [225–228]. A more interesting approach is the synthesis of covalent or metal-coordinated molecular structures, created by the surface-assisted reactions of molecular precursor buliding blocks [82]. The 2D confinement in the presence of a catalytic surface can lead to novel reaction pathways that give rise to polymers that can not be synthesized in solution [229], or can hardly be deposited under clean conditions. As of the chemical nature of such bonds, the obtained nano-structures exhibit high stability and robustness, and can certainty enable for more efficient charge transport [82, 230–232] and magnetic interactions [100–102].

Covalently-bonded or metal-coordinated networks have traditionally been realized on metallic substrates because of their high reactivity capable to catalyse several reactions. Nevertheless, it is highly desirable to transfer the synthesis mechanisms from metals to bulk insulating materials in order to expand the functionalities of such structures. On the one hand, for the use of their pristine properties it is crucial to decouple their electronic structure from the underlying support. On the other hand, it is interesting to extend beyond molecule-metal heterostructures in the search of novel phenomena, as it is the aim of this thesis. To this end, it is highly desirable to transfer the synthesis mechanisms from metals to semiconductor and bulk insulating materials, a pursuit that has been rarely studied [233–235]. The major limitation in this direction is the weaker reactivity of these materials as compared to metals, which frequently leads to desorption before reaction initiation upon annealing.

Topological Insulator (TI) surfaces represent an intermediate case where the

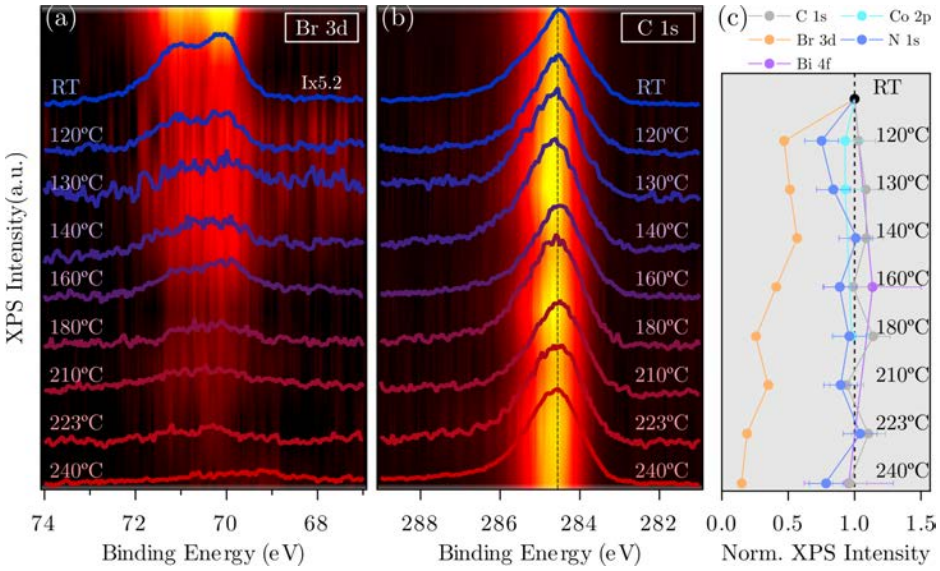

Figure 6.1: Temperature dependence (a) Br 3d and (b) C 1s XPS peaks of the CoTBrPP molecules on Bi_2Te_3 evidencing the complete dehalogenation. XPS intensity maps in the background have been built by interpolating the plotted spectra. (c) Intensity of Bi 4f, C 1s, N 1s, Co 2p and Br 3d peaks normalized to their initial values indicating that molecules are not desorbed during the dehalogenation.

metallic Topological Surface State (TSS) still provide a reasonable reactivity to the otherwise insulating material [133, 236]. One could use this finite reactivity for the on-surface synthesis of coordination and covalent networks of magnetic molecules, where ordered arrays of interacting spins could be engineered. This would prevent them from surface diffusion [210, 237] or intercalation inside the TI bulk [67, 238–240], at the same time that would allow a gradual control over the magnetic interactions occuring at the interface. M. Otrokov et al. [97] theoretically predicted that Co- and Cr- based coordination networks deposited on a TI exhibit long-range magnetic ordering and induce magnetic proximity effect, breaking time reversal symmetry. Experimentally, a few recent studies have focused on weakly interacting molecular enssembles on TIs, confirming that interfacial interactions can effectively be tunned by means of rational design of the ligand and the metallic centers [98, 215–217, 219, 220, 241, 242]. Nevertheless, no covalent or coordination Metal-organic (MO) network on TI has been reported to date.

In this chapter we report the on-surface synthesis of MO coordination networks on TI. Our initial system consists of Br-functionalized CoTPP deposited on the (0001) surface of a "twin-free" Bismuth Telluride (Bi_2Te_3) (see Chapter 3). Two different coordination phases are formed at different activation temperatures, both related to a different degree of coordination of the C radicals created by the dehalogenation with Te atoms. The final structure is hence a bimetallic co-

ordination network, where Co-based MO molecules are coordinated by Te atoms. We track the chemical reaction by X-ray Photoemission Spectroscopy (XPS), and investigate the morphological and electronic properties of the resulting products by combining Scanning Tunneling Microscopy (STM), Scanning Tunneling Spectroscopy (STS) and Density Functional Theory (DFT) calculations (performed in collaboration with R. Robles). Furthermore, Angle-Resolved Photoemission Spectroscopy (ARPES) measurements reveal that the TSS is unperturbed upon the synthesis of the MO coordination structures.

6.1 Thermal Evolution of CoTBrPP on Bi_2Te_3

The thermally induced chemical changes in the molecule were tracked by measuring XPS as a function of reaction temperature. XPS spectra shown in this section correspond consecutive annealing cycles done to the sample at incremental temperatures. The experiment was repeated in four different samples finding consistent results.

Figures 6.1a and 6.1b show how the intensity of the Br 3d peak undergoes an abrupt decrease at the first annealing step at 120°C and smoothly decreases close to zero in the $120 - 240$°C range. This continuous decrease is not accompanied by the rise of any other component related to Te-bound Br atoms, indicating that these are desorbed as they cleave out of the molecule. In contrast, the N 1s and C 1s peaks remain constant in intensity and energy over the temperature range studied, indicating that the molecular coverage and integrity is not varied during dehalogenation. This is corroborated by the constant intensity of the Bi 4f peak found in the whole temperature dependent series. Knowing that the explored temperature range goes beyond the multilayer desorption threshold, the constant C and Bi peak intensities also imply that our initial coverage is within the sub-monolayer regime.

6.2 Morphology of Te-coordinated Structures

In order to assess the morphologic structure of the dehalogenated product, STM measurements were performed after consecutive annealing cycles at incremental temperatures. STM images shown in this section correspond to measurements done in two samples, different from those used for the XPS study in Section 6.1.

After deposition at RT, we find the same self-assembled phase described in the Chapter 5, which we call van der Waals (vdW) phase (Figure 6.2). This phase was showed to be stable up to 180°C annealing temperature. Above this temperature, two distinct structural phases emerge at 200°C and 230°C respectively.

6.2.1 Dimeric Phase

The first phase consists of periodic molecular islands like the on presented in Figure 6.3a. At positive bias, their lattice can be constructed by using an array of spherical bright protrusions, zig-zag aligned in one direction and linearly

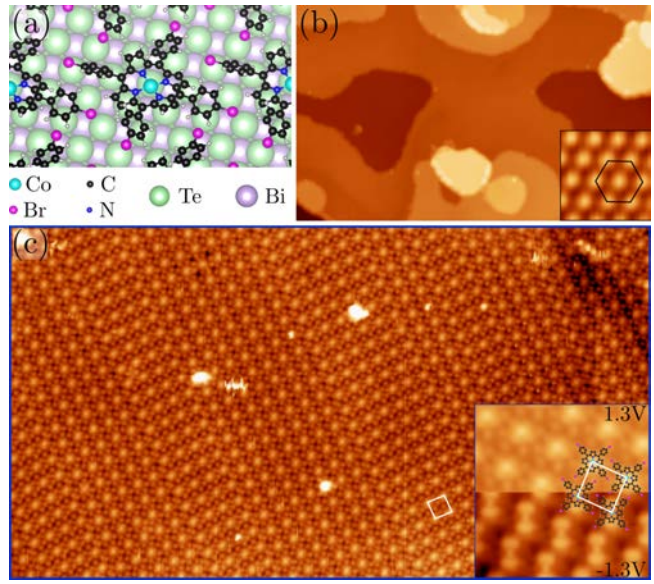

Figure 6.2: Initial vdW phase: (a) CoTBrPP adsorption geometry on $Bi_2Te_3(0001)$ simulated by DFT. (b) STM image of the clean surface of the substrate ($V_{bias} = 1.5$ V, 0.044 nA, 200×122 nm^2), and atomically resolved STM image showing the hexagonal lattice with constant $a = 4.38$ Å in the inset. (c) STM image of the CoTBrPP self-assembly on Bi_2Te_3 ($V_b = 1.1$ V, 0.060 nA, 34×19 nm^2), and intra-molecular resolved STM image showing quasi-square lattice with constant $a = 15.8$ Å (0.022 nA, 7.1×7.1 nm^2, V_{bias} was switch from 1.3 V to -1.3 V during the acquisition).

aligned in another direction (highlighted by zig-zag and straight light blue lines respectively in Figure 6.3b). Straight lines are separated by 14.1 ± 0.2 Å and 15.0 ± 0.2 Å alternatively, thus arranging in pairs. At negative bias, the bright protrusions are replaced by the dumble-like orbitals already observed in previous chapters. With this information, the position of the Co central ion and azimuthal angle of the molecule is defined. By superimposing a CoTBrPP model on each protrusion, oriented in the corresponding azimuthal angle, a molecular lattice is depicted. Every two molecules, columns of double-lobed protrusions appear at negative bias (straight green lines in Figure 6.3c). We tentatively assign this pair of dots to a Te pair that would be coordinated to the nearby molecules, based on the fact that halogen cleavage leaves an unsaturated C radical at this position.

Brigth dots appearing between molecules upon the formation of metalorganic networks have often been identified as the coordinating metal atoms [243–249]. In our case, Te atoms incorporated from the substrate are the most foreseeable candidates because of the natural tendency of Bi_2Te_3 crystals to form Te vacancies upon annealing [153], although in principle the contribution of Bi atoms can not be ruled out. In this line, DFT calculations were performed in order to assess the stability (in gas phase) of a CoTPP dimer mediated by two Te or two Bi atoms. The results, summarized in Figure 6.3d, reveal that the formation of Te-coordinated dimers is indeed stable with an energy gain of $E_B = 0.46$ ev, whereas the Bi-coordinated dimers would be unfavourable by $E_B = -0.59$ eV. This result endorses the proposed dimeric model, in which adjacent molecules are coordinated two Te atoms.

Figure 6.4 shows further evidence of the presence of coordinated dimers in the observed structures. Figure 6.4a for example, contains a double molecular

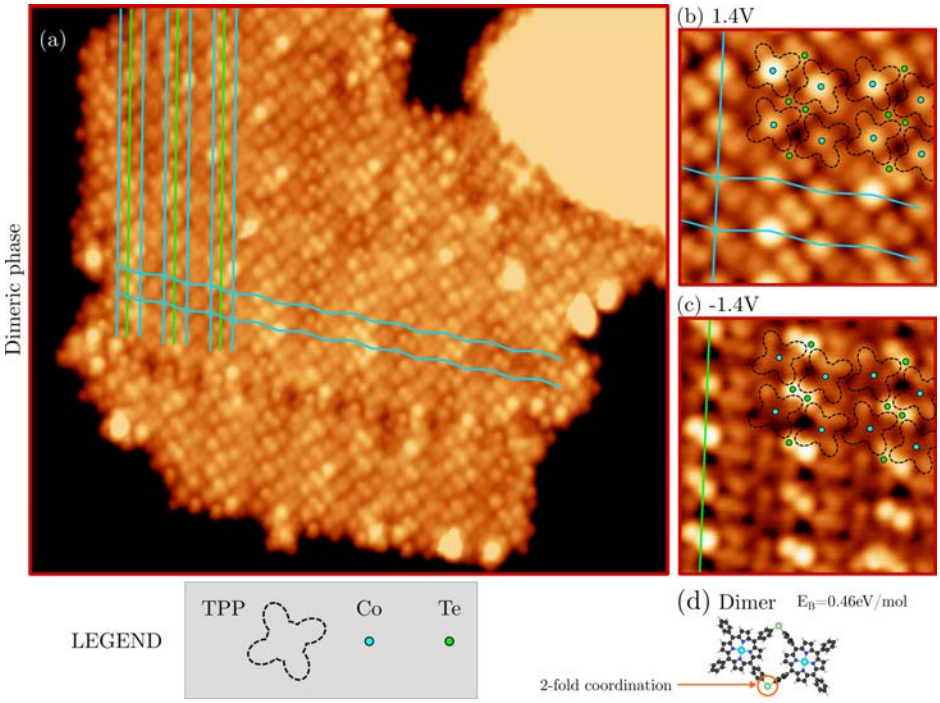

Figure 6.3: STM topographic images of the first CoTPP coordination structure on Bi_2Te_3 (dimeric phase): (a) $V_{bias} = 1.4$ V, 0.017 nA, 49×44 nm^2, (b) $V_{bias} = 1.4$ V, 0.020 nA, 8×8 nm^2, (c) $V_{bias} = -1.4$ V, 0.023 nA, 8×8 nm^2. DFT calculations modelling the Te-coordinated (d) dimers. Calculations by R. Robles.

vacancy, which are very rarely observed in monomeric vdW structures, but constitute the minimum vacancy unit in a lattice of coordinative dimers. The edges of the domain presented in Figure 6.4b, on the other hand, hold a strong evidence supporting the assignment of bright intermolecular dots to coordination units. Here, the double dot becomes a single one, as should correspond to the presence of a single dimer to be coordinated at the edge.

The formation of covalent intermolecular bonds upon debromination can be excluded from the bonding geometry. The rigid and directional C-C bonds can only be formed in the plane by maintaining the sp^2 bonding geometry, hence forming a square network with the phenyl groups of adjacent molecules. That is molecules facing to each other with phenyl axis forming 180 ° as shown in Figure 6.5a. These covalent network structures are found after dehalogenation of porphyrins in noble metals, as shown in Figure 6.5 for Au(111) and Ag(111). In contrast, the structures formed on Bi_2Te_3 show an angle of 90 ° between phenyl groups of the two coordinated molecules. This geometry is allowed by the more flexible coordinative bond, as has been widely observed in different metal-coordinated porphyrin-based structures [246, 250–257].

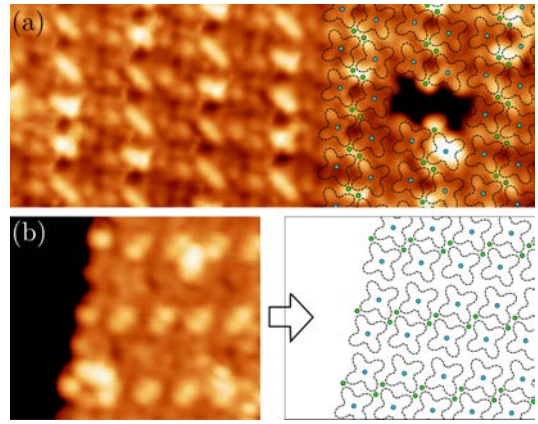

Figure 6.4: STM topographic images of different dimer lattices presenting (a) a lattice vacancy ($V_{bias} = -1.3$ V, 0.018 nA, 21×9 nm^2), and (b) a lattice edge ($V_{bias} = -1.6$ V,0.072 nA, 10.1×9 nm^2).

6.2.2 Polymeric Phase

The Dimeric phase persists upon annealing at 220°C, while annealing at 230°C leads to the new structural phase presented in Figure 6.6a. Unlike the extended and ordered islands in the Dimeric phase, it consists of molecular aggregates forming structures of apparent stochastic geometries. As well as in the vdW and in the Dimeric phases, the molecular centres in this new phase are well identified by using the bias-dependent contrast of the Co sites, appearing as spherical and dumbell protrussions at positive and negative bias respectively. Using this features, Co atoms are identified and labelled with light blue solid circles in Figures 6.6b and 6.6d. The additional intermolecular protrusions, which can be assigned to coordinative Te atoms, are labelled with green solid circles in Figures 6.6b and 6.6e. The resulting structure seems to be an extension of the dimeric structures into longer Te-coordination chains. These appear to merge forming kinks and aggregating in disordered structures of a few tens of monomers. Complementary STM images are presented in Figure C.2 in Appendix C for a more extensive and detailed view of the morphological structure of this phase.

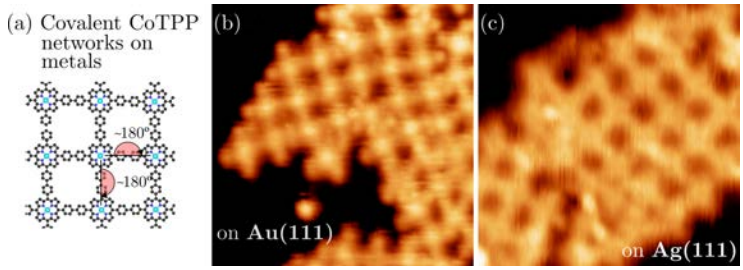

Figure 6.5: (a) Schematic of the covalent networks formed after the debromination of CoTBrPP on (a) Au(111) and (b) Ag(111). STM topographic images (8×8 nm^2) were taken at constant current mode, at 1.1 V (0.625 nA) and $V_{bias} = 0.6$ V (0.160 nA) respectively. Both of them courtesy of J. Hieulle.

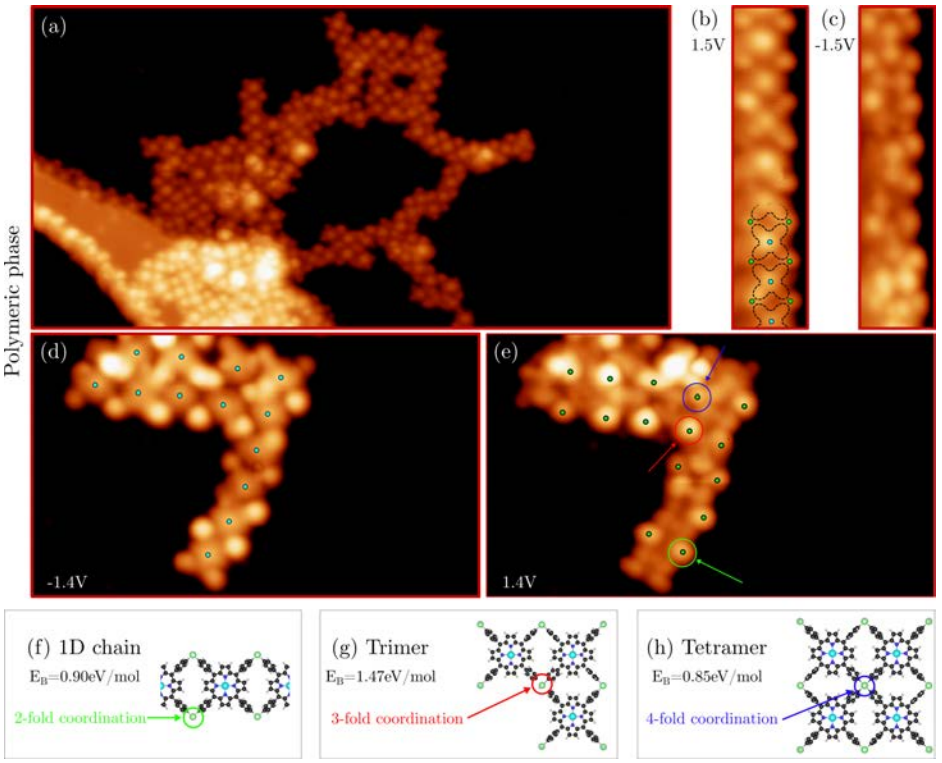

Figure 6.6: STM images of to the second CoTPP coordination structure on Bi_2Te_3 (Polymeric phase): (a) $V_{bias} = 1.4$ V, 0.019 nA, 56×29 nm^2, (b) $V_{bias} = 1.5$ V and (c) $V_{bias} = -1.5$ V (0.044 nA, 2.8×12 nm^2), (d) $V_{bias} = 1.4$ V and (e) $V_{bias} = -1.4$ V (0.017 nA, 17×10 nm^2). DFT calculations modelling the different Te-coordination numbers found: (f) infinite 1-dimensional chains (n=2), (g) trimers (n=3) and (h) tetramers (n=4). Calculations by R. Robles.

Figure 6.7 presents DFT calculated binding energies for different Te-coordinated porphyrin structures. Trimers (containing one 3-fold coordinated Te atom) appears as the most stable structure to the detriment of less energetically favourable dimers or 1D chains (containing 2-fold coordinated Te atoms), and tetramers (containing one 4-fold coordinated).

The binding energies of different coordination structures calculated by DFT are ploted in Figure 6.7, whereas different examples are represented in Figures 6.7f and 6.7h. In particular, the energetic stability of an infinite one-dimensional CoTPP chain ($[Te_2\text{-CoTPP}]_n$) mediated by two doubly coordinated Te atoms validates the experimentally observed Te_2-CoTPP structure. Similar chains in which porphyrin molecules are mediated by two metal atoms can be found in the literature [254, 256, 258, 259]. Furthermore, the merging of chains, kinks of 90 ° and clusters presented in Figure 6.6a and enlarged in Figures 6.6d and 6.6e suggest that the Te linker has variable coordination number. DFT calculations for a porphyrin trimer (Te_8-$[CoTPP]_3$, Figure 6.6g) and for a tetramer (Te_9-$[CoTPP]_4$

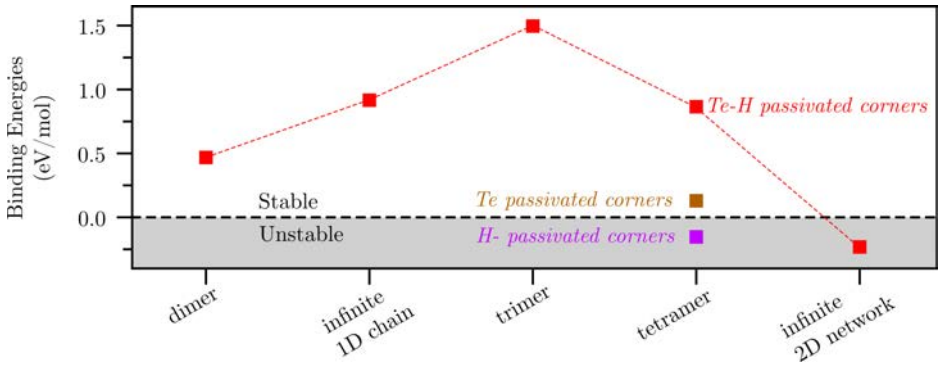

Figure 6.7: Calculated binding energies for the dimer, one-dimensional infinite chain (both containing 2-fold coordinated Te atoms), trimer (containing one 3-fold coordinated Te), tetramer (containing one 4-fold coordinated) and infinite 2D network (containing 4-fold coordinated). Calculations by R. Robles.

, Figure 6.6h), assert the energetic stability of 3- and 4-fold Te atoms coordinating CoTPP monomers. For finite clusters, the energetic stability depends on the different passivation configuration of the peripheral C atoms where molecules do not meet each other, as shown in Figure 6.7 by the tetramer case. In any case, both Te and hydrogenated Te passivation of this corner C atoms lead to stable configurations, and could explain the tendency of forming beyond chain structures with higher coordination number (see for instance Figure 6.6e, and Figure C.1 in Appendix C). However, calculations clearly determine that extended 2D clusters with 4-fold coordinated Te are highly unstable, which explains the absence of such ordered 2D islands.

In conclusion, the irregular coordination structure observed in the Polymeric phase (Figure 6.6a) can be understood as a result of the competition between different coordination pathways, in which the higher hierarchy of trimers over tetarmers, and specially over the unstable infinite 2D networks, blocks the formation of larger 2D networks (see Figure C.1 in Appendix C). Nevertheless, the fact that we did not observe coexistence between the Dimeric and the Polymeric phase (by STM) cannot be well explained with the thermodynamic picture given by the DFT calculations. One possible explanation rely on the number of accessible Te adatoms at a given reaction temperature. This could not be enough to promote the coordination of more than two monomers at the activation temperature of the Dimeric phase, while a higher concentration of available Te adatoms would allow extended coordination numbers (i.e. chains, trimers and tetramers) at the higher temperature where the Polymeric phase was found. Indeed, several studies pointed the crucial role of the stoichiometry between the coordination metal and the monomer in the resulting MO structure [260].

The formation of MO structures by the surface-assisted passivation of dehalogenated molecules is a well known phenomena in nobel metals. Dehalogenated radicals coordinate to metal adatoms that are either thermally or chemically extracted from the surface, forming different one and two dimensional structures.

These are often intermediates of more stable covalent structures [261, 262]. However, if the interactions with the substrate are weak, the final covalent structures can be inhibited by desorption [263]. In a similar way, the initial dehalogenation process can also be inhibited by desorption if the interaction is too weak. For instance, dehalogenation of bromophenylbenzene can be thermally activated in Cu(111) and Ag(110), but is desorption-inhibited in graphite(001) [243]. In our case we find that annealing above 250°C leads to complete desorption of the molecular structures before any additional phase is formed. Thus the Bi_2Te_3 surface reactivity is strong enough to induce dehalogenation and subsequent formation of Te-coordinated networks, but weak enough to transform these into covalent networks.

6.3 Electronic Properties of Te-coordinated Structures

A complete set of STS spectra and conductance maps were acquired in order to asses how the coordination with Te atoms affects the electronic structure of the CoTPP. A comparison between the unreacted CoTBrPP (already discussed extensively in Chapter 5) and the Te-coordinated CoTPP chain is presented below.

Figure 6.8a shows conductance (dI/dV) spectra taken on three representative molecular positions, schematically represented in models in the right side of the figure, of unreacted porphyrin (CoTBrPP, blue) and Te-coordinated porphyrin chain ($[Te_2\text{-CoTPP}]_n$, red) on Bi_2Te_3, together with conductance maps taken at representative energies. The first noticeable difference in the Te-coordinated case is the emergence of intense spherical protrusions at the coordination sites. They appear with strong intensity from -2.0 eV to 1.0 eV in the red conductance maps in Figure 6.8b-e, in contrast to the low spectral contribution emerging from the Br positions in the unreacted bromophenyls, which are visible only in energies within the molecular gap (blue map in Figure 6.8d).

The spectroscopic features that are more related to the CoTPP molecular unit appear with the same spatial distribution but shifted to lower energies by about $0.4 - 0.5$ eV. The onset of the HOMO, related to the $d_{xz/yz}$ orbital hybridized with pyrrole states, is found at -1.0 eV and -1.4 eV for the unreacted and Te-coordinated species respectively. The onset of the LUMO, a d_{z^2} related orbital, shifts from 1.7 eV to 1.2 eV upon coordination. A similar shift from 2.3 eV to 1.9 eV is observed for the ligand related manifold that shows intensity around the phenyl groups.

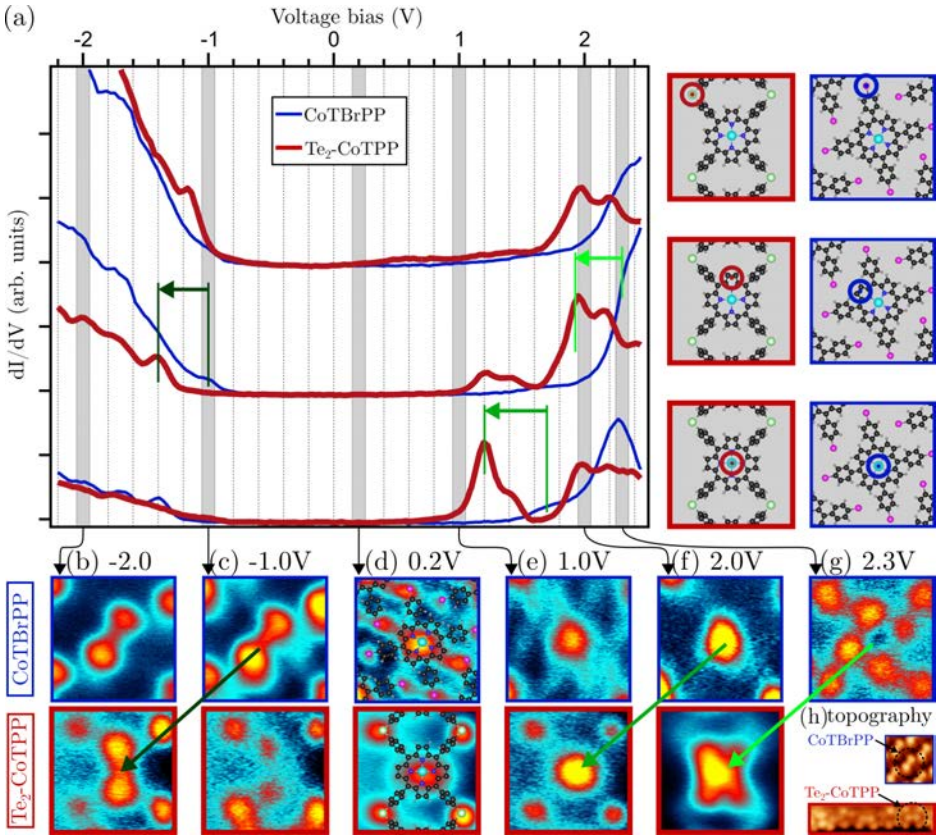

Figure 6.8: STS comparison between the electronic structure of the molecules on Bi_2Te_3 before (CoTBrPP in blue) and after the annealing-induced dehalogenation and Te-coordination ($[Te_2\text{-}CoTPP]_n$ in red) on Bi_2Te_3 surface. (a) Pairs of conductance dI/dV spectra, each one acquired on the spots depicted in the schematics on the right side of the figure. (b) - (g) Conductance dI/dV maps (2.3×2.3 nm^2) measured on at different bias voltages. Green arrows denote the energy shift that molecular orbitals undergo upon the reaction. (h) STM topographic images showing the unreacted and reacted molecules under study (blue: 4×4 nm^2 and $V_{bias} = -1.4$ V, red: 12×2.8 nm^2 and $V_{bias} = -1.5$ V).

Despite the concerted downwards energy shift of all molecular orbitals, none of them is crossing or even close to the Fermi Level (E_F), meaning that the molecule dos not receive (or give) any charge. The energy shifts then could be related to a different interaction with the substrate, or to an electrostatic field that could gate the molecular orbitals. The former is rather unlikely, given the fact that the interaction with the substrate of unreacted molecules is already weak, and further decoupling is expected for the out-of-registry coordinated molecules (as inferred from Figure C.2d in Appendix C). Indeed, a sharpening of the peaks can be observed in the spectra of the coordinated molecule, an indication of an increased decoupling. Coulomb shifts could arise, on the other hand, from the coordinated Te ions that act as local gating potentials. An additional hint

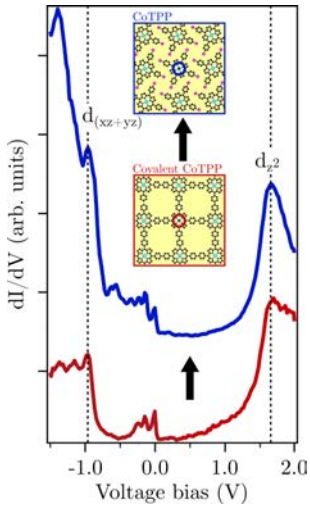

Figure 6.9: STS comparison between spectra taken in the molecular center of as-deposited CoTBrPP and covalently bonded CoTPP on Au(111) presenting not-shifted contribution from d orbitals.

pointing towards the Te atoms as origin of the shift lies in the fact that the purely covalent networks observed in Au(111) does not show any energy shift of the orbitals, as shown in Figure 6.9.

DFT calculations performed on the polymeric chain structures result in a donation of 0.46 electrons per Te atom. Being a gas-phase calculation, the electron can only be donated to the molecule. However, in the presence of a substrate, this can act as a charge sink, inhibiting the molecular charge transfer. This has indeed been observed in the Li doping of CuPc molecules deposited on Ag(100) [92]. Here the electron donated by the Li cation is absorbed by the metallic substrate reservoir, and the halogens, electrostitcally bonded to the molecule, act only as gating sources, shifting the orbitals without changing their occupation. We propose the same scenario for the Te-coordinated molecular system, where the Te cations shift the CoTPP molecular orbitals. Hence, this charge redistribution does not alter the d level occupation of the Co2+ cation and its S=1/2 character. Indeed, this is a robust result, since DFT calculations also show unaltered d orbitals in the PDOS in spite of the net charge that is redistributed in ligand orbitals.

6.4 Bi_2Te_3 Electronic Properties upon CoTBrPP Reaction

In order to assess if the Te-coordinated CoTPP structures alter the stability of the TSS, ARPES measurements were performed on the pristine Bi_2Te_3, after the deposition of CoTBrPP molecules and after annealing at 240°C, that is the temperature in which molecules are completely debrominated (see Figure 6.1). Data presented in this section was acquired in the same sample, different from those ones used in Sections 6.1 and 6.2. ARPES acquisitions were accompanied

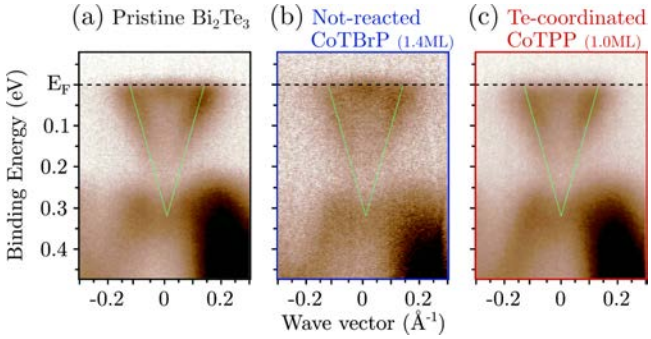

Figure 6.10: ARPES intensity maps taken along the $\Gamma \rightarrow$ M direction, showing the Bi_2Te_3 TSS of the (a) pristine surface, (b) after CoTBrPP deposition and (c) after subsequent annealing at 240°C. Molecular coverage calculated as in Appendix B.

by XPS measurements, confirming the compatibility between results found for the XPS and ARPES studies. The experiment was repeated in two different samples, finding consistent results.

ARPES intensity maps in Figure 6.10 measurements were performed on the pristine Bi_2Te_3, after the deposition of CoTBrPP at RT, and after annealing at 240°C, that is the temperature in which molecules are completely dehalogenated and form Te-coordinated phases. The results are presented in Figure 6.10, showing intense Dirac-like bands (Dirac cone, highlighted in green lines) characteristic of TSS for the three cases, and revealing the TSS prevalence when put in contact with a complete layer of Te-coordinated CoTPP molecules. Additionally, the Fermi level (dotted black line) is preserved in the bulk gap as no significant energy shift with respect to the pristine situation is observed. This is in contrast to most of the prior studies interfacing magnetic MO molecules with TIs, in which the helical surface states are strongly perturbed by a significant n-doping from the metal ions [216–219, 264], or even by quenching the TSS at the outermost Quintuple-layer (QL) of the TI [99]. Consequently the bulk remains insulating, thus limiting the current to a TSS that is in direct contact with the magnetic material.

6.5 Summary

On-surface synthesis of MO coordination structures on TI surface has been achieved for the first time, by using CoTBrPP as molecular precursor on Bi_2Te_3 surface. A selective formation of extended networks composed of dimers, formed by two CoTPP monomers coordinated via two Te atoms, is found at the temperature threshold of 200°C. At temperatures above 220°C, the dimeric phase evolves into large polymeric structures. Based on the higher stability of chain structures as compared to dimers obtained from DFT, we attribute this transition to the higher concentration of available Te adatoms at increasing temperatures. On the other hand, the lack of ordered 2D structures is explained by the instability of the 4-fold coordinated configuration, as calculated by DFT. We also find spectroscopic evidences that the orbital structure of the molecule remains unpertubed, and probably further decoupled from the TI.

Remarkably, the synthesis of such structures does not induce doping to the TI, thus preserving its bulk insulating behaviour, at the same time that maintains the TSS at the very interface. Interactions are therefore in the non-perturbative regime, allowing the independent engineering of the molecular and TI properties, crucial for the realization of the sought after spin-orbit phenomena emerging from TIs.

Chapter 7

Conclusions and Outlook

Bulk conductivity in TIs represent one of the major issues for the detection of surface currents, thus compromising the study of novel spin-related phenomena emerging from the helical surface currents. Therefore, the growth of TI materials with the Fermi Level positioned within the bulk gap is required. In the last years it has been achieved by using MBE growth method, as it offers a great control over impurities and crystalline defects, responsible of inducing doping effects and parasitic conducting channels in the bulk [56–60].

In Chapter 3, two complementary MBE approaches towards the growth of TI thin films with controlled position of the Fermi Level position by MBE are presented. The first one focusses on the improvement of crystalline quality, without the need of adding extrinsec dopants. The growth of high-crystalline quality Bi_2Te_3 thin films with suppressed mirror-symmetric twin domains, responsible for self-doping of the crystal [155], is discussed as a function of the substrate and growth temperature. Bi_2Te_3 thin films free of twin domains, and consequently with exceptional low-doping level, are achieved by a combination of the initial interaction with the BaF_2 substrate and the spiral-like growth mode favoured by high working temperatures [159].

The second approach exploits the MBE capability to chemically modify the pristine Bi_2Te_3 thin film. We report that the progressive addition of Sb as Te antisite during the growth process induces p-doping and shifts the Dirac point across the bulk gap. Adjusting the proper x concentration results into a $(Bi_{1-x}Sb_x)_2Te_3$ compound with E_F well located into the bulk gap. Such a p-doped character can counteract the typical n-doping effect induced when TIs are interfaced with other materials [63, 69, 71, 73, 265], defining a system where magnetic interactions between TSS and magnetic materials can be explored. The use of $(Bi_{1-x}Sb_x)_2Te_3$ in heterostructures has not been explored in this thesis, and remains for future investigations.

Interfacing TIs with magnetic materials can give rise to novel magnetoelectronic phenomena, the emergence of which depend crucially on the capability to control interactions occurring at the interface. Magnetic moments and anisotropies are often modified or quenched upon adsorption on surfaces, like-

wise the stability of TI helical surface states can be compromised when put in contact with certain materials. The results presented in this thesis provide an insight into the realization of such hybrid heterostructures with non-perturbative interactions, via the use of magnetic MO frameworks.

A rational design of organic ligands hosting magnetic ions give access to a large variety of electronic and spin states, and leads to great control over the interfacial interactions. The study presented in Chapter 4 illustrates how magnetic interactions can be finely tuned by caging a magnetic Co ion in different planar ligands on a model metallic surface such as Au(111). They are explored by complementary STS and XMCD techniques, that provide complementary electronic and magnetic information respectively. While CoPc leads to strong hybridization between Co d orbitals and substrate states that result in quenched magnetic moment, CoTPP, covalently bonded CoTPP and CoTBrPP gradually lift the Co ion, taking it into a scenario where its magnetic moment is gradually recovered. This is evidenced by the correlation between the strength of Kondo coupling between unpaired Co electrons and surface conduction electrons, the intensity of XMCD signal and the DFT calculated adsorption distance of each molecular ligand. Additionally, CoTBrPP deposited on TI Bi_2Te_3 surface, leads to an even weaker interacting interface in which the pristine magnetic moment is preserved.

This finding encourages further endeavours in order to assess the delicate stability of the TSS by employing ligand chemistry for tuning interactions, and to gain more insight into the complex magnetic / TI interfaces. Therefore, Chapter 5 presents a comprehensive study of CoTBrPP molecules on Bi_2Te_3 system, in which the structural, electronic and magnetic properties are explored with STM, STS/XPS/ARPES and XMCD respectively. The results indicate that TBrPP ligands enables the creation of an interface where both the magnetic moment of the Co ion and the TSS are unperturbed but still in direct contact. It is noteworthy to mention, that molecules do not induce extra electron-doping, vital for the preservation of truly bulk insulating TIs. Additionally, it is also reported that caging the Co ion in Pc ligands maintains the interfacial interactions in the non-perturbative regime, with just a slight increase in the TSS doping level. This contrasts with the CoPc suppression of the Bi_2Se_3 TSS reported in the literature [99], highlighting that changes in TI electronic structure can also affect dramatically the interfacial properties.

The inter-molecular interactions in the magnetic MO films studied to this point are dominated by weak vdW forces. In order to enhance the magnetic correlations between magnetic ions, coordination bonds between MO ligands were induced in Chapter 6. On-surface formation of covalent or coordination structures have been traditionally performed on metallic surfaces because of their high catalytic activity. Here, we achieve for the first time the on-TI surface synthesis of coordinated MO networks. Thanks to a combined XPS and STM study, we observe how a dehalogenation reaction occurs upon thermal activation, leading to the formation of coordination structures via the incorporation of Te atoms from the substrate. Two differentiated phases emerge at different temperatures; (i) formation of $[\text{Te-CoTPP}]_2$ dimers that condense in ordered arrays in which inter-dimeric interactions are driven by vdW forces; (ii) and formation of irregu-

lar structures comprising tens of ligands as a result of different Te coordination numbers. DFT calculations corroborate the stability of such structures, at the same time that assert that long-range 2D structures are not stable. Overall, the formation of the Te-coordinated structures is fairly well understood by a simple picture based only on thermodynamic considerations, regardless more complex dynamic and chemical process that may occur on the surface during the reaction. Additionally, ARPES measurements reveal that the Bi_2Te_3 TSS is kept unperturbed and undoped upon the formation of coordination MO structures.

Previous studies had shown that the use of MO molecules on TI could to cover the full range of magnetic interactions; from weak dipolar by using non-planar molecules where the magnetic ion is far from the surface protected by a 3D ligand shell [220], to strong interactions where the TSS is highly perturbed [99]. On the other hand, our results indicate that ligand chemistry can be used to fine-tune interactions within the non-perturbative regime, yet using planar molecules where the ion is in direct contact with the surface. Nevertheless, the induction of magnetic order with an out-of-plane component, required for the emergence of QAHE has not been achieved.

Therefore, several pathways continuing this line of research can be proposed, with special aim to enhance the magnetic order within the molecular layer. Reducing the lateral size of the ligands that act as molecular building blocks in correlated networks appears as a good strategy to enhance magnetic interactions between magnetic ions. Among other factors to consider, this would enhance exchange interactions, enabling long-range magnetically ordered networks. As an example, covalent bonding of a 2D Cr-polyporphirin network is predicted to mediate ferromagnetic order between Cr- magnetic moments via magnetic exchange, with a surprisingly elevated Curie temperature of 183 K [266]. Nevertheless, metal-coordinated organic networks seem to be the most suitable candidates for driving long-range magnetic order [97, 100–102]. The reversible nature of the coordination bonds make the on-surface formation of such structures tolerant against defect formation, thus more prompt to generate structures with long-range structural order [267]. In particular, MO coordination networks containing lanthanide ions are very promising because of their large spin moments and anisotropy of the lattests [268].

Another pathway worth exploring is the mediation of magnetic order by the Dirac surface electrons [269, 270] via the Ruderman-Kittle-Kasuya-Yosida (RKKY) coupling. Two factors affect crytically the sign and magnitude of the RKKY coupling: First, the distance between magnetic moments [213, 271], which can lead to cancellation between ferromagnetic and anti-ferromagnetic interactions in the case of disordered systems. And second, the Dirac fermions wavelength at E_F ($\lambda_F = 1/k_F$), which is often uncontrolled due to the tendency of magnetic impurities to electron-dope (hence modifying k_F) [74, 212]. In this thesis we have shown that MO molecules present the tools to overcome this issues: First, the spatial long-range order between magnetic ions, that could promote the same RKKY interaction among all ions. And second, the fact that they can be directly exposed to TSS while keeping the electronic doping level unaltered.

Overall, these findings represent an important step in the understanding of

the electronic and magnetic interactions between magnetic ions, caged in vdW interacting and coordinated molecular frameworks, with TI surfaces. The reported heterostructures define a benchmark scenario where the magnetic and topological properties can be engineered independently , thus encouraging future endeavours towards the induction of magnetic order in the TIs.

Bibliography

[1] Ibach, H. *Springer*; Springer-Verlag Berlin Heidelberg: Jülich, Germany, 2006.

[2] Lüth, H. *Solid Surfaces, Interfaces and Thin Films*; Graduate Texts in Physics; Springer Berlin Heidelberg: Berlin, Germany, 2010.

[3] Ohtomo, A.; Hwang, H. Y. A high-mobility electron gas at the $LaAlO_3/SrTiO_3$ heterointerface. *Nature* **2004**, *427*, 423–426.

[4] Gariglio, S.; Reyren, N.; Caviglia, A. D.; Triscone, J.-M. Superconductivity at the $LaAlO_3$ /$SrTiO_3$ interface. *Journal of Physics: Condensed Matter* **2009**, *21*, 164213.

[5] Bert, J. A.; Kalisky, B.; Bell, C.; Kim, M.; Hikita, Y.; Hwang, H. Y.; Moler, K. A. Direct imaging of the coexistence of ferromagnetism and superconductivity at the LaAlO3/SrTiO3 interface. *Nature Physics* **2011**, *7*, 767–771.

[6] Shalom, M. B.; Sachs, M.; Rakhmilevitch, D.; Palevski, A.; Dagan, Y. Tuning spin-orbit coupling and superconductivity at the $SrTiO_3/LaAlO_3$ interface: a magneto-transport study. *Physical Review Letters* **2010**, *104*, 126802.

[7] Tebano, A.; Fabbri, E.; Pergolesi, D.; Balestrino, G.; Traversa, E. Room-Temperature Giant Persistent Photoconductivity in $SrTiO_3/LaAlO_3$ Heterostructures. *ACS Nano* **2012**, *6*, 1278–1283.

[8] Bogorin, D. F.; Irvin, P.; Cen, C.; Levy, J. *Multifunctional Oxide Heterostructures*; Oxford University Press, 2012; pp 364–388.

[9] Brown, G. E. In *Selected Papers, with Commentary, of Tony Hilton Royle Skyrme*; E. Brown, G., Ed.; World Scientific Series in 20th Century Physics; WORLD SCIENTIFIC: Singapore, 1994; Vol. 3.

[10] Fu, L. Topological Crystalline Insulators. *Physical Review Letters* **2011**, *106*, 106802.

[11] Murakami, S. Phase transition between the quantum spin Hall and insulator phases in 3D: emergence of a topological gapless phase. *New Journal of Physics* **2007**, *9*, 356–356.

[12] Topological phase transitions and topological phases of matter. 2016; `https://www.nobelprize.org/prizes/physics/2016/press-release/`.

[13] Ando, Y. Topological insulator materials. *Journal of the Physical Society of Japan* **2013**, *82*, 1–32.

[14] Ortmann, F.; Roche, S.; Valenzuela, S. O. *Topological Insulators*; Wiley-VCH Verlag GmbH & Co. KGaA: Weinheim, Germany, 2015; Vol. 63; pp 1–10.

[15] Kane, C. L.; Mele, E. J. Z2 Topological Order and the Quantum Spin Hall Effect. *Physical Review Letters* **2005**, *95*, 146802.

[16] Bernevig, B. A.; Zhang, S.-C. Quantum Spin Hall Effect. *Physical Review Letters* **2006**, *96*, 106802.

[17] Haldane, F. Model for a Quantum Hall Effect without Landau Levels: Condensed-Matter Realization of the "Parity Anomaly". *Physical Review Letters* **1988**, *61*, 2015–2018.

[18] Bernevig, B. A.; Hughes, T. L.; Zhang, S.-C. Quantum Spin Hall Effect and Topological Phase Transition in HgTe Quantum Wells. *Science* **2006**, *314*, 1757–1761.

[19] Konig, M.; Wiedmann, S.; Brune, C.; Roth, A.; Buhmann, H.; Molenkamp, L. W.; Qi, X.-L.; Zhang, S.-C. Quantum Spin Hall Insulator State in HgTe Quantum Wells. *Science* **2007**, *318*, 766–770.

[20] Kou, L.; Ma, Y.; Sun, Z.; Heine, T.; Chen, C. Two-Dimensional Topological Insulators: Progress and Prospects. *The Journal of Physical Chemistry Letters* **2017**, *8*, 1905–1919.

[21] Fu, L.; Kane, C. L.; Mele, E. J. Topological Insulators in Three Dimensions. *Physical Review Letters* **2007**, *98*, 106803.

[22] Xia, Y.; Qian, D.; Hsieh, D.; Wray, L.; Pal, A.; Lin, H.; Bansil, A.; Grauer, D.; Hor, Y. S.; Cava, R. J.; Hasan, M. Z. Observation of a large-gap topological-insulator class with a single Dirac cone on the surface. *Nature Physics* **2009**, *5*, 398–402.

[23] Hsieh, D.; Qian, D.; Wray, L.; Xia, Y.; Hor, Y. S.; Cava, R. J.; Hasan, M. Z. A topological Dirac insulator in a quantum spin Hall phase. *Nature* **2008**, *452*, 970–974.

[24] Zhang, H.; Liu, C.-X.; Qi, X.-L.; Dai, X.; Fang, Z.; Zhang, S.-C. Topological insulators in Bi_2Se_3, Bi_2Te_3 and Sb_2Te_3 with a single Dirac cone on the surface. *Nature Physics* **2009**, *5*, 438–442.

[25] Hu, X.; Zhong, Z.; Fiete, G. A. First Principles Prediction of Topological Phases in Thin Films of Pyrochlore Iridates. *Scientific Reports* **2015**, *5*, 11072.

[26] Liang, Y.; Khazaei, M.; Ranjbar, A.; Arai, M.; Yunoki, S.; Kawazoe, Y.; Weng, H.; Fang, Z. Theoretical prediction of two-dimensional functionalized MXene nitrides as topological insulators. *Physical Review B* **2017**, *96*, 195414.

[27] Pi, S.-T.; Wang, H.; Kim, J.; Wu, R.; Wang, Y.-K.; Lu, C.-K. New Class of 3D Topological Insulator in Double Perovskite. *The Journal of Physical Chemistry Letters* **2017**, *8*, 332–339.

[28] Dey, U.; Chakraborty, M.; Taraphder, A.; Tewari, S. Bulk band inversion and surface Dirac cones in LaSb and LaBi: Prediction of a new topological heterostructure. *Scientific Reports* **2018**, *8*, 14867.

[29] Zhang, D.; Wang, J.; Dasilva, A. M.; Lee, J. S.; Gutierrez, H. R.; Chan, M. H.; Jain, J.; Samarth, N. Superconducting proximity effect and possible evidence for Pearl vortices in a candidate topological insulator. *Physical Review B - Condensed Matter and Materials Physics* **2011**, *84*, 1–8.

[30] Sochnikov, I.; Bestwick, A. J.; Williams, J. R.; Lippman, T. M.; Fisher, I. R.; Goldhaber-Gordon, D.; Kirtley, J. R.; Moler, K. A. Direct measurement of current-phase relations in superconductor/topological insulator/superconductor junctions. *Nano Letters* **2013**, *13*, 3086–3092.

[31] Williams, J. R.; Bestwick, A. J.; Gallagher, P.; Hong, S. S.; Cui, Y.; Bleich, A. S.; Analytis, J. G.; Fisher, I. R.; Goldhaber-Gordon, D. Unconventional Josephson effect in hybrid superconductor-topological insulator devices. *Physical Review Letters* **2012**, *109*, 1–5.

[32] Cho, S.; Dellabetta, B.; Yang, A.; Schneeloch, J.; Xu, Z.; Valla, T.; Gu, G.; Gilbert, M. J.; Mason, N. Symmetry protected Josephson supercurrents in three-dimensional topological insulators. *Nature communications* **2013**, *4*, 1689.

[33] Majorana, E.; Maiani, L. *Società Italiana di Fisica*; Springer Berlin Heidelberg: Berlin, Heidelberg, 1981; Vol. 63; pp 201–233.

[34] Wilczek, F. Majorana returns. *Nature Physics* **2009**, *5*, 614–618.

[35] Fu, L.; Kane, C. L. Superconducting proximity effect and majorana fermions at the surface of a topological insulator. *Physical Review Letters* **2008**, *100*, 1–4.

[36] Sun, H.-H.; Jia, J.-F. Majorana zero mode in the vortex of an artificial topological superconductor. *Science China Physics, Mechanics & Astronomy* **2017**, *60*, 057401.

[37] Fert, A. Origin, Development, and Future of Spintronics (Nobel Lecture). *Angewandte Chemie International Edition* **2008**, *47*, 5956–5967.

[38] Han, W. Perspectives for spintronics in 2D materials. *APL Materials* **2016**, *4*, 032401.

[39] Sander, D. et al. The 2017 Magnetism Roadmap. *Journal of Physics D: Applied Physics* **2017**, *50*, 363001.

[40] Edelstein, V. Spin polarization of conduction electrons induced by electric current in two-dimensional asymmetric electron systems. *Solid State Communications* **1990**, *73*, 233–235.

[41] Wang, Y.; Zhu, D.; Wu, Y.; Yang, Y.; Yu, J.; Ramaswamy, R.; Mishra, R.; Shi, S.; Elyasi, M.; Teo, K.-L.; Wu, Y.; Yang, H. Room temperature magnetization switching in topological insulator-ferromagnet heterostructures by spin-orbit torques. *Nature Communications* **2017**, *8*, 6–11.

[42] DC, M.; Grassi, R.; Chen, J.-Y.; Jamali, M.; Reifsnyder Hickey, D.; Zhang, D.; Zhao, Z.; Li, H.; Quarterman, P.; Lv, Y.; Li, M.; Manchon, A.; Mkhoyan, K. A.; Low, T.; Wang, J.-P. Room-temperature high spin–orbit torque due to quantum confinement in sputtered BixSe(1–x) films. *Nature Materials* **2018**, *17*, 800–807.

[43] Rojas-Sánchez, J. C.; Oyarzún, S.; Fu, Y.; Marty, A.; Vergnaud, C.; Gambarelli, S.; Vila, L.; Jamet, M.; Ohtsubo, Y.; Taleb-Ibrahimi, A.; Le Fèvre, P.; Bertran, F.; Reyren, N.; George, J. M.; Fert, A. Spin to Charge Conversion at Room Temperature by Spin Pumping into a New Type of Topological Insulator: α -Sn Films. *Physical Review Letters* **2016**, *116*, 1–6.

[44] He, K.; Wang, Y.; Xue, Q.-K. Quantum anomalous Hall effect. *National Science Review* **2013**, *1*, 38–48.

[45] Chang, C. C.-Z. et al. Experimental Observation of the Quantum Anomalous Hall Effect in a Magnetic Topological Insulator. *Science* **2013**, *340*, 167–170.

[46] Qi, X.-L.; Hughes, T. L.; Zhang, S.-C. Topological field theory of time-reversal invariant insulators. *Physical Review B* **2008**, *78*, 195424.

[47] Yu, R.; Zhang, W.; Zhang, H.-J.; Zhang, S.-C.; Dai, X.; Fang, Z. Quantized Anomalous Hall Effect in Magnetic Topological Insulators. *Science* **2010**, *329*, 61–64.

[48] Liu, C.-X.; Qi, X.-L.; Dai, X.; Fang, Z.; Zhang, S.-C. Quantum Anomalous Hall Effect in Hg$_{1-y}$Mn$_{y}$Te Quantum Wells. *Physical Review Letters* **2008**, *101*, 146802.

[49] Zhang, X.; Zhang, S.-C. Chiral interconnects based on topological insulators. 2012; p 837309.

[50] Wang, J.; Lian, B.; Zhang, H.; Xu, Y.; Zhang, S.-C. Quantum Anomalous Hall Effect with Higher Plateaus. *Physical Review Letters* **2013**, *111*, 136801.

[51] Stern, A.; Lindner, N. H. Topological Quantum Computation–From Basic Concepts to First Experiments. *Science* **2013**, *339*, 1179–1184.

[52] Paglione, J.; Butch P., N. *Topological Insulators*; Wiley-VCH Verlag GmbH & Co. KGaA: Weinheim, Germany, 2015.

[53] Hsieh, D. et al. A tunable topological insulator in the spin helical Dirac transport regime. *Nature* **2009**, *460*, 1101–1105.

[54] Hor, Y. S.; Roushan, P.; Beidenkopf, H.; Seo, J.; Qu, D.; Checkelsky, J. G.; Wray, L. A.; Hsieh, D.; Xia, Y.; Xu, S.-Y.; Qian, D.; Hasan, M. Z.; Ong, N. P.; Yazdani, A.; Cava, R. J. Development of ferromagnetism in the doped topological insulator $Bi_{2-x}Mn_xTe_3$. *Physical Review B* **2010**, *81*, 195203.

[55] Chen, Y. L.; Analytis, J. G.; Chu, J.-H.; Liu, Z. K.; Mo, S.-K.; Qi, X. L.; Zhang, H. J.; Lu, D. H.; Dai, X.; Fang, Z.; Zhang, S. C.; Fisher, I. R.; Hussain, Z.; Shen, Z.-X. Experimental Realization of a Three-Dimensional Topological Insulator, Bi_2Te_3. *Science* **2009**, *325*, 178–181.

[56] Li, Y.-Y. et al. Intrinsic Topological Insulator Bi_2Te_3 Thin Films on Si and Their Thickness Limit. *Advanced Materials* **2010**, *22*, 4002–4007.

[57] Chen, X.; Ma, X.-C.; He, K.; Jia, J.-F.; Xue, Q.-K. Molecular Beam Epitaxial Growth of Topological Insulators. *Advanced Materials* **2011**, *23*, 1162–1165.

[58] Zhang, J.; Chang, C.-Z.; Zhang, Z.; Wen, J.; Feng, X.; Li, K.; Liu, M.; He, K.; Wang, L.; Chen, X.; Xue, Q.-K.; Ma, X.; Wang, Y. Band structure engineering in $(Bi_{1-x}Sb_x)_2Te_3$ ternary topological insulators. *Nature Communications* **2011**, *2*, 574.

[59] Lee, J. J.; Schmitt, F. T.; Moore, R. G.; Vishik, I. M.; Ma, Y.; Shen, Z. X. Intrinsic ultrathin topological insulators grown via molecular beam epitaxy characterized by in-situ angle resolved photoemission spectroscopy. *Applied Physics Letters* **2012**, *101*, 013118.

[60] Ngabonziza, P.; Heimbuch, R.; De Jong, N.; Klaassen, R. A.; Stehno, M. P.; Snelder, M.; Solmaz, A.; Ramankutty, S. V.; Frantzeskakis, E.; Van Heumen, E.; Koster, G.; Golden, M. S.; Zandvliet, H. J.; Brinkman, A. In situ spectroscopy of intrinsic Bi_2Te_3topological insulator thin films and impact of extrinsic defects. *Physical Review B - Condensed Matter and Materials Physics* **2015**, *92*, 1–7.

[61] Li, C. H.; van 't Erve, O. M. J.; Robinson, J. T.; Liu, Y.; Li, L.; Jonker, B. T. Electrical detection of charge-current-induced spin polarization due to spin-momentum locking in Bi_2Se_3. *Nature Nanotechnology* **2014**, *9*, 218–224.

[62] Li, J.; Wang, Z. Y.; Tan, A.; Glans, P.-A.; Arenholz, E.; Hwang, C.; Shi, J.; Qiu, Z. Q. Magnetic dead layer at the interface between a Co film and the topological insulator Bi2Se3. *Physical Review B* **2012**, *86*, 054430.

[63] Spataru, C. D.; Léonard, F. Fermi-level pinning, charge transfer, and relaxation of spin-momentum locking at metal contacts to topological insulators. *Physical Review B* **2014**, *90*, 085115.

[64] Ye, W. Band bending at interfaces between topological insulator Bi2Se3 and transition metals Weiguang. *arXiv* **2015**,

[65] De Jong, N.; Frantzeskakis, E.; Zwartsenberg, B.; Huang, Y. K.; Wu, D.; Hlawenka, P.; Sańchez-Barriga, J.; Varykhalov, A.; Van Heumen, E.; Golden, M. S. Angle-resolved and core-level photoemission study of interfacing the topological insulator $Bi_1.5Sb_0.5Te_1.7Se_1.3$ with Ag, Nb, and Fe. *Physical Review B - Condensed Matter and Materials Physics* **2015**, *92*, 1–10.

[66] Zhang, J.; Velev, J. P.; Dang, X.; Tsymbal, E. Y. Band structure and spin texture of Bi_2Se_3 3d ferromagnetic metal interface. *Physical Review B* **2016**, *94*, 014435.

[67] Walsh, L. A.; Smyth, C. M.; Barton, A. T.; Wang, Q.; Che, Z.; Yue, R.; Kim, J.; Kim, M. J.; Wallace, R. M.; Hinkle, C. L. Interface Chemistry of Contact Metals and Ferromagnets on the Topological Insulator Bi_2Se_3. *The Journal of Physical Chemistry C* **2017**, *121*, 23551–23563.

[68] Ye, M. et al. Perpendicular magnetic anisotropy with enhanced orbital moments of Fe adatoms on a topological surface of Bi 2 Se 3. *Journal of Physics: Condensed Matter* **2013**, *25*, 232201.

[69] Schlenk, T.; Bianchi, M.; Koleini, M.; Eich, A.; Pietzsch, O.; Wehling, T. O.; Frauenheim, T.; Balatsky, A.; Mi, J. L.; Iversen, B. B.; Wiebe, J.; Khajetoorians, A. A.; Hofmann, P.; Wiesendanger, R. Controllable magnetic doping of the surface state of a topological insulator. *Physical Review Letters* **2013**, *110*, 1–5.

[70] Song, C. L.; Jiang, Y. P.; Wang, Y. L.; Li, Z.; Wang, L.; He, K.; Chen, X.; Ma, X. C.; Xue, Q. K. Gating the charge state of single Fe dopants in the topological insulator Bi 2Se 3 with a scanning tunneling microscope. *Physical Review B - Condensed Matter and Materials Physics* **2012**, *86*, 3–6.

[71] Eelbo, T.; Waśniowska, M.; Sikora, M.; Dobrzański, M.; Kozłowski, A.; Pulkin, A.; Autès, G.; Miotkowski, I.; Yazyev, O. V.; Wiesendanger, R. Strong out-of-plane magnetic anisotropy of Fe adatoms on Bi2Te3. *Phys. Rev. B - Condens. Matter Mater. Phys.* **2014**, *89*, 1–6.

[72] Honolka, J.; Khajetoorians, A. A.; Sessi, V.; Wehling, T. O.; Stepanow, S.; Mi, J.-L.; Iversen, B. B.; Schlenk, T.; Wiebe, J.; Brookes, N. B.; Lichtenstein, A. I.; Hofmann, P.; Kern, K.; Wiesendanger, R. In-Plane Magnetic Anisotropy of Fe Atoms on Fe Atoms on bi2Se3(111). *Physical Review Letters* **2012**, *108*, 256811.

[73] Martínez-Velarte, M. C.; Kretz, B.; Moro-Lagares, M.; Aguirre, M. H.; Riedemann, T. M.; Lograsso, T. A.; Morellón, L.; Ibarra, M. R.; Garcia-Lekue, A.; Serrate, D. Chemical Disorder in Topological Insulators: A Route to Magnetism Tolerant Topological Surface States. *Nano Letters* **2017**, *17*, 4047–4054.

[74] Sessi, P.; Reis, F.; Bathon, T.; Kokh, K. A.; Tereshchenko, O. E.; Bode, M. Signatures of Dirac fermion-mediated magnetic order. *Nature Communications* **2014**, *5*, 1–8.

[75] Scholz, M. R.; Sánchez-Barriga, J.; Marchenko, D.; Varykhalov, A.; Volykhov, A.; Yashina, L. V.; Rader, O. Tolerance of Topological Surface States towards Magnetic Moments: Fe on Bi2Se3. *Physical Review Letters* **2012**, *108*, 256810.

[76] Wang, E.; Tang, P.; Wan, G.; Fedorov, A. V.; Miotkowski, I.; Chen, Y. P.; Duan, W.; Zhou, S. Robust Gapless Surface State and Rashba-Splitting Bands upon Surface Deposition of Magnetic Cr on Bi 2 Se 3. *Nano Lett.* **2015**, 150302112213008.

[77] Suto, K.; Yoshimoto, S.; Itaya, K. Two-Dimensional Self-Organization of Phthalocyanine and Porphyrin: Dependence on the Crystallographic Orientation of Au. *Journal of the American Chemical Society* **2003**, *125*, 14976–14977.

[78] Heim, D.; Écija, D.; Seufert, K.; Auwärter, W.; Aurisicchio, C.; Fabbro, C.; Bonifazi, D.; Barth, J. V. Self-Assembly of Flexible One-Dimensional Coordination Polymers on Metal Surfaces. *Journal of the American Chemical Society* **2010**, *132*, 6783–6790.

[79] Wäckerlin, C.; Chylarecka, D.; Kleibert, A.; Müller, K.; Iacovita, C.; Nolting, F.; Jung, T. A.; Ballav, N. Controlling spins in adsorbed molecules by a chemical switch. *Nature Communications* **2010**, *1*, 1–7.

[80] Ikeda, T.; Tsutsumi, O. Optical Switching and Image Storage by Means of Azobenzene Liquid-Crystal Films. *Science* **1995**, *268*, 1873–1875.

[81] Henzl, J.; Mehlhorn, M.; Gawronski, H.; Rieder, K. H.; Morgenstern, K. Reversible cis-trans isomerization of a single azobenzene molecule. *Angewandte Chemie - International Edition* **2006**, *45*, 603–606.

[82] Grill, L.; Dyer, M.; Lafferentz, L.; Persson, M.; Peters, M. V.; Hecht, S. Nano-architectures by covalent assembly of molecular building blocks. *Nature nanotechnology* **2007**, *2*, 687–691.

[83] Cinchetti, M.; Dediu, V. A.; Hueso, L. E. Activating the molecular spinterface. *Nature Materials* **2017**, *16*, 507–515.

[84] Liu, J.; Lewis, L. N.; Duggal, A. R. Photoactivated and patternable charge transport materials and their use in organic light-emitting devices. *Applied Physics Letters* **2007**, *90*, 233503.

[85] Shtein, M.; Mapel, J.; Benziger, J. B.; Forrest, S. R. Effects of film morphology and gate dielectric surface preparation on the electrical characteristics of organic-vapor-phase-deposited pentacene thin-film transistors. *Applied Physics Letters* **2002**, *81*, 268–270.

[86] Torsi, L.; Dodabalapur, A.; Sabbatini, L.; Zambonin, P. Multi-parameter gas sensors based on organic thin-film-transistors. *Sensors and Actuators B: Chemical* **2000**, *67*, 312–316.

[87] Majumder, M.; Sheath, P.; Mardel, J. I.; Harvey, T. G.; Thornton, A. W.; Gonzago, A.; Kennedy, D. F.; Madsen, I.; Taylor, J. W.; Turner, D. R.; Hill, M. R. Aqueous Molecular Sieving and Strong Gas Adsorption in Highly Porous MOFs with a Facile Synthesis. *Chemistry of Materials* **2012**, *24*, 4647–4652.

[88] Peumans, P.; Forrest, S. R. Very-high-efficiency double-heterostructure copper phthalocyanine/C60 photovoltaic cells. *Applied Physics Letters* **2001**, *79*, 126–128.

[89] Barth, J. V. Molecular architectonic on metal surfaces. *Annual review of physical chemistry* **2007**, *58*, 375–407.

[90] Mugarza, A.; Krull, C.; Robles, R.; Stepanow, S.; Ceballos, G.; Gambardella, P. Spin coupling and relaxation inside molecule–metal contacts. *Nature Communications* **2011**, *2*, 490.

[91] Auwärter, W.; Seufert, K.; Klappenberger, F.; Reichert, J.; Weber-Bargioni, A.; Verdini, A.; Cvetko, D.; Dell'Angela, M.; Floreano, L.; Cossaro, A.; Bavdek, G.; Morgante, A.; Seitsonen, A. P.; Barth, J. V. Site-specific electronic and geometric interface structure of Co-tetraphenyl-porphyrin layers on Ag(111). *Physical Review B - Condensed Matter and Materials Physics* **2010**, *81*, 1–14.

[92] Krull, C.; Robles, R.; Mugarza, A.; Gambardella, P. Site- and orbital-dependent charge donation and spin manipulation in electron-doped metal phthalocyanines. *Nat. Mater.* **2013**, *12*, 337–343.

[93] Lodi Rizzini, A. et al. Coupling of single, double, and triple-decker metal-phthalocyanine complexes to ferromagnetic and antiferromagnetic substrates. *Surface Science* **2014**, *630*, 361–374.

[94] Mugarza, A.; Robles, R.; Krull, C.; Korytár, R.; Lorente, N.; Gambardella, P. Electronic and magnetic properties of molecule-metal interfaces: Transition-metal phthalocyanines adsorbed on Ag(100). *Physical Review B* **2012**, *85*, 155437.

[95] Stepanow, S.; Lodi Rizzini, A.; Krull, C.; Kavich, J.; Cezar, J. C.; Yakhou-Harris, F.; Sheverdyaeva, P. M.; Moras, P.; Carbone, C.; Ceballos, G.; Mugarza, A.; Gambardella, P. Spin tuning of electron-doped metal-phthalocyanine layers. *Journal of the American Chemical Society* **2014**, *136*, 5451–5459.

[96] Wäckerlin, C.; Tarafder, K.; Siewert, D.; Girovsky, J.; Hählen, T.; Iacovita, C.; Kleibert, A.; Nolting, F.; Jung, T. A.; Oppeneer, P. M.; Ballav, N. On-surface coordination chemistry of planar molecular spin systems: novel magnetochemical effects induced by axial ligands. *Chemical Science* **2012**, *3*, 3154.

[97] Otrokov, M. M.; Chulkov, E. V.; Arnau, A. Breaking time-reversal symmetry at the topological insulator surface by metal-organic coordination networks. *Physical Review B* **2015**, *92*, 165309.

[98] Bathon, T.; Sessi, P.; Kokh, K. A.; Tereshchenko, O. E.; Bode, M. Systematics of Molecular Self-Assembled Networks at Topological Insulators Surfaces. *Nano Letters* **2015**, *15*, 2442–2447.

[99] Caputo, M. et al. Manipulating the Topological Interface by Molecular Adsorbates: Adsorption of Co-Phthalocyanine on Bi 2 Se 3. *Nano Letters* **2016**, *16*, 3409–3414.

[100] Umbach, T. R.; Bernien, M.; Hermanns, C. F.; Krüger, A.; Sessi, V.; Fernandez-Torrente, I.; Stoll, P.; Pascual, J. I.; Franke, K. J.; Kuch, W. Ferromagnetic coupling of mononuclear Fe centers in a self-assembled metal-organic network on Au(111). *Physical Review Letters* **2012**, *109*, 1–5.

[101] Abdurakhmanova, N.; Tseng, T. C.; Langner, A.; Kley, C. S.; Sessi, V.; Stepanow, S.; Kern, K. Superexchange-mediated ferromagnetic coupling in two-dimensional Ni-TCNQ networks on metal surfaces. *Physical Review Letters* **2013**, *110*, 1–5.

[102] Faraggi, M. N.; Golovach, V. N.; Stepanow, S.; Tseng, T.-C.; Abdurakhmanova, N.; Kley, C. S.; Langner, A.; Sessi, V.; Kern, K.; Arnau, A. Modeling Ferro- and Antiferromagnetic Interactions in Metal–Organic Coordination Networks. *The Journal of Physical Chemistry C* **2015**, *119*, 547–555.

[103] Cho, A. Y.; Arthur, J. R. Molecular beam epitaxy. *Molecular Beam Epitaxy* **1975**, *10*, 1–4157–1916.

[104] Bauer, E. Phänomenologische Theorie der Kristallabscheidung an Oberflächen. I. *Zeitschrift für Kristallographie* **1958**, *110*, 372–394.

[105] Koma, A.; Sunouchi, K.; Miyajima, T. Fabrication and characterization of heterostructures with subnanometer thickness. *Microelectronic Engineering* **1984**, *2*, 129–136.

[106] Binning, G.; Rohrer, H. "Scanning tunneling microscopy". IBM Journal of Research and Development. *IBM Journal of Research and Development* **1989**, *30*, 355.

[107] Bardeen, J. Tunnelling from a Many-Particle Point of View. *Physical Review Letters* **1961**, *6*, 57–59.

[108] Tersoff, J.; Hamann, D. R. Theory of the scanning tunneling microscope. *Physical Review B* **1985**, *31*, 805–813.

[109] Lang, N. D. Spectroscopy of single atoms in the scanning tunneling microscope. *Phys. Rev. B* **1986**, *34*, 2–5.

[110] Selloni, A.; Carnevali, P.; Tosatti, E.; Chen, C. D. Voltage-dependent scanning-tunneling microscopy of a crystal surface: Graphite. *Physical Review B* **1985**, *31*, 2602–2605.

[111] Ukraintsev, V. A. Data evaluation technique for electron-tunneling spectroscopy. *Physical Review B - Condensed Matter and Materials Physics* **1996**, *53*, 11176–11185.

[112] CreaTec Fischer and Co. GmbH. "STM/AFM systems". `http://www.createc.de/products/It-stm-afm-systems.html`.

[113] Meyer, G. A simple low-temperature ultrahigh-vacuum scanning tunneling microscope capable of atomic manipulation. *Review of Scientific Instruments* **1996**, *67*, 2960–2965.

[114] Hertz, H. Ueber einen Einfluss des ultravioletten Lichtes auf die electrische Entladung. *Annalen der Physik* **1887**, *2567*, 983–1000.

[115] Einstein, A. Concerning an Heuristic Point of View Toward the Emission and Transformation of Light. *Annalen der Physik* **1905**, *17*, 132–148.

[116] Arons, A. B.; Peppard, M. B. Einstein's Proposal of the Photon Concept—a Translation of the Annalen der Physik Paper of 1905. *American Journal of Physics* **1965**, *33*, 367–374.

[117] Fahlman, A.; Nordling, C.; Siegbahn, K. *ESCA: atomic, molecular and solid state structure studied by means of electron spectroscopy*; Almqvist and Wiksell: Uppsala, 1967.

[118] Seah, M. P.; Dench, W. A. Quantitative electron spectroscopy of surfaces: A standard data base for electron inelastic mean free paths in solids. *Surface and Interface Analysis* **1979**, *1*, 2–11.

[119] Hüfner, S. *Photoelectron Spectroscopy*; Springer-Verlag: Berlin Heidelberg, 1995.

[120] Bennett, H. S.; Stern, E. A. Faraday Effect in Solids. *Physical Review* **1965**, *137*, A448–A461.

[121] Erskine, J. L.; Stern, E. A. Calculation of the M2,3 magneto-optical absorption spectrum of ferromagnetic nickel. *Physical Review B* **1975**, *12*, 5016–5024.

[122] Laan, G. V. D.; Thole, B. T.; Sawatzky, G. A.; Laboratories, B.; Hill, M.; Dabkowska, H. A. Experimental proof of magnetic x-ray dichroism. **1986**, *34*, 2–4.

[123] Schnohr, C. S.; Ridgway, M. C. In *X-Ray Absorption Spectroscopy of Semiconductors*; Schnohr, C. S., Ridgway, M. C., Eds.; Springer Series in Optical Sciences; Springer Berlin Heidelberg: Berlin, Heidelberg, 2015; Vol. 190.

[124] Stohr, J.; Nakajima, R. Magnetic properties of transition-metal multilayers studied with X-ray magnetic circular dichroism spectroscopy. *IBM Journal of Research and Development* **1998**, *42*, 73–88.

[125] Fano, Spin Orientation of Photoelectrons Emitted by Circularly Polarized Light. *Physical Review* **1969**, *178*, 131.

[126] Barla, A.; Nicolás, J.; Cocco, D.; Valvidares, S. M.; Herrero-Martín, J.; Gargiani, P.; Moldes, J.; Ruget, C.; Pellegrin, E.; Ferrer, S. Design and performance of BOREAS, the beamline for resonant X-ray absorption and scattering experiments at the ALBA synchrotron light source. *Journal of Synchrotron Radiation* **2016**, *23*, 1507–1517.

[127] Krumrain, J.; Mussler, G.; Borisova, S.; Stoica, T.; Plucinski, L.; Schneider, C.; Grützmacher, D. MBE growth optimization of topological insulator Bi2Te3 films. *Journal of Crystal Growth* **2011**, *324*, 115–118.

[128] Caha, O.; Dubroka, A.; Humlíček, J.; Holý, V.; Steiner, H.; Ul-Hassan, M.; Sánchez-Barriga, J.; Rader, O.; Stanislavchuk, T. N.; Sirenko, a. a.; Bauer, G.; Springholz, G. Growth, Structure, and Electronic Properties of Epitaxial Bismuth Telluride Topological Insulator Films on BaF 2 (111) Substrates. *Crystal Growth & Design* **2013**, *13*, 3365–3373.

[129] Steiner, H.; Volobuev, V.; Caha, O.; Bauer, G.; Springholz, G.; Holý, V. Structure and composition of bismuth telluride topological insulators grown by molecular beam epitaxy. *Journal of Applied Crystallography* **2014**, *47*, 1889–1900.

[130] Harrison, S. E.; Li, S.; Huo, Y.; Zhou, B.; Chen, Y. L.; Harris, J. S. Two-step growth of high quality Bi 2 Te 3 thin films on Al 2 O 3 (0001) by molecular beam epitaxy. *Applied Physics Letters* **2013**, *102*, 171906.

[131] Kampmeier, J.; Borisova, S.; Plucinski, L.; Luysberg, M.; Mussler, G.; Grützmacher, D. Suppressing Twin Domains in Molecular Beam Epitaxy Grown Bi 2 Te 3 Topological Insulator Thin Films. *Crystal Growth & Design* **2015**, *15*, 390–394.

[132] Dai, J.; West, D.; Wang, X.; Wang, Y.; Kwok, D.; Cheong, S. W.; Zhang, S. B.; Wu, W. Toward the Intrinsic Limit of the Topological Insulator Bi2Se3. *Physical Review Letters* **2016**, *117*, 31–33.

[133] Benia, H. M.; Lin, C.; Kern, K.; Ast, C. R. Reactive Chemical Doping of the Bi2Te3 Topological Insulator. *Physical Review Letters* **2011**, *107*, 177602.

[134] Zhou, B.; Liu, Z. K.; Analytis, J. G.; Igarashi, K.; Mo, S. K.; Lu, D. H.; Moore, R. G.; Fisher, I. R.; Sasagawa, T.; Shen, Z. X.; Hussain, Z.; Chen, Y. L. Controlling the carriers of topological insulators by bulk and surface doping. *Semiconductor Science and Technology* **2012**, *27*, 124002.

[135] Kim, S. H.; Jin, K. H.; Park, J.; Kim, J. S.; Jhi, S. H.; Kim, T. H.; Yeom, H. W. Edge and interfacial states in a two-dimensional topological insulator: Bi(111) bilayer on Bi2Te2Se. *Physical Review B - Condensed Matter and Materials Physics* **2014**, *89*, 1–6.

[136] Yeom, H. W.; Kim, S. H.; Shin, W. J.; Jin, K.-H.; Park, J.; Kim, T.-H.; Kim, J. S.; Ishikawa, H.; Sakamoto, K.; Jhi, S.-H. Transforming a surface state of a topological insulator by a Bi capping layer. *Physical Review B* **2014**, *90*, 235401.

[137] Chien, Y.-j. Transition Metal-Doped Sb2Te3 and Bi2Te3 Diluted Magnetic Semiconductors. Ph.D. thesis, University of Michigan, 2007.

[138] Haazen, P. P. J.; Laloë, J.-B.; Nummy, T. J.; Swagten, H. J. M.; Jarillo-Herrero, P.; Heiman, D.; Moodera, J. S. Ferromagnetism in thin-film Cr-doped topological insulator Bi 2 Se 3. *Applied Physics Letters* **2012**, *100*, 082404.

[139] Zhang, D.; Richardella, A.; Rench, D. W.; Xu, S. Y.; Kandala, A.; Flanagan, T. C.; Beidenkopf, H.; Yeats, A. L.; Buckley, B. B.; Klimov, P. V.; Awschalom, D. D.; Yazdani, A.; Schiffer, P.; Hasan, M. Z.; Samarth, N. Interplay between ferromagnetism, surface states, and quantum corrections in a magnetically doped topological insulator. *Physical Review B - Condensed Matter and Materials Physics* **2012**, *86*, 1–9.

[140] Bao, L.; Wang, W.; Meyer, N.; Liu, Y.; Zhang, C.; Wang, K.; Ai, P.; Xiu, F. Quantum Corrections Crossover and Ferromagnetism in Magnetic Topological Insulators. *Scientific Reports* **2013**, *3*, 2391.

[141] Lee, J. S.; Richardella, A.; Rench, D. W.; Fraleigh, R. D.; Flanagan, T. C.; Borchers, J. A.; Tao, J.; Samarth, N. Ferromagnetism and spin-dependent transport in <math> <mi>n</mi> </math> -type Mn-doped bismuth telluride thin films. *Physical Review B* **2014**, *89*, 174425.

[142] Richardella, A.; Kandala, A.; Lee, J. S.; Samarth, N. Characterizing the structure of topological insulator thin films. *APL Materials* **2015**, *3*, 083303.

[143] Rubloff, G. W. Far-ultraviolet reflectance spectra and the electronic structure of ionic crystals. *Physical Review B* **1972**, *5*, 662–684.

[144] Bansal, N.; Kim, Y. S.; Edrey, E.; Brahlek, M.; Horibe, Y.; Iida, K.; Tanimura, M.; Li, G. H.; Feng, T.; Lee, H. D.; Gustafsson, T.; Andrei, E.; Oh, S. Epitaxial growth of topological insulator Bi 2Se 3 film on Si(111) with atomically sharp interface. *Thin Solid Films* **2011**, *520*, 224–229.

[145] Liu, Y.; Weinert, M.; Li, L. Spiral growth without dislocations: molecular beam epitaxy of the topological insulator Bi2Se3 on epitaxial graphene/SiC(0001). *Physical review letters* **2012**, *108*, 115501.

[146] Levy, I.; Garcia, T. A.; Shafique, S.; Tamargo, M. C. Reduced twinning and surface roughness of Bi 2 Se 3 and Bi 2 Te 3 layers grown by molecular beam epitaxy on sapphire substrates. *Journal of Vacuum Science & Technology B, Nanotechnology and Microelectronics: Materials, Processing, Measurement, and Phenomena* **2018**, *36*, 02D107.

[147] Hoefer, K.; Becker, C.; Wirth, S.; Hao Tjeng, L. Protective capping of topological surface states of intrinsically insulating Bi2Te3. *AIP Adv.* **2015**, *5*, 97139.

[148] Fornari, C. I.; Rappl, P. H. O.; Morelho, S. L.; Abramof, E. Structural properties of Bi2Te3 topological insulator thin films grown by molecular beam epitaxy on (111) BaF2 substrates. *Journal of Applied Physics* **2016**, *119*.

[149] Moulder, J.; Chastain, J. *Handbook of X-ray Photoelectron Spectroscopy: A Reference Book of Standard Spectra for Identification and Interpretation of XPS Data*; Physical Electronics Division, Perkin-Elmer Corporation, 1992.

[150] Wang, G.; Zhu, X. G.; Sun, Y. Y.; Li, Y. Y.; Zhang, T.; Wen, J.; Chen, X.; He, K.; Wang, L. L.; Ma, X. C.; Jia, J. F.; Zhang, S. B.; Xue, Q. K. Topological insulator thin films of Bi2Te3 with controlled electronic structure. *Advanced Materials* **2011**, *23*, 2929–2932.

[151] Borisova, S.; Kampmeier, J.; Luysberg, M.; Mussler, G.; Grützmacher, D. Domain formation due to surface steps in topological insulator Bi 2 Te 3 thin films grown on Si (111) by molecular beam epitaxy. *Applied Physics Letters* **2013**, *103*, 081902.

[152] Samoylov, A. M.; Klimov, A. E.; Akimov, A. N.; Paschin, N. S.; Shumsky, V. N.; Suprun, S. P.; Fedosenko, E. V.; Erkov, V. G.; Scheglow, D. V. Surface morphology and structure of CaF2/BaF2–on-Si epitaxial layers and the electronic properties of the interface with the substrate. 17th International Conference on Crystal Growth and Epitaxy - ICCGE-17, General Session 10. Warsav, 2013.

[153] Schouteden, K.; Govaerts, K.; Debehets, J.; Thupakula, U.; Chen, T.; Li, Z.; Netsou, A.; Song, F.; Lamoen, D.; Van Haesendonck, C.; Partoens, B.; Park, K. Annealing-Induced Bi Bilayer on Bi 2 Te 3 Investigated via Quasi-Particle-Interference Mapping. *ACS Nano* **2016**, *10*, 8778–8787.

[154] Liu, Y.; Li, Y. Y.; Rajput, S.; Gilks, D.; Lari, L.; Galindo, P. L.; Weinert, M.; Lazarov, V. K.; Li, L. Tuning Dirac states by strain in the topological insulator Bi_2Se_3. *Nature Physics* **2014**, *10*, 294–299.

[155] Aramberri, H.; Cerdá, J. I.; Muñoz, M. C. Tunable Dirac Electron and Hole Self-Doping of Topological Insulators Induced by Stacking Defects. *Nano Letters* **2015**, *15*, 3840–3844.

[156] Tarakina, N. V.; Schreyeck, S.; Borzenko, T.; Schumacher, C.; Karczewski, G.; Brunner, K.; Gould, C.; Buhmann, H.; Molenkamp, L. W. Comparative Study of the Microstructure of Bi 2 Se 3 Thin Films Grown on Si(111) and InP(111) Substrates. *Crystal Growth & Design* **2012**, *12*, 1913–1918.

[157] Tarakina, N. V.; Schreyeck, S.; Luysberg, M.; Grauer, S.; Schumacher, C.; Karczewski, G.; Brunner, K.; Gould, C.; Buhmann, H.; Dunin-Borkowski, R. E.; Molenkamp, L. W. Suppressing Twin Formation in Bi2Se3Thin Films. *Advanced Materials Interfaces* **2014**, *1*, 1–8.

[158] Höfer, K.; Becker, C.; Rata, D.; Swanson, J.; Thalmeier, P.; Tjeng, L. H. Intrinsic conduction through topological surface states of insulating Bi$_2$Te$_3$ epitaxial thin films. *Proceedings of the National Academy of Sciences* **2014**, *111*, 14979–14984.

[159] Bonell, F.; Cuxart, M. G.; Song, K.; Robles, R.; Ordejón, P.; Roche, S.; Mugarza, A.; Valenzuela, S. O. Growth of Twin-Free and Low-Doped Topological Insulators on BaF 2 (111). *Crystal Growth & Design* **2017**, *17*, 4655–4660.

[160] Li, C. H.; van 't Erve, O. M. J.; Yan, C.; Li, L.; Jonker, B. T. Electrical Detection of Charge-to-spin and Spin-to-Charge Conversion in a Topological Insulator Bi2Te3 Using BN/Al2O3 Hybrid Tunnel Barrier. *Scientific Reports* **2018**, *8*, 10265.

[161] Li, H. D.; Wang, Z. Y.; Kan, X.; Guo, X.; He, H. T.; Wang, Z.; Wang, J. N.; Wong, T. L.; Wang, N.; Xie, M. H. The van der Waals epitaxy of Bi 2 Se 3 on the vicinal Si(111) surface: an approach for preparing high-quality thin films of a topological insulator. *New Journal of Physics* **2010**, *12*, 103038.

[162] Kong, D.; Chen, Y.; Cha, J. J.; Zhang, Q.; Analytis, J. G.; Lai, K.; Liu, Z.; Hong, S. S.; Koski, K. J.; Mo, S. K.; Hussain, Z.; Fisher, I. R.; Shen, Z. X.; Cui, Y. Ambipolar field effect in the ternary topological insulator (BixSb1-x)2Te3by composition tuning. *Nature Nanotechnology* **2011**, *6*, 705–709.

[163] Carbone, C. et al. Self-Assembled Nanometer-Scale Magnetic Networks on Surfaces: Fundamental Interactions and Functional Properties. *Advanced Functional Materials* **2011**, *21*, 1212–1228.

[164] Gottfried, J. M. Surface chemistry of porphyrins and phthalocyanines. *Surface Science Reports* **2015**, *70*, 259–379.

[165] Gambardella, P. et al. Supramolecular control of the magnetic anisotropy in two-dimensional high-spin Fe arrays at a metal interface. *Nature Materials* **2009**, *8*, 189–193.

[166] Zhao, A.; Li, Q.; Chen, L.; Xiang, H.; Wang, W.; Pan, S.; Wang, B.; Xiao, X.; Yang, J.; Hou, J. G.; Zhu, Q. Controlling the Kondo Effect of an Adsorbed Magnetic Ion Through Its Chemical Bonding. *Science* **2005**, *309*, 1542–1544.

[167] Stepanow, S.; Miedema, P. S.; Mugarza, A.; Ceballos, G.; Moras, P.; Cezar, J. C.; Carbone, C.; de Groot, F. M. F.; Gambardella, P. Mixed-valence behavior and strong correlation effects of metal phthalocyanines adsorbed on metals. *Physical Review B* **2011**, *83*, 220401.

[168] Greuling, A.; Rohlfing, M.; Temirov, R.; Tautz, F. S.; Anders, F. B. Ab initio study of a mechanically gated molecule: From weak to strong correlation. *Physical Review B* **2011**, *84*, 125413.

[169] Gargiani, P.; Rossi, G.; Biagi, R.; Corradini, V.; Pedio, M.; Fortuna, S.; Calzolari, A.; Fabris, S.; Cezar, J. C.; Brookes, N. B.; Betti, M. G. Spin and orbital configuration of metal phthalocyanine chains assembled on the Au(110) surface. *Physical Review B* **2013**, *87*, 165407.

[170] Ternes, M.; Heinrich, A. J.; Schneider, W.-D. Spectroscopic manifestations of the Kondo effect on single adatoms. *Journal of Physics: Condensed Matter* **2009**, *21*, 053001.

[171] Hewson, A. C. *The Kondo Problem to Heavy Fermions*; Cambridge University Press: Cambridge, UK, 1997.

[172] Frank, S.; Jacob, D. Orbital signatures of Fano-Kondo line shapes in STM adatom spectroscopy. *Physical Review B* **2015**, *92*, 235127.

[173] Iancu, V.; Deshpande, A.; Hla, S.-W. Manipulating Kondo Temperature via Single Molecule Switching. *Nano Letters* **2006**, *6*, 820–823.

[174] Stróżecka, A.; Soriano, M.; Pascual, J. I.; Palacios, J. J. Reversible Change of the Spin State in a Manganese Phthalocyanine by Coordination of CO Molecule. *Physical Review Letters* **2012**, *109*, 147202.

[175] Liu, L.; Yang, K.; Jiang, Y.; Song, B.; Xiao, W.; Li, L.; Zhou, H.; Wang, Y.; Du, S.; Ouyang, M.; Hofer, W. A.; Castro Neto, A. H.; Gao, H.-J. Reversible Single Spin Control of Individual Magnetic Molecule by Hydrogen Atom Adsorption. *Scientific Reports* **2013**, *3*, 1210.

[176] Kim, H.; Chang, Y. H.; Lee, S.-h.; Kim, Y.-h.; Kahng, S.-j. Switching and Sensing Spin States of Co-Porphyrin in Bimolecular Reactions on Au (111) Using Scanning Tunneling Microscopy. *ACS Nano* **2013**, 9312–9317.

[177] Gao, L.; Ji, W.; Hu, Y. B.; Cheng, Z. H.; Deng, Z. T.; Liu, Q.; Jiang, N.; Lin, X.; Guo, W.; Du, S. X.; Hofer, W. A.; Xie, X. C.; Gao, H.-J. Site-Specific Kondo Effect at Ambient Temperatures in Iron-Based Molecules. *Physical Review Letters* **2007**, *99*, 106402.

[178] Minamitani, E.; Tsukahara, N.; Matsunaka, D.; Kim, Y.; Takagi, N.; Kawai, M. Symmetry-Driven Novel Kondo Effect in a Molecule. *Physical Review Letters* **2012**, *109*, 086602.

[179] Schneider, M.; Vitali, L.; Wahl, P.; Knorr, N.; Diekhöner, L.; Wittich, G.; Vogelgesang, M.; Kern, K. Kondo state of Co impurities at noble metal surfaces. *Applied Physics A* **2005**, *80*, 937–941.

[180] Temirov, R.; Lassise, A.; Anders, F. B.; Tautz, F. S. Kondo effect by controlled cleavage of a single-molecule contact. *Nanotechnology* **2008**, *19*, 065401.

[181] Stepanow, S.; Mugarza, A.; Ceballos, G.; Moras, P.; Cezar, J. C.; Carbone, C.; Gambardella, P. Giant spin and orbital moment anisotropies of a Cu-phthalocyanine monolayer. *Physical Review B* **2010**, *82*, 014405.

[182] Vijayaraghavan, S.; Auwärter, W.; Écija, D.; Seufert, K.; Rusponi, S.; Houwaart, T.; Sautet, P.; Bocquet, M. L.; Thakur, P.; Stepanow, S.; Schlickum, U.; Etzkorn, M.; Brune, H.; Barth, J. V. Restoring the co magnetic moments at interfacial co-porphyrin arrays by site-selective uptake of iron. *ACS Nano* **2015**, *9*, 3605–3616.

[183] Bhandary, S.; Brena, B.; Panchmatia, P. M.; Brumboiu, I.; Bernien, M.; Weis, C.; Krumme, B.; Etz, C.; Kuch, W.; Wende, H.; Eriksson, O.; Sanyal, B. Manipulation of spin state of iron porphyrin by chemisorption on magnetic substrates. *Physical Review B* **2013**, *88*, 024401.

[184] Hermanns, C. F.; Tarafder, K.; Bernien, M.; Krüger, A.; Chang, Y.-M.; Oppeneer, P. M.; Kuch, W. Magnetic Coupling of Porphyrin Molecules Through Graphene. *Advanced Materials* **2013**, *25*, 3473–3477.

[185] Bartolomé, J.; Bartolomé, F.; García, L. M.; Filoti, G.; Gredig, T.; Colesniuc, C. N.; Schuller, I. K.; Cezar, J. C. Highly unquenched orbital moment in textured Fe-phthalocyanine thin films. *Physical Review B* **2010**, *81*, 195405.

[186] Klar, D.; Bhandary, S.; Candini, A.; Joly, L.; Ohresser, P.; Klyatskaya, S.; Schleberger, M.; Ruben, M.; Affronte, M.; Eriksson, O.; Sanyal, B.; Wende, H. Field-regulated switching of the magnetization of Co-porphyrin on graphene. *Physical Review B* **2014**, *89*, 144411.

[187] Ballav, N.; Wäckerlin, C.; Siewert, D.; Oppeneer, P. M.; Jung, T. A. Emergence of On-Surface Magnetochemistry. *The Journal of Physical Chemistry Letters* **2013**, *4*, 2303–2311.

[188] Wäckerlin, C.; Nowakowski, J.; Liu, S.-X.; Jaggi, M.; Siewert, D.; Girovsky, J.; Shchyrba, A.; Hählen, T.; Kleibert, A.; Oppeneer, P. M.; Nolting, F.; Decurtins, S.; Jung, T. A.; Ballav, N. Two-Dimensional Supramolecular Electron Spin Arrays. *Advanced Materials* **2013**, *25*, 2404–2408.

[189] Miguel, J.; Hermanns, C. F.; Bernien, M.; Krüger, A.; Kuch, W. Reversible Manipulation of the Magnetic Coupling of Single Molecular Spins in Fe-Porphyrins to a Ferromagnetic Substrate. *The Journal of Physical Chemistry Letters* **2011**, *2*, 1455–1459.

[190] Wende, H. et al. Substrate-induced magnetic ordering and switching of iron porphyrin molecules. *Nature Materials* **2007**, *6*, 516–520.

[191] Lodi Rizzini, A.; Krull, C.; Balashov, T.; Mugarza, A.; Nistor, C.; Yakhou, F.; Sessi, V.; Klyatskaya, S.; Ruben, M.; Stepanow, S.; Gambardella, P. Exchange Biasing Single Molecule Magnets: Coupling of TbPc 2 to Antiferromagnetic Layers. *Nano Letters* **2012**, *12*, 5703–5707.

[192] Nistor, C.; Krull, C.; Mugarza, A.; Stepanow, S.; Stamm, C.; Soares, M.; Klyatskaya, S.; Ruben, M.; Gambardella, P. Exchange bias of <math> <msub> <mi>TbPc</mi> <mn>2</mn> </msub> </math> molecular magnets on antiferromagnetic FeMn and ferromagnetic Fe films. *Physical Review B* **2015**, *92*, 184402.

[193] Auwärter, W.; Écija, D.; Klappenberger, F.; Barth, J. V. Porphyrins at interfaces. *Nature Chemistry* **2015**, *7*, 105–120.

[194] Scheybal, A.; Ramsvik, T.; Bertschinger, R.; Putero, M.; Nolting, F.; Jung, T. Induced magnetic ordering in a molecular monolayer. *Chemical Physics Letters* **2005**, *411*, 214–220.

[195] Fanetti, M.; Calzolari, A.; Vilmercati, P.; Castellarin-Cudia, C.; Borghetti, P.; Di Santo, G.; Floreano, L.; Verdini, A.; Cossaro, A.; Vobornik, I.; Annese, E.; Bondino, F.; Fabris, S.; Goldoni, A. Structure and Molecule–Substrate Interaction in a Co-octaethyl Porphyrin Monolayer on the Ag(110) Surface. *The Journal of Physical Chemistry C* **2011**, *115*, 11560–11568.

[196] Unger, E.; Beck, M.; Lipski, R. J.; Dreybrodt, W.; Medforth, C. J.; Smith, K. M.; Schweitzer-Stenner, R. A New Method for Evaluating the Conformations and Normal Modes of Macromolecule Vibrations with a Reduced Force Field. 2. Application to Nonplanar Distorted Metal Porphyrins. *The Journal of Physical Chemistry B* **1999**, *103*, 10022–10031.

[197] Barlow, D. E.; Scudiero, L.; Hipps, K. W. Scanning Tunneling Microscopy Study of the Structure and Orbital-Mediated Tunneling Spectra of Cobalt(II) Phthalocyanine and Cobalt(II) Tetraphenylporphyrin on Au(111): Mixed Composition Films. *Langmuir* **2004**, *20*, 4413–4421.

[198] Kawamoto, T.; Yoshimoto, S. Tuning Porphyrin Assembly and Electrochemical Catalytic Activity with Halogen Substituents. *Langmuir* **2015**, *31*, 11532–11538.

[199] Brede, J. et al. Dynamics of molecular self-ordering in tetraphenyl porphyrin monolayers on metallic substrates. *Nanotechnology* **2009**, *20*, 275602.

[200] Kim, H.; Son, W. J.; Jang, W. J.; Yoon, J. K.; Han, S.; Kahng, S. J. Mapping the electronic structures of a metalloporphyrin molecule on Au(111) by scanning tunneling microscopy and spectroscopy. *Physical Review B - Condensed Matter and Materials Physics* **2009**, *80*, 1–6.

[201] Nagaoka, K.; Jamneala, T.; Grobis, M.; Crommie, M. F. Temperature Dependence of a Single Kondo Impurity. *Physical Review Letters* **2002**, *88*, 077205.

[202] Sarkar, S.; Yang, J.; Tan, L. Z.; Rappe, A. M.; Kronik, L. Molecule-Adsorbed Topological Insulator and Metal Surfaces: A Comparative First-Principles Study. *Chemistry of Materials* **2018**, *30*, 1849–1855.

[203] Pacchioni, G. E.; Pivetta, M.; Gragnaniello, L.; Donati, F.; Autès, G.; Yazyev, O. V.; Rusponi, S.; Brune, H. Two-Orbital Kondo Screening in a Self-Assembled Metal–Organic Complex. *ACS Nano* **2017**, *11*, 2675–2681.

[204] Joly, L.; Kappler, J.-P.; Ohresser, P.; Sainctavit, P.; Henry, Y.; Gautier, F.; Schmerber, G.; Kim, D. J.; Goyhenex, C.; Bulou, H.; Bengone, O.; Kavich, J.; Gambardella, P.; Scheurer, F. Kondo screening of the spin and orbital magnetic moments of Fe impurities in Cu. *Physical Review B* **2017**, *95*, 041108.

[205] Mellnik, A. R.; Lee, J. S.; Richardella, A.; Grab, J. L.; Mintun, P. J.; Fischer, M. H.; Vaezi, A.; Manchon, A.; Kim, E.-A.; Samarth, N.; Ralph, D. C. Spin-transfer torque generated by a topological insulator. *Nature* **2014**, *511*, 449–451.

[206] Wang, Y.; Deorani, P.; Banerjee, K.; Koirala, N.; Brahlek, M.; Oh, S.; Yang, H. Topological Surface States Originated Spin-Orbit Torques in Bi_2Se_3. *Physical Review Letters* **2015**, *114*, 257202.

[207] He, K.; Wang, Y.; Xue, Q. *Topological Insulators*; Wiley-VCH Verlag GmbH & Co. KGaA: Weinheim, Germany, 2015; Chapter 14, pp 357–376.

[208] Liu, C.-X.; Zhang, S.-C.; Qi, X.-L. The Quantum Anomalous Hall Effect: Theory and Experiment. *Annual Review of Condensed Matter Physics* **2016**, *7*, 301–321.

[209] Sánchez, J. C.; Vila, L.; Desfonds, G.; Gambarelli, S.; Attané, J. P.; De Teresa, J. M.; Magén, C.; Fert, A. Spin-to-charge conversion using Rashba coupling at the interface between non-magnetic materials. *Nature Communications* **2013**, *4*, 1–7.

[210] Schlenk, T.; Bianchi, M.; Koleini, M.; Eich, A.; Pietzsch, O.; Wehling, T. O.; Frauenheim, T.; Balatsky, A.; Mi, J. L.; Iversen, B. B.; Wiebe, J.; Khajetoorians, A. A.; Hofmann, P.; Wiesendanger, R. Controllable magnetic doping of the surface state of a topological insulator. *Physical Review Letters* **2013**, *110*, 1–5.

[211] Wray, L. A.; Xu, S. Y.; Xia, Y.; Hsieh, D.; Fedorov, A. V.; Hor, Y. S.; Cava, R. J.; Bansil, A.; Lin, H.; Hasan, M. Z. A topological insulator surface under strong Coulomb, magnetic and disorder perturbations. *Nature Physics* **2011**, *7*, 32–37.

[212] Abanin, D. a.; Pesin, D. a. Ordering of Magnetic Impurities and Tunable Electronic Properties of Topological Insulators. *Physical Review Letters* **2011**, *106*, 136802.

[213] Rüßmann, P. et al. Towards microscopic control of the magnetic exchange coupling at the surface of a topological insulator. *Journal of Physics: Materials* **2018**, *1*, 015002.

[214] Brede, J.; Atodiresei, N.; Kuck, S.; Lazić, P.; Caciuc, V.; Morikawa, Y.; Hoffmann, G.; Blügel, S.; Wiesendanger, R. Spin- and energy-dependent tunneling through a single molecule with intramolecular spatial resolution. *Physical Review Letters* **2010**, *105*, 1–4.

[215] Jakobs, S. et al. Controlling the Spin Texture of Topological Insulators by Rational Design of Organic Molecules. *Nano Letters* **2015**, *15*, 6022–6029.

[216] Sk, R.; Mulani, I.; Deshpande, A. Emergent Properties of the Organic Molecule-Topological Insulator Hybrid Interface: Cu-Phthalocyanine on Bi 2 Se 3. *The Journal of Physical Chemistry C* **2018**, *122*, 22996–23001.

[217] Song, Y. R.; Zhang, Y. Y.; Yang, F.; Zhang, K. F.; Liu, C.; Qian, D.; Gao, C. L.; Zhang, S. B.; Jia, J.-F. Magnetic anisotropy of van der Waals absorbed iron(II) phthalocyanine layer on Bi2Te3. *Physical Review B* **2014**, *90*, 180408.

[218] Hewitt, A.; Boltersdorf, J.; Maggard, P.; Dougherty, D. Recovery of the bulk-like electronic structure of manganese phthalocyanine beyond the first monolayer on Bi 2 Te 3. *Surface Science* **2017**, *662*, 87–92.

[219] Sessi, P.; Bathon, T.; Kokh, K. A.; Tereshchenko, O. E.; Bode, M. Probing the Electronic Properties of Individual MnPc Molecules Coupled to Topological States. *Nano Letters* **2014**, *14*, 5092–5096.

[220] Nam, M.-S.; Williams, B. H.; Chen, Y.; Contera, S.; Yao, S.; Lu, M.; Chen, Y.-F.; Timco, G. A.; Muryn, C. A.; Winpenny, R. E. P.; Ardavan, A. How to probe the spin contribution to momentum relaxation in topological insulators. *Nature Communications* **2018**, *9*, 56.

[221] Seufert, K.; Bocquet, M.-L.; Auwärter, W.; Weber-Bargioni, A.; Reichert, J.; Lorente, N.; Barth, J. V. Cis-dicarbonyl binding at cobalt and iron porphyrins with saddle-shape conformation. *Nature Chemistry* **2011**, *3*, 114–119.

[222] Jarvis, S. P.; Taylor, S.; Baran, J. D.; Thompson, D.; Saywell, A.; Mangham, B.; Champness, N. R.; Larsson, J. A.; Moriarty, P. Physisorption Controls the Conformation and Density of States of an Adsorbed Porphyrin. *The Journal of Physical Chemistry C* **2015**, *119*, 27982–27994.

[223] Houwaart, T.; Le Bahers, T.; Sautet, P.; Auwärter, W.; Seufert, K.; Barth, J. V.; Bocquet, M. L. Scrutinizing individual CoTPP molecule adsorbed on coinage metal surfaces from the interplay of STM experiment and theory. *Surface Science* **2015**, *635*, 108–114.

[224] Mugarza, A.; Lorente, N.; Ordejón, P.; Krull, C.; Stepanow, S.; Bocquet, M. L.; Fraxedas, J.; Ceballos, G.; Gambardella, P. Orbital specific chirality and homochiral self-assembly of achiral molecules induced by charge transfer and spontaneous symmetry breaking. *Physical Review Letters* **2010**, *105*, 30–33.

[225] Rabe, J. P.; Buchholz, S. Commensurability and Mobility in Two-Dimensional Molecular Patterns on Graphite. *Science* **1991**, *253*, 424–427.

[226] Yokoyama, T.; Yokoyama, S.; Kamikado, T.; Okuno, Y.; Mashiko, S. Selective assembly on a surface of supramolecular aggregates with controlled size and shape. *Nature* **2001**, *413*, 619–621.

[227] Schlickum, U.; Decker, R.; Klappenberger, F.; Zoppellaro, G.; Klyatskaya, S.; Ruben, M.; Silanes, I.; Arnau, A.; Kern, K.; Brune, H.; Barth, J. V. Metal-organic honeycomb nanomeshes with tunable cavity size. *Nano letters* **2007**, *7*, 3813–7.

[228] Theobald, J. A.; Oxtoby, N. S.; Phillips, M. A.; Champness, N. R.; Beton, P. H. Controlling molecular deposition and layer structure with supramolecular surface assemblies. *Nature* **2003**, *424*, 1029–1031.

[229] Franc, G.; Gourdon, A. Covalent networks through on-surface chemistry in ultra-high vacuum: State-of-the-art and recent developments. *Physical Chemistry Chemical Physics* **2011**, *13*, 14283–14292.

[230] Nitzan, A. Electron Transport in Molecular Wire Junctions. *Science* **2003**, *300*, 1384–1389.

[231] Lafferentz, L.; Ample, F.; Yu, H.; Hecht, S.; Joachim, C.; Grill, L. Conductance of a Single Conjugated Polymer as a Continuous Function of Its Length. *Science* **2009**, *323*, 1193–1197.

[232] Koch, M.; Ample, F.; Joachim, C.; Grill, L. Voltage-dependent conductance of a single graphene nanoribbon. *Nature Nanotechnology* **2012**, *7*, 713–717.

[233] Kittelmann, M.; Rahe, P.; Nimmrich, M.; Hauke, C. M.; Gourdon, A.; Kühnle, A. On-Surface Covalent Linking of Organic Building Blocks on a Bulk Insulator. *ACS Nano* **2011**, *5*, 8420–8425.

[234] Abel, M.; Clair, S.; Ourdjini, O.; Mossoyan, M.; Porte, L. Single Layer of Polymeric Fe-Phthalocyanine: An Organometallic Sheet on Metal and Thin Insulating Film. *Journal of the American Chemical Society* **2011**, *133*, 1203–1205.

[235] Kittelmann, M.; Nimmrich, M.; Lindner, R.; Gourdon, A.; Kühnle, A. Sequential and Site-Specific On-Surface Synthesis on a Bulk Insulator. *ACS Nano* **2013**, *7*, 5614–5620.

[236] Chen, H.; Zhu, W.; Xiao, D.; Zhang, Z. CO Oxidation Facilitated by Robust Surface States on Au-Covered Topological Insulators. *Physical Review Letters* **2011**, *107*, 056804.

[237] West, D.; Sun, Y. Y.; Zhang, S. B.; Zhang, T.; Ma, X.; Cheng, P.; Zhang, Y. Y.; Chen, X.; Jia, J. F.; Xue, Q. K. Identification of magnetic dopants on the surfaces of topological insulators: Experiment and theory for Fe on Bi 2Te 3(111). *Physical Review B - Condensed Matter and Materials Physics* **2012**, *85*, 2–6.

[238] Wang, Y.-L.; Xu, Y.; Jiang, Y.-P.; Liu, J.-W.; Chang, C.-Z.; Chen, M.; Li, Z.; Song, C.-L.; Wang, L.-L.; He, K.; Chen, X.; Duan, W.-H.; Xue, Q.-K.; Ma, X.-C. Structural defects and electronic properties of the Cu-doped topological insulator Bi2Se3. *Physical Review B* **2011**, *84*, 075335.

[239] Schmidt, T. M.; Miwa, R. H.; Fazzio, A. Spin texture and magnetic anisotropy of Co impurities in Bi2Se3 topological insulators. *Physical Review B* **2011**, *84*, 245418.

[240] Li, Y.; Xiao, J.; Shubina, T. E.; Chen, M.; Shi, Z.; Schmid, M.; Steinrück, H. P.; Gottfried, J. M.; Lin, N. Coordination and metalation bifunctionality of Cu with 5,10,15,20-tetra(4- pyridyl)porphyrin: Toward a mixed-valence two-dimensional coordination network. *Journal of the American Chemical Society* **2012**, *134*, 6401–6408.

[241] Pia, A. D.; Lisi, S.; Luca, O. D.; Warr, D. A.; Lawrence, J.; Otrokov, M. M.; Aliev, Z. S.; Chulkov, E. V.; Agostino, R. G.; Arnau, A.; Papagno, M.; Costantini, G. TCNQ Physisorption on the Topological Insulator Bi2Se3. *ChemPhysChem* **2018**, *19*, 2405–2410.

[242] Cuxart, M. G.; Valbuena, M. A.; Robles, R.; Moreno, C.; Bonell, F.; Imaz, I.; Nistor, C.; Barla, A.; Gargiani, P.; Valvidares, M.; Daniel, M.; Gambardella, P.; Ordejón, P.; Valenzuela, S. O.; Mugarza, A. Metal-organic topological insulator heterostructures with robust interfacial properties. *to be submitted*

[243] Gutzler, R.; Walch, H.; Eder, G.; Kloft, S.; Heckl, W. M.; Lackinger, M. Surface mediated synthesis of 2D covalent organic frameworks: 1,3,5-tris(4-bromophenyl)benzene on graphite(001), Cu(111), and Ag(110). *Chemical Communications* **2009**, 4456.

[244] Fan, Q.; Wang, C.; Han, Y.; Zhu, J.; Hieringer, W.; Kuttner, J.; Hilt, G.; Gottfried, J. M. Surface-Assisted Organic Synthesis of Hyperbenzene Nanotroughs. *Angewandte Chemie International Edition* **2013**, *52*, 4668–4672.

[245] Écija, D.; Urgel, J. I.; Papageorgiou, A. C.; Joshi, S.; Auwarter, W.; Seitsonen, A. P.; Klyatskaya, S.; Ruben, M.; Fischer, S.; Vijayaraghavan, S.; Reichert, J.; Barth, J. V. Five-vertex Archimedean surface tessellation by lanthanide-directed molecular self-assembly. *Proceedings of the National Academy of Sciences* **2013**, *110*, 6678–6681.

[246] Lin, T.; Kuang, G.; Wang, W.; Lin, N. Two-Dimensional Lattice of Out-of-Plane Dinuclear Iron Centers Exhibiting Kondo Resonance. *ACS Nano* **2014**, *8*, 8310–8316.

[247] Urgel, J. I.; Écija, D.; Auwärter, W.; Stassen, D.; Bonifazi, D.; Barth, J. V. Orthogonal insertion of lanthanide and transition-metal atoms in metal-organic networks on surfaces. *Angewandte Chemie - International Edition* **2015**, *54*, 6163–6167.

[248] Urgel, J. I.; Écija, D.; Lyu, G.; Zhang, R.; Palma, C.-A.; Auwarter, W.; Lin, N.; Barth, J. V. Quasicrystallinity expressed in two-dimensional coordination networks. *Nature Chemistry* **2016**, *8*, 657–662.

[249] Bischoff, F.; He, Y.; Seufert, K.; Stassen, D.; Bonifazi, D.; Barth, J. V.; Auwärter, W. Tailoring Large Pores of Porphyrin Networks on Ag(111) by Metal–Organic Coordination. *Chemistry - A European Journal* **2016**, *22*, 15298–15306.

[250] Shi, Z.; Lin, N. Porphyrin-Based Two-Dimensional Coordination Kagome Lattice Self-Assembled on a Au(111) Surface. *Journal of the American Chemical Society* **2009**, *131*, 5376–5377.

[251] Shi, Z.; Lin, N. Self-assembly of a two-dimensional bimetallic coordination framework and dynamic control of reversible conversions to homo-metallic hydrogen-bond arrays. *ChemPhysChem* **2010**, *11*, 97–100.

[252] Li, Y.; Lin, N. Combined scanning tunneling microscopy and kinetic Monte Carlo study on kinetics of Cu-coordinated pyridyl-porphyrin supramolecular self-assembly on a Au(111) surface. *Physical Review B* **2011**, *84*, 125418.

[253] Lyu, G.; Zhang, R.; Zhang, X.; Nian Liu, P.; Lin, N. On-surface assembly of low-dimensional Pb-coordinated metal-organic structures. *Journal of Materials Chemistry C* **2015**, *3*, 3252–3257.

[254] Beggan, J. P.; Boyle, N. M.; Pryce, M. T.; Cafolla, A. A. Surface-confined Ullmann coupling of thiophene substituted porphyrins. *Nanotechnology* **2015**, *26*, 365602.

[255] Wurster, B.; Grumelli, D.; Hötger, D.; Gutzler, R.; Kern, K. Driving the Oxygen Evolution Reaction by Nonlinear Cooperativity in Bimetallic Coordination Catalysts. *Journal of the American Chemical Society* **2016**, *138*, 3623–3626.

[256] Wang, Y.; Zhou, K.; Shi, Z.; Ma, Y. Q. Structural reconstruction and spontaneous formation of Fe polynuclears: A self-assembly of Fe-porphyrin coordination chains on Au(111) revealed by scanning tunneling microscopy. *Physical Chemistry Chemical Physics* **2016**, *18*, 14273–14278.

[257] Chen, X.; Lei, S.; Lotze, C.; Czekelius, C.; Paulus, B.; Franke, K. J. Conformational adaptation and manipulation of manganese tetra(4-pyridyl)porphyrin molecules on Cu(111). *The Journal of Chemical Physics* **2017**, *146*, 092316.

[258] Haq, S.; Hanke, F.; Dyer, M. S.; Persson, M.; Iavicoli, P.; Amabilino, D. B.; Raval, R. Clean Coupling of Unfunctionalised Porphyrins at Surfaces to Give Highly Oriented Organometallic Oligomers Clean Coupling of Unfunctionalised Porphyrins at Surfaces to Give Highly Oriented Organometallic Oligomers. *Surface Science* **2011**, 12031–12039.

[259] Chen, C.; Joshi, T.; Li, H.; Chavez, A. D.; Pedramrazi, Z.; Liu, P.-N.; Li, H.; Dichtel, W. R.; Bredas, J.-L.; Crommie, M. F. Local Electronic Structure of a Single-Layer Porphyrin-Containing Covalent Organic Framework. *ACS Nano* **2018**, *12*, 385–391.

[260] Stepanow, S.; Lin, N.; Barth, J. V. Modular assembly of low-dimensional coordination architectures on metal surfaces. *Journal of Physics: Condensed Matter* **2008**, *20*, 184002.

[261] Björk, J. Reaction mechanisms for on-surface synthesis of covalent nanostructures. *Journal of Physics: Condensed Matter* **2016**, *28*, 083002.

[262] Lackinger, M. Surface-assisted Ullmann coupling. *Chemical Communications* **2017**, *53*, 7872–7885.

[263] Moreno, C.; Panighel, M.; Vilas-Varela, M.; Sauthier, G.; Tenorio, M.; Ceballos, G.; Peña, D.; Mugarza, A. Critical Role of Phenyl Substitution and Catalytic Substrate in the Surface-Assisted Polymerization of Dibromobianthracene Derivatives. *Chemistry of Materials* **2019**, *31*, 331–341.

[264] Sessi, P. et al. Superparamagnetism-induced mesoscopic electron focusing in topological insulators. *Physical Review B* **2016**, *94*, 075137.

[265] Yang, H. H.; Chu, Y. H.; Lu, C. I.; Butler, C. J.; Sankar, R.; Chou, F. C.; Lin, M. T. Organic Monolayer Protected Topological Surface State. *Nano Letters* **2015**, *15*, 6896–6900.

[266] Tan, J.; Li, W.; He, X.; Zhao, M. Stable ferromagnetism and half-metallicity in two-dimensional polyporphyrin frameworks. *RSC Advances* **2013**, *3*, 7016.

[267] Cook, T. R.; Zheng, Y.-R.; Stang, P. J. Metal–Organic Frameworks and Self-Assembled Supramolecular Coordination Complexes: Comparing and Contrasting the Design, Synthesis, and Functionality of Metal–Organic Materials. *Chemical Reviews* **2013**, *113*, 734–777.

[268] Guo, F.-S.; Day, B. M.; Chen, Y.-C.; Tong, M.-L.; Mansikkamäki, A.; Layfield, R. A. Magnetic hysteresis up to 80 kelvin in a dysprosium metallocene single-molecule magnet. *Science* **2018**, *362*, 1400–1403.

[269] Checkelsky, J. G.; Ye, J.; Onose, Y.; Iwasa, Y.; Tokura, Y. Dirac-fermion-mediated ferromagnetism in a topological insulator. *Nature Physics* **2012**, *8*, 729–733.

[270] Chang, C.-Z. et al. Thin Films of Magnetically Doped Topological Insulator with Carrier-Independent Long-Range Ferromagnetic Order. *Advanced Materials* **2013**, *25*, 1065–1070.

[271] Liu, Q.; Liu, C.-X.; Xu, C.; Qi, X.-L.; Zhang, S.-C. Magnetic Impurities on the Surface of a Topological Insulator. *Physical Review Letters* **2009**, *102*, 156603.

[272] NIST: Database of electron inelastic mean free path for elemental solids.

Publications

Cuxart, M. G.; Valbuena, M. A.; Moreno, C.; Bonell, F.; Robles, R.; Cruz, J.; Imaz, I.; Maspoch, D.; Ordejón, P.; Valenzuela, S.; Mugarza, A. **Metal-organic Coordination Structure Synthesized on a Topological Insulator Surface**. *To be submitted.*

Cuxart, M. G.; Valbuena, M. A.; Moreno, C.; Bonell, F.; Robles, R.; Cruz, J.; Imaz, I.; Maspoch, D.; Nistor, C.; Gargiani, P.; Ordejón, P.; Gambardella, P.; Valenzuela, S.; Mugarza, A. **Metal-Organic Topological Insulator Heterostructure With Robust Interfacial Properties**. *To be submitted.*

Cuxart, M. G.; Valbuena, M. A.; Robles, R.; Huille, J.; Moreno, C.; Bonell, F.; Maspoch, D.; Nistor, C.; Barla, A.; Perischetti, L.; Verdu, C.; Pascual, J. I.; Plantek, M.; Serrate, D.; Gargiani, P.; Gambardella, P.; Valenzuela, S.; Mugarza, A. **Engineering spin states and interactions by ligand chemistry of molecules on surfaces**. *To be submitted.*

Figueroa, A.; Bonell, F; Cuxart, M. G.; Valvidares, M.; van der Laan. G.; Mugarza, A.; Valenzuela, S. Investigating **Magnetic Proximity Effects at Topological Insulators/Magnetic Insulator Interfaces**. *To be submitted.*

Bonell, F.; Cuxart, M. G.; Song, K;, Robles, R.; Ordejón, P.; Roche, S.; Mugarza, A.; Valenzuela, S. O. **Growth of Twin-Free and Low-Doped Topological Insulators on BaF_2(111)**. *Cryst. Growth Des.* 2017, *17*(9), 4655-4660.

Appendix A

Analysis of the CoTBrPP Rotational Domains

In Section 5.1, it is reported that Cobalt - Tetrakis (4-Promophenyl) Porphyrin (CoTBrPP) molecules deposited on Bismuth Telluride (Bi_2Te_3) substrate self-assemble in condensed ordered islands. The periodicity of such islands is described by a quasi-square lattice, that leads to a commensurate stacking with the underlying hexagonal surface. Hence, the 2-fold symmetry of the molecular lattice in combination with the 6-fold symmetry of the surface leads to the formation of 3 equivalent rotational domains. In this appendix, we report a statistical study of the orientations of the molecular lattices that confirms the sole presence of such domains.

26 orientations of molecular islands were measured on different Scanning Tunneling Microscopy (STM) images. These are plotted by black solid lines in Figure A.1, superposed to the base vectors predicted by the quasi-square lattice (92.2° between lattice vectors) measured previously, and by a hypothetical square lattice (90°). This allows us to asses the discrepancies between the two lattices, between the 90° and 92.2° MODELs. Inset table shows that the measured $\angle b_1 b_2$ angles are compatible with the predicted 92.2° within the error margin, and that their agreement is higher with the 92.2° MODEL than with the 90° MODEL.

Therefore, this is finding further endorses the commensurate quasi-square lattice described in Section 5.1.1 Chapter 5.

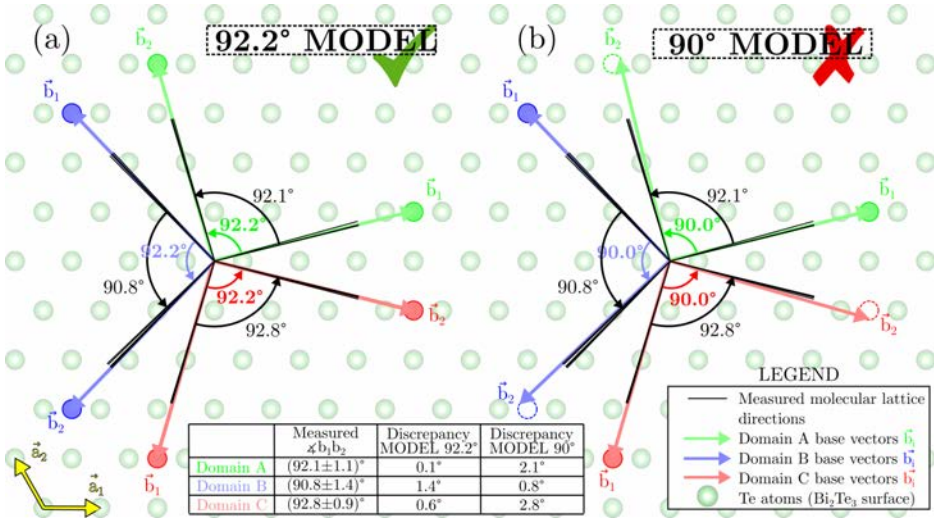

Figure A.1: Schematic of the measured directions in which CoTBrPP islands are oriented, represented together with the base vectors of the three equivalent rotated domains predicted by (a) the 92.2° Model (quasi-square lattice, $\angle b_1 b_2 = 92.2°$) and (b) the 90° Model (square lattice, $\angle b_1 b_2 = 90.0°$). Higher agreement with 92.2° Model is evidenced in the inset table showing the discrepancies of the experimental data with both models. Full dashed circles represent Te-Te bridge positions pointed by lattice vectors, meanwhile empty dashed circles represent Te-Te bridge positions not pointed by some lattice vectors, highlighting the commensurably of the 92.2° Model against the no-commensurably of the 90° Model.

Appendix B

Estimation of the Molecular Coverages in the Photoemission Experiments

The molecular coverage in photoemission experiments was calculated using the Beer-Lambert law, which describes the attenuation of radiation passing through a material. We make an approximation that has been successfully used in the literature for systems formed by molecules deposited on metallic substrates. We suppose an heterosystem formed by an homogeneous layer of thickness d lying on top of an infinitely thick and homogeneous substrate. Therefore, the intensity of photoemitted electrons from the substrate (I_0) is attenuated by the layer and, assuming that attenuators act independently, the transmitted intensity I_{trans} is described by

$$I_{trans} = I_0 e^{-d/\lambda}, \tag{B.1}$$

where λ is the inelastic mean free path of a photoemitted electrons in a solid for a given energy.

Bi $4f_{7/2}$ peak was used in our calculation as it is an intense feature emerging from the Bismuth Telluride (Bi_2Te_3) substrate. Bi has an invariable chemical environment upon deposition of molecules and annealings. I^{Bi} was measured by integrating the Bi $4f_{7/2}$ peak with a Shirley background subtracted and normalized with each own flat offset. Due to the energy of the exciting photon (1486 eV) used in this experimental setup (see Section 2.3), elastically photoemitted Bi $4f_{7/2}$ electrons have a kinetic energy of 1326 eV, which leads to $\lambda(1339eV) = 22.9$ Å[272]. Adsorption distance for Cobalt - Tetrakis (4-Promophenyl) Porphyrin (CoTBrPP) and Cobalt - Phthalocyanine (CoPc) calculated by Density Functional Theory (DFT), 3.82 Å and 3.00 Å respectively, was used as an effective thickness d corresponding to 1 ML.

Changes in the Bi $4f_{7/2}$ intensity between the pristine Bi_2Te_3 sample I_0^{Bi}

and after each i evaporation I_i^{Bi} were used to obtain the effective d^i, which was linearly related to the molecular coverage θ_i as

$$\theta_i = \frac{d_i}{d} = \frac{\lambda}{d}\, ln\left(\frac{I_i^{Bi}}{I_0^{Bi}}\right) \tag{B.2}$$

This method has been used to calculate the molecular coverages in the photoemission experiments performed in Chapter 6. Nevertheless, in the experiments shown in Chapter 5, we did not get reliable Bi data after every evaporation due to experimental issues. In order to obtain a coverage value for each point, we set the evaporation time corresponding to 1 ML, by making a linear fit to the points with available Bi data (Figure B.1a). Then, knowing the linear dependence of the amount of molecules with the evaporation time (Figure B.1b), we rescaled the coverage of each point to the defined 1 ML (Figure B.1c).

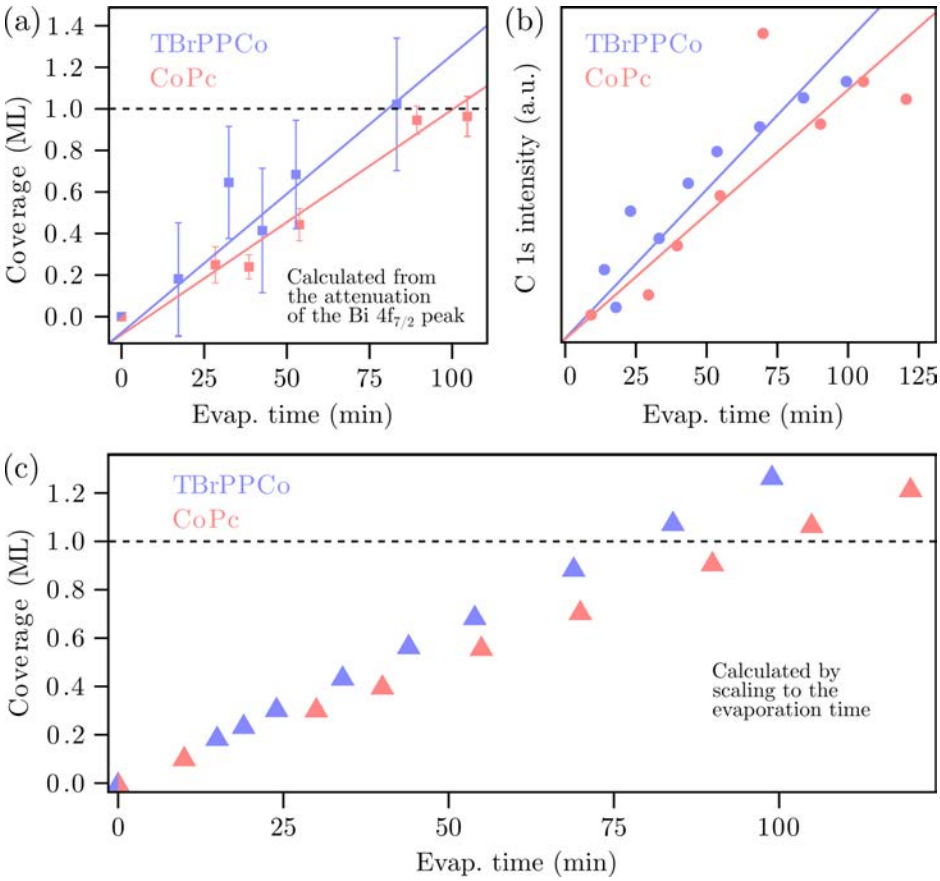

Figure B.1: (a) Dependence of the XPS intensity of the C 1s peak with respect to the total evaporation time, for the CoTBrPP on Bi_2Te_3, and CoPc on Bi_2Te_3 systems. Linear regressions show linearity between amount of carbon deposited and evaporation time. (b) Molecular coverage extracted from the attenuation of the Bi $4f_{7/2}$ peak, by using the Beer-Lambeert law, and linear regressions for both systems.(c) Coverage calculated from the linear regressions in for both systems.

Appendix C

Complementary STM Images of the Polymeric Phase

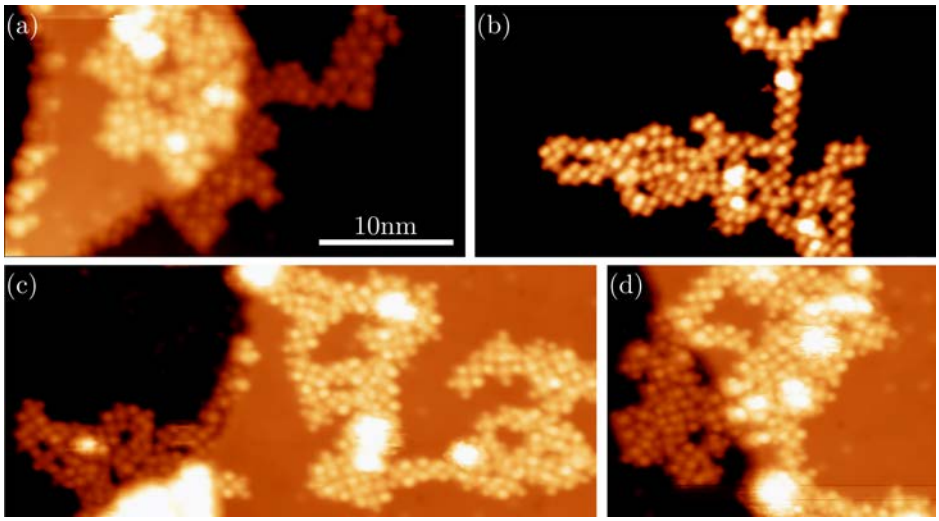

Figure C.1: STM topographic images of various coordination polymers showing non-homogeneous shapes, at (a) 1.4 V and 0.019 nA, (b) 1.4 V and 0.027 nA, (c) 1.3 V, 1.3 V and 0.015 nA and (d) 1.4 V and 0.022 nA. All images have the same magnification described by the scale bar in (a).

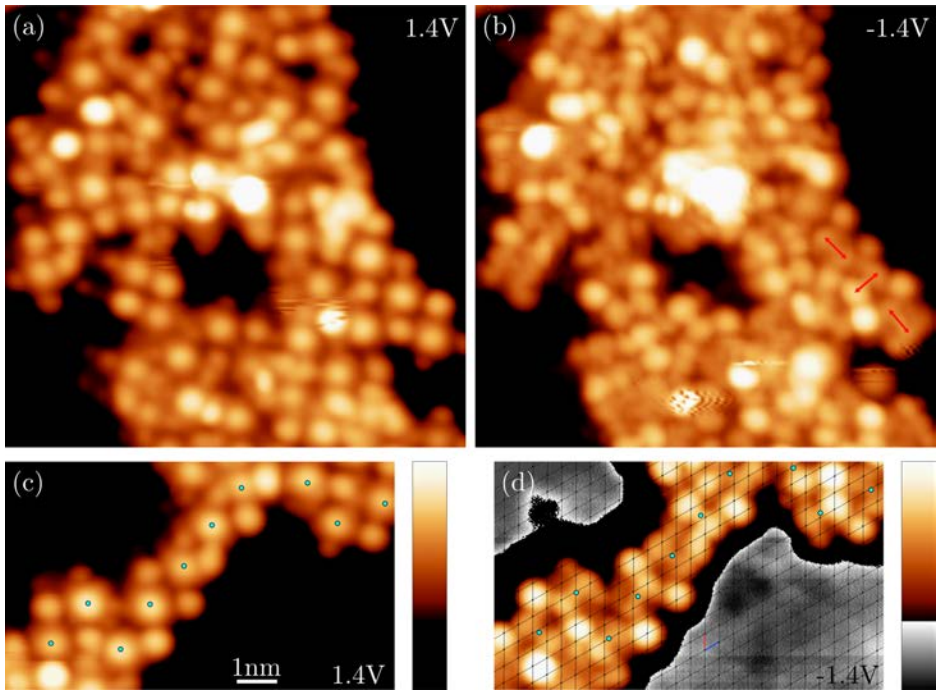

Figure C.2: Pairs of STM topographic images of different regions of the same polymer measured at ((a) and (c)) positive (1.4 V) and ((b) and (d)) negative (−1.4 V) bias voltage. (a) and (b) 0.019 nA, (c) and (d) 0.037 nA. They exhibit d_{z2} (blue solid circles) and d_{xz} orbitals (red arrows), respectively. Both features are indispensable for the identification of the position and orientation of each monomer. Atomic resolution in (d) unveils non-commensurability between polymer and substrate. All images have the same magnification described by the scale bar in (a).

Acknowledgements

First and foremost, I would like to express my gratitude to my three thesis directors. To Aitor Mugarza, for being an endless source of motivation, enthusiasm, commitment and scientific inspiration. To Sergio Valenzuela, for his steadfast and sharp advises, and for giving me the opportunity to widen the scope of my research and knowledge. To César Moreno, for his inexhaustible sense of working, and specially for persisting in guiding me through the ins and outs of a thesis.

I want to thank two scientists that have been essential to me. Frédéric Bonell, probably the person whom I learned more science during this period. It has been a pleasure to enjoy all those fruitful scientific discussions full of complicity. And Markos Paradinas, for giving me unlimited support during the ups and downs of this thesis. Not only me but also the AMS group should feel very lucky to have him close, as I am convinced that he is the human cement of this group.

Thanks to Miguel Valbuena as well, for the side-by-side work in all those innumerable beamtime experiments, and for becoming my mirror image when it comes to football. To Michele Gastaldo, for being the omnipresent and always-aware-of-everything office mate, and a great Italian teacher! To María Tenorio, for his contagious enthusiasm and dedication. And to the rest of members of the AMS group that I had the pleasure to work with: Stefano Schirone, Mercedes Saludes, Amina Kimouche, Nicolau Molina, Jeremy Hieulle, Mirko Panighel, Sofia Parreiras and summer interns. Many thanks to Adriana, for his gentleness way of conducting research and colleague relations, and of course to the rest of the PEND team: Antonio Benítez, Juan Sierra, Marius Costache, Iván Fernández, Williams Savero, Aloïs Arrighi, Regina Galceran, Matias Timmermans, Zewdu Messele and former members.

This thesis would not have been possible without the expertise of some ICN2 scientists and technicians. Thanks to Gustavo Ceballos, Marc Maymó and Rafael León for the efforts in the design and fabrication of the "double-sample holder", it represented a breakthrough! To Guillaume Sauthier, for his will to support us in the photoemission experiments. Thanks to Roberto Robles, for his non-stop stream of calculations and for those gratifying scientific discussions. To Inhar Imaz and his team, for synthesizing and providing most of the molecules used in our studies. And to the BOREAS beamline staff in ALBA synchrotron, Pierluigi Gargiani and Manuel Valvidares, always willing to a last-minute experiment.

Gracias a ti, por creer tanto en mí. Y porque tu también sabes rescaterme cuando es necesario, sobretodo de mis "caras de pantalla"! Gràcies als meus

pares, Josep Maria i Maria Dolors, i a l'Esteve, per haver-me dut fins aquí. La seva perseverança i suport incondicional ho han fet possible. També als avis i abuelitos, per haver-me acompanyat sempre.

Gràcies al grup dels fRísics, companys de tants combats impossibles al final de cada semestre, i per damunt de tot amics. I a la Sandra. Òbviament també a tots els sapastres del grup d'Enveitg, per procurar-me un racó de desequilibri i amistat. I també a l'Alibe i l'Albert, per haver suportat el dia a dia dels mesos d'escriptura en primera línia.

Last but not least, I must recall many of the teachers and supervisors that I had ever since physics engaged me. Some of them became mentors to me: special thanks to Eric Pellegrín, and to Tomàs Salamí, el veritable responsable d'haver-me despertat la vocació científica.